R-13-29

Äspö Hard Rock Laboratory

Äspö Pillar Stability Experiment

Coupled Stress-flow tests on large fracture samples from the APSE site

Diego Mas Ivars, Katarina Norén
Itasca Geomekanik AB

May 2017

Svensk Kärnbränslehantering AB
Swedish Nuclear Fuel
and Waste Management Co

Box 3091, SE-169 03 Solna
Phone +46 8 459 84 00

ISSN 1402-3091
SKB R-13-29
ID 1581058
May 2017

Äspö Hard Rock Laboratory

Äspö Pillar Stability Experiment

Coupled Stress-flow tests on large fracture samples from the APSE site

Diego Mas Ivars, Katarina Norén
Itasca Geomekanik AB

This report concerns a study which was conducted for Svensk Kärnbränslehantering AB (SKB). The conclusions and viewpoints presented in the report are those of the authors. SKB may draw modified conclusions, based on additional literature sources and/or expert opinions.

A pdf version of this document can be downloaded from www.skb.se.

© 2017 Svensk Kärnbränslehantering AB

Abstract

Fully coupled stress-flow tests have been performed on three large fracture samples, Sample 1, Sample 2 and Sample 3, with fracture areas 13 cm × 13 cm, 15 cm × 15 cm and 15 cm × 15 cm respectively, taken from the APSE site at the Äspö HRL in Sweden. Usually, tests of this type are performed with synthetic fracture samples or with artificially induced fracture samples due to the difficulty in obtaining undisturbed real fracture samples. Artificial or induced fractures are usually fresh and very well mated and do not have the same geological history as natural ones do.

The fracture samples used in this set of tests were drilled from a very conductive fracture belonging to the NW-SE, sub-vertical fracture set that is responsible for most of the water flow at the Äspö HRL. This fracture intersected one of the deposition holes of the APSE experiment. Flow and displacements (normal and shear) from this fracture were monitored during the de-stressing of the APSE pillar and it showed a highly stress dependent flow behaviour. For this reason it was decided to take advantage of this unique opportunity and try to characterize the coupled stress-flow behaviour of this fracture in the laboratory.

The derived values of fracture normal stiffness, fracture shear stiffness and fracture peak shear strength do not differ significantly. However, meaningful shear dilation begins at approximately 2.25 mm of shear displacement for Sample 1, while it occurs at about 0.5 mm and 1.1 mm of shear displacement for Sample 2 and Sample 3 respectively.

The “cubic law” with an adjusting friction factor, seems to be an adequate predictor for the coupled stress-flow behaviour of Sample 1 up to a shear displacement of 2–3 mm. The flow in Samples 2 and 3 seems to have a turbulent component that cannot be neglected and therefore the “cubic law” is not sufficient for its prediction. Other factors not studied in this project may also influence the coupled behaviour (i.e. gouge generation).

Even if the three fracture samples tested in this project are relatively large, and they belonged to the same large fracture in the APSE tunnel and were separated less than 1 meter from each other in-situ, their coupled stress-flow behaviour is remarkably different. This confirms the idea that, for this type of highly water bearing fracture, a hydraulically representative fracture area is probably larger than the areas of the fracture samples tested in this project.

Sammanfattning

Kombinerade spänning/flödestest har utförts på tre större sprickprov tagna från området för pelarstabilitetsförsöket (APSE) vid Äspölaboratioriet, Prov 1, Prov 2 och Prov 3, med respektive sprickytor 13 × 13 cm, 15 × 15 cm och 15 × 15 cm. Vanligtvis görs skjuvförsök av det här slaget med syntetiska sprickprover eller med inducerade sprickprover på grund av svårigheten i att få fram opåverkade naturliga sprickprover. Dock har syntetiska eller inducerade sprickor ofta mycket välmatchande sprickytor och de har inte samma geologiska bakgrund som naturliga sprickor har.

Sprickproverna som användes i provtagningarna borrades från en mycket vattenförande spricka tillhörande det NW-SE, subvertikala sprickset som står för det mesta av vattenflödet vid Äspölaboratoriet. Sprickan korsade ett av borrhålen i APSE-experimentet. Flöde och rörelse (i normal- och skjuvriktning) mättes under det att APSE-pelaren avlastades och sprickan visade ett starkt spänningsberoende flöde. Med anledning av detta bestämdes det att man skulla ta vara på den unika möjligheten och försöka bestämma det kombinerade spännings-flödesegenskaperna hos denna spricka i laboratorium.

De uppmätta värdena för normalstyvhet, skjuvstyvhet och pikhållfasthet skiljer sig inte nämndvärt åt mellan proven. Däremot sker betydande dilatation efter 2.25 mm skjuvning för Prov 1 medan det sker tidigare, efter 0.5 respektive 1.1 mm skjuvning för Prov 2 respektive Prov 3.

Fram till 2–3 mm skjuvning kan ”kubik-lagen”, med en justerande friktionsfaktor, användas för att förutsäga det kombinerade spänning/flödesbeteendet för Prov 1. Flödet i Prov 2 och Prov 3 verkar ha turbulenta inslag som inte kan försummas, och därför är ”kubik-lagen” inte tillräcklig för att uppskatta dess storlek. Andra faktorer som inte har studerats i detta projekt kan också påverka kopplad beteendet (dvs. gouge bildning).

Trots att de tre sprickproverna som testats i det här projektet är relativt stora, att de tillhörde samma stora spricka i APSE-tunneln och att de *in-situ* befann sig mindre än en meter ifrån varandra, är deras kopplade spänning/flödesbeteende påfallande olika. Det bekräftar hypotesen att för den här typen av starkt vattenförande sprickor, krävs en större yta för en representativ flödesbeskrivning, än ytan hos sprickproven som testades i det här projektet.

Contents

1 Introduction

1.1 Background

One of the recent experiments performed by the Swedish Nuclear Fuel and Waste Management Co (SKB) has been the Äspö Pillar Stability Experiment (APSE). This experiment was designed to demonstrate the ability to predict spalling in a fractured rock mass, to consider the effect of backfill on the rock mass response, and to compare the capabilities of 2D and 3D numerical models. The experiment was carried out at 450 m depth at the Äspö HRL. High stresses were induced by excavating a tunnel with curved floor and by boring two vertical boreholes of deposition hole size (1.8 m diameter) close to each other (Figure 1-1). To further increase the stress, the rock volume between the boreholes was heated. The effect of confining pressure was also studied by applying a uniform pressure of 0.7 MPa from a rubber blather to the wall of the first hole drilled. The pressure was maintained during drilling of the second hole and the heating phase. After the heating, the pressure was stepwise reduced while the rock mass response was monitored by acoustic emission (Andersson 2004).

One of the last phases of the APSE project involved the extraction of the pillar between the holes to study the effect of high stress concentrations obtained during the experiment. Before cutting and extracting the pillar, it had to be de-stressed. The de-stressing of the pillar was carried out by drilling a semicircular array of boreholes (Figure 1-2). During this phase of the APSE project a large field experiment was conducted with the aim of acquiring hydro-mechanical data during the drilling of the de-stressing slot.The de-stressing of the pillar was expected to cause a number of coupled hydro-mechanical effects in two highly conductive sub-vertical fractures intersecting borehole DQ0066G01 (Figure 1-2). Therefore, fracture displacements, fracture inflow and total inflow into borehole DQ0066G01 were monitored during the drilling of the de-stressing slot.

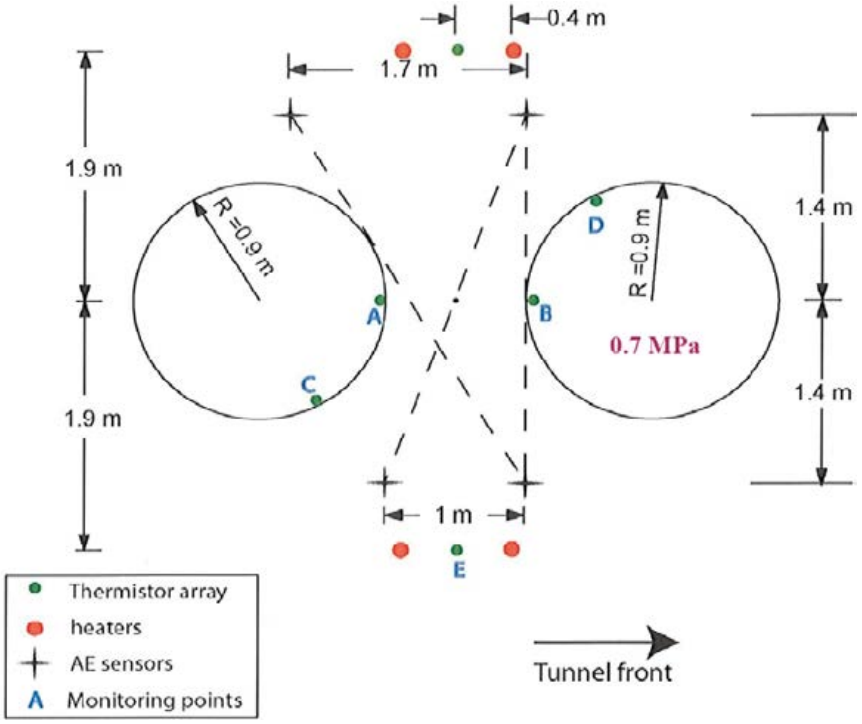

Figure 1-1. *Layout of the APSE experiment (Andersson 2004).*

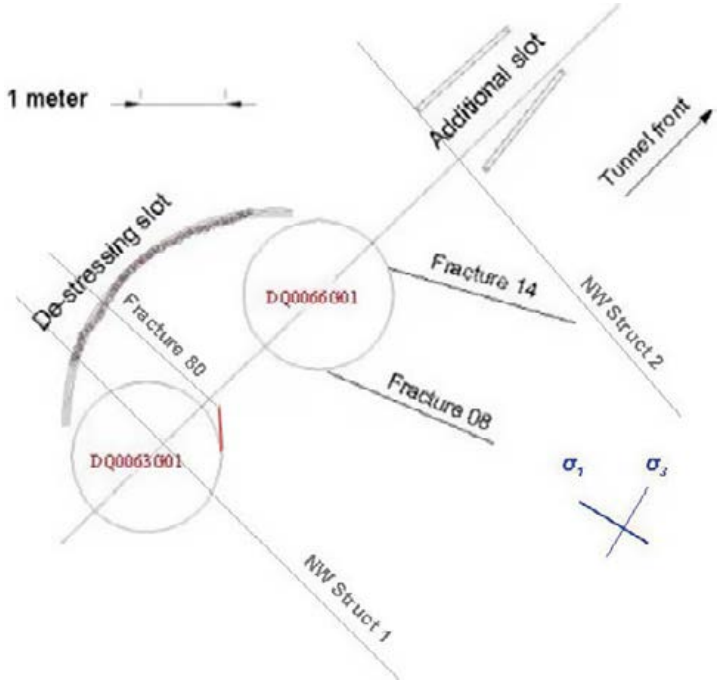

Figure 1-2. *Layout of the HM data acquisition experiment (Mas Ivars 2005) (not to scale). Fracture 08 is the fracture from which the samples were taken from.*

Fracture normal openings of up to 0.6 mm and shear displacements of up to 0.9 mm were registered during the drilling of the slot. The inflow coming from fracture 08 increased from 2.4 l/min to 4 l/min, and the inflow from fracture 14 increased from 6.1 l/min to 18 l/min. The water pressure was monitored during the experiment, making use of the Hydro Monitoring System, at several locations at the Äspö Hard Rock Laboratory to be able to assess the influence of the drilling of the de-stressing slot on the hydraulic response of the surrounding rock mass. Strong responses were registered at several locations (Mas Ivars 2005).

1.2 Motivation, objective and scope

Water flow in hard crystalline rocks occurs almost exclusively through fractures. The gathered data from the "Hydromechanical data acquisition experiment at the APSE site" clearly supports this fact (Mas Ivars 2005).

Due to changes in stress, groundwater movement, weathering, chemical reaction and erosion, fractures can be filled in, or washed open, fracture walls can displace, can be coated with minerals and fracture wall properties can be altered. During the drilling of the de-stressing slot at the APSE site, the stress acting on the two sub-vertical conductive fractures monitored changed. This change in fracture normal and shear stress can cause mechanical aperture change and in turn hydraulic aperture change with the subsequent influence in the fracture flow. Besides, any induced shear displacement can ultimately cause fracture dilation and it can produce flow channelling effects which can increase or decrease the flow through the fracture depending on the initial fracture wall geometry.

In order to better understand the results obtained in the HM data acquisition experiment at the APSE site (Mas Ivars 2005) it is first needed to understand the single fracture coupled hydro-mechanical behaviour. For this reason two large diameter boreholes (30 cm diameter) were drilled in one of the sub-vertical conductive fractures monitored (fracture 08 in Figure 1-2) in the field experiment. The cores, being of good quality (Figure 1-3), provided a unique opportunity to perform coupled stress-flow tests on large fracture samples from a very conductive fracture belonging to the NW-SE, sub-vertical fracture set that is responsible for most of the water flow at the Äspö HRL (Magnor 2004). The longer core (KQ0065B01) was bored at 1.5 m depth from the floor of the APSE tunnel. The shorter core (KQ0065B02) was drilled at a depth of 2 m under the floor of the tunnel.

Figure 1-3. *Borehole cores from which the fracture samples were cut.*

The planned set of coupled laboratory tests would supply information about the flow rate through the fracture, hydraulic aperture, Reynolds number, etc, under controlled boundary conditions. Additionally, the fracture walls of the three samples would be scanned before and after the test by a three-dimensional laser scanner to obtain information about their geometrical characteristics and to allow the derivation of the fracture mechanical aperture. The results from the laboratory test and the laser scanning would provide a valuable data set to improve our knowledge on the coupled behaviour of this type of structures, and they could be relevant in transport studies and groundwater flow related studies.

2 Equipment and test planning

For the planning of the stress-flow tests it was necessary to have an idea about the magnitude of the stresses acting on the fracture plane from where the drill cores had been obtained, during the drilling of the de-stressing slot. There were no stress measurements while drilling the de-stressing slot. For this reason, and to better understand the previous field studies conducted at the APSE site, a three-dimensional mechanical numerical analysis of the redistribution of the stress during the drilling of the de-stressing slot was carried out (Mas Ivars 2006) with the distinct element code 3DEC (Itasca 2003). This simulation included the effect of the main fractures in the study volume, one of which was fracture 08 (see Figure 1-2).

2.1 Coupled stress flow test

Three samples were cut and moulded into concrete by Ulf Stenman at Testlab, LTU (Luleå Tekniska Universitet). Only healthy parts of the fracture (i.e. parts of the fracture with no visible side fractures or small cracks) were chosen for the fracture samples in order to avoid leakage of water through the intact rock part. Sample 1 was cut from core KQ0065B02 with a fracture area of 13 cm × 13 cm and sample 2 and 3 were cut from core (KQ0065B01) with an area of 15 cm × 15 cm. The fracture samples were quadrangular in shape (Figure 2-1).

2.1.1 Laboratory test equipment

The set of laboratory stress-flow tests presented in these report were performed by Thomas Forsberg at TestLab, LTU. The equipment used for the tests is described in the following sections.

The shearing unit

The shearing unit consists of a highly reinforced steel frame (Figure 2-2) in which the lower part of the sample is firmly attached.

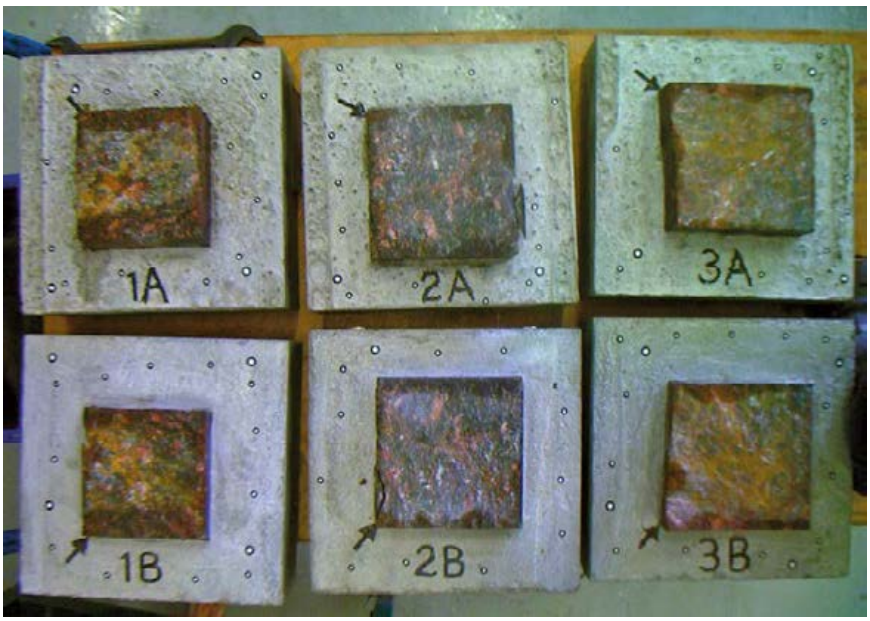

Figure 2-1. *The three fracture samples opened after the tests have been performed.*

Figure 2-2. *Shearing frame in grey with shearing system in red. Log system in the right of the picture.*

Shearing is performed by two hydraulic 500 kN actuators which act in one direction each. The upper part of the sample is sheared to the left while the lower part remains stationary or fixed. The shearing rate is controlled by a steering unit built by Nobel AB. Further, the shearing system consists of two arms connected to a rigid steel junction, where the upper part of the sample is attached (Figure 2-3). The upper end of the sample is attached to the gap with heavy bolts.

Two heavy steel bars are attached on each side of the opening in order to stiffen the middle of the frame to prevent the frame of horizontal deformation. After the sample has been inserted, two stretchers are applied over the gap so that the high forces during shearing won't deform the gap by widening it rather than shearing the rock pieces. One of the steel bars and the stretcher in black paint may be seen in Figure 2-2.

The entire shearing system in red (Figure 2-2 and 2-4) is freely attached to the frame with springs. The spring system allows the moving parts in the shearing system to rotate some ± 10 degrees in the line of shearing and also follows vertical change with approximately 50 mm. Ahead of shearing the hydraulic system pre-stretches the arms in order to be able to locate the gap in the centre position. As a result of the pre-stretching, a distinct and stiff response is achieved during the shearing phase of the sample.

Normal force is applied by a 500 kN hydraulic actuator situated on top of the sample, inside the steel frame. It has a stroke capacity of ± 20 mm. The actuator is equipped with a digital servo valve that is controlled by a program supplied by MOOG. The force that compresses the sample is transferred down to the sample through a spherical bearing and further down through an oil lubricated flat slide bearing down to the upper joint for the samples. The force is measured by a load cell and the stroke determined by a LVDT (Figure 2-5).

The oil lubricated flat slide bearing (hydraulic bearing) works as a frictionless joint between the normal force actuator and the horizontally moving system in the shear box thus allowing frictionless horizontal displacement of ± 25 mm sideways and ± 50 mm in shearing direction. Vegetable oil is compressed by a hydraulic pump and let out between two steel plates.

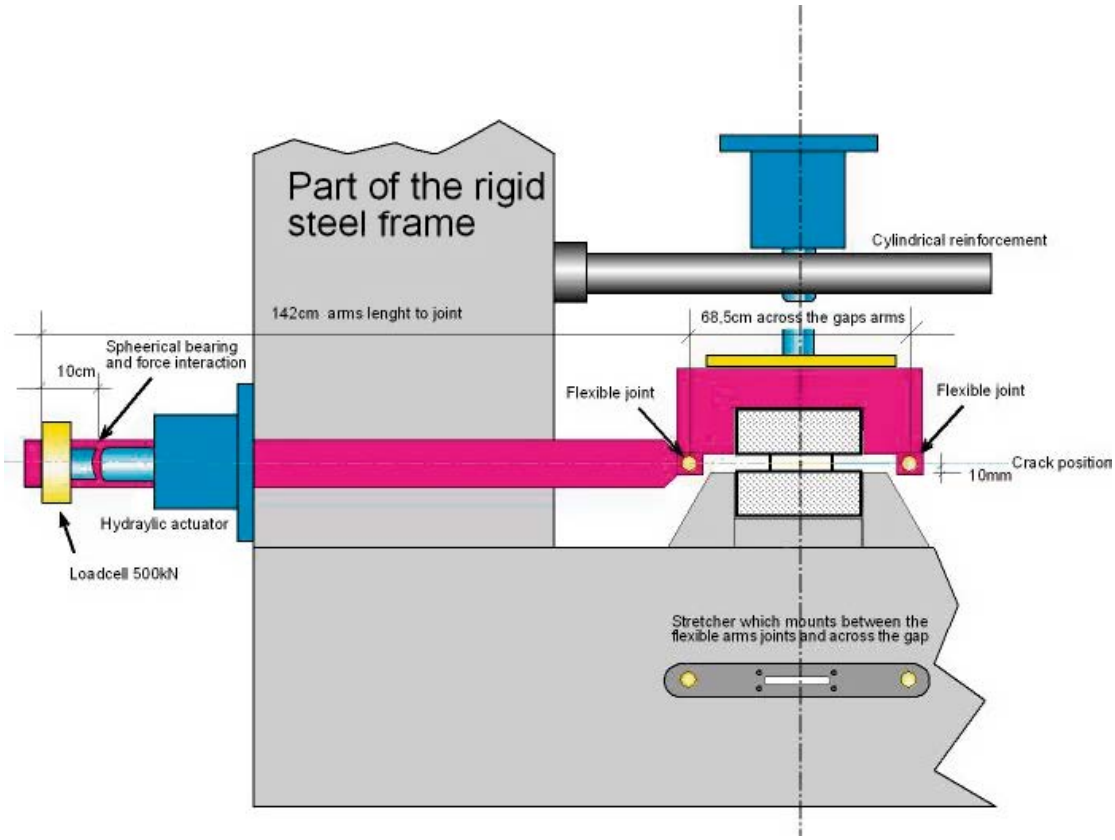

Figure 2-3. *Schematic representation of the direct shear device.*

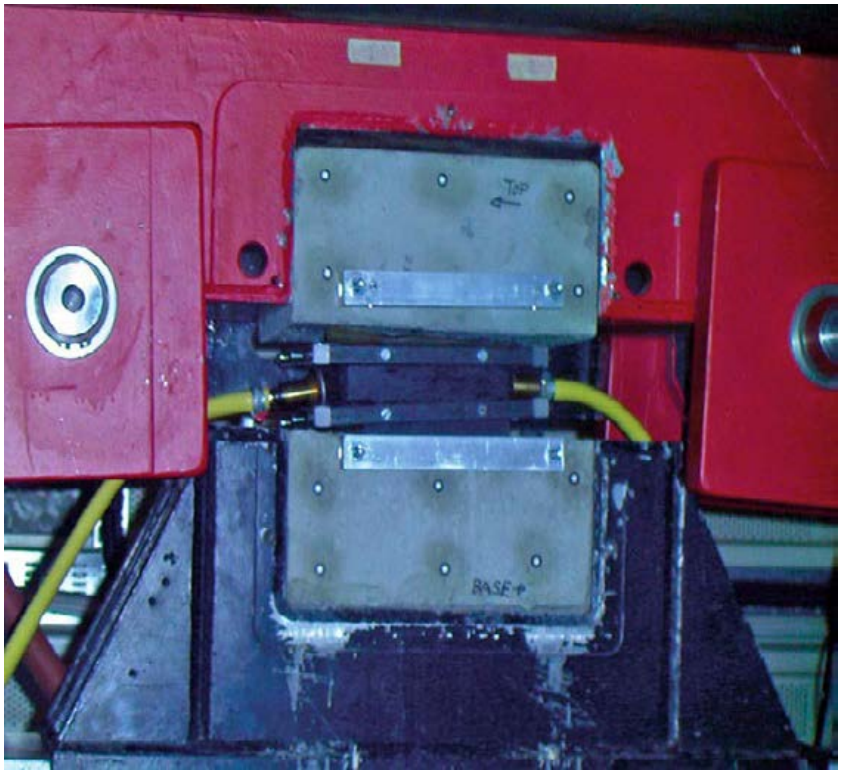

Figure 2-4. *The mounting gap where the sample is attached. The picture shows a sample with high neck and the water supplying system attached (the yellow hoses).*

Figure 2-5. *Normal force actuator and the system for distributing the force down on top of the sample.*

A large amount of oil is flushed through the system and needed to be returned back to the hydraulic pump. This is achieved by a subsystem; which filters the collected oil and pumps it back to the main vegetable oil system. Vegetable oil is used in order to minimize the environmental and health effects.

Transducers for displacement monitoring (LVDT)

As shown in Figure 2-5, the shearing unit has a central transducer (LVDT), located over the normal force actuator, which records the vertical displacement.

Four LVDTs (Linear Variable Differential Transformer) perpendicular to the sample's fracture (two on each side) measure the opening/closure of the fracture during the test (Figure 2-6). Holders are glued on the side of the concrete mould and the signals from the four transducers are logged together with the other signals. LVDT 1 and LVDT 2 are both in the same side of the fracture. Similarly, LVDT 3 and LVDT 4 are both in the same side of the fracture, opposite to the side where LVDT 1 and 2 are placed. Besides, LVDT 1 and LVDT 4 are situated close to the outlet of the water, while LVDT 2 and LVDT 3 are close to the inlet of the water.

To mount the set of LVDTs, aluminium holders are fixed to the sides of the concrete cast together with a mounting plate so that the LVDTs are separated 120 mm in height and 150 mm in side distance.

The set of LVDT holders and sliding bar (Figure 2-7) are glued on to the side of the concrete with X60-glue. The glue is applied on the heads of the bolts and compressed against the concrete with wing screws that are mounted on to the stretchers (Figure 2-8).

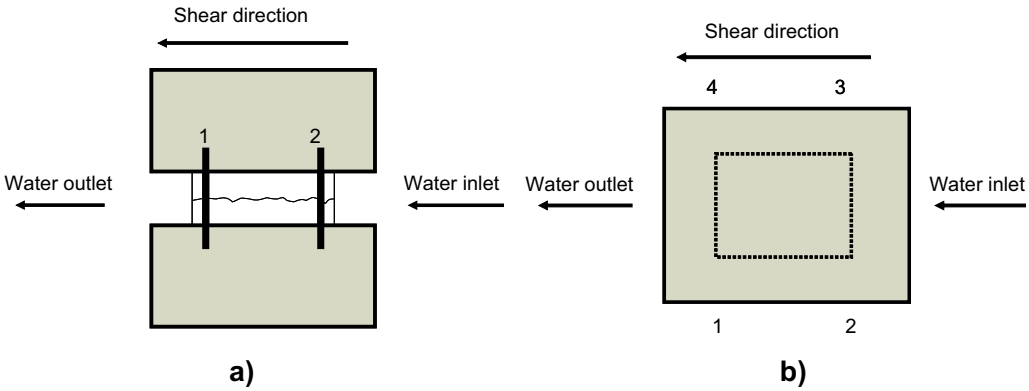

Figure 2-6. *a) The fracture sample mounted viewed from side. LVDT 1 and LVDT 2 are shown. b) The fracture sample mounted viewed from above. LVDT 1–LVDT 4 are shown.*

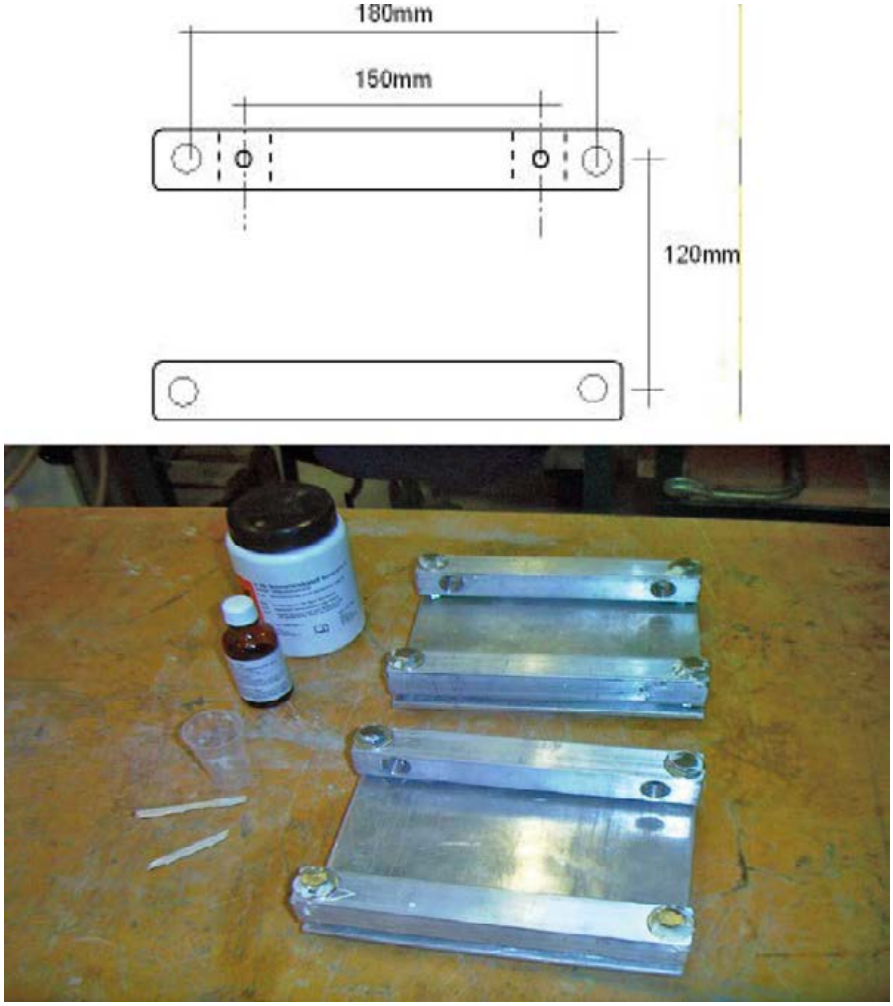

Figure 2-7. *The fixation tools for mounting the LVDTs along the side of the samples.*

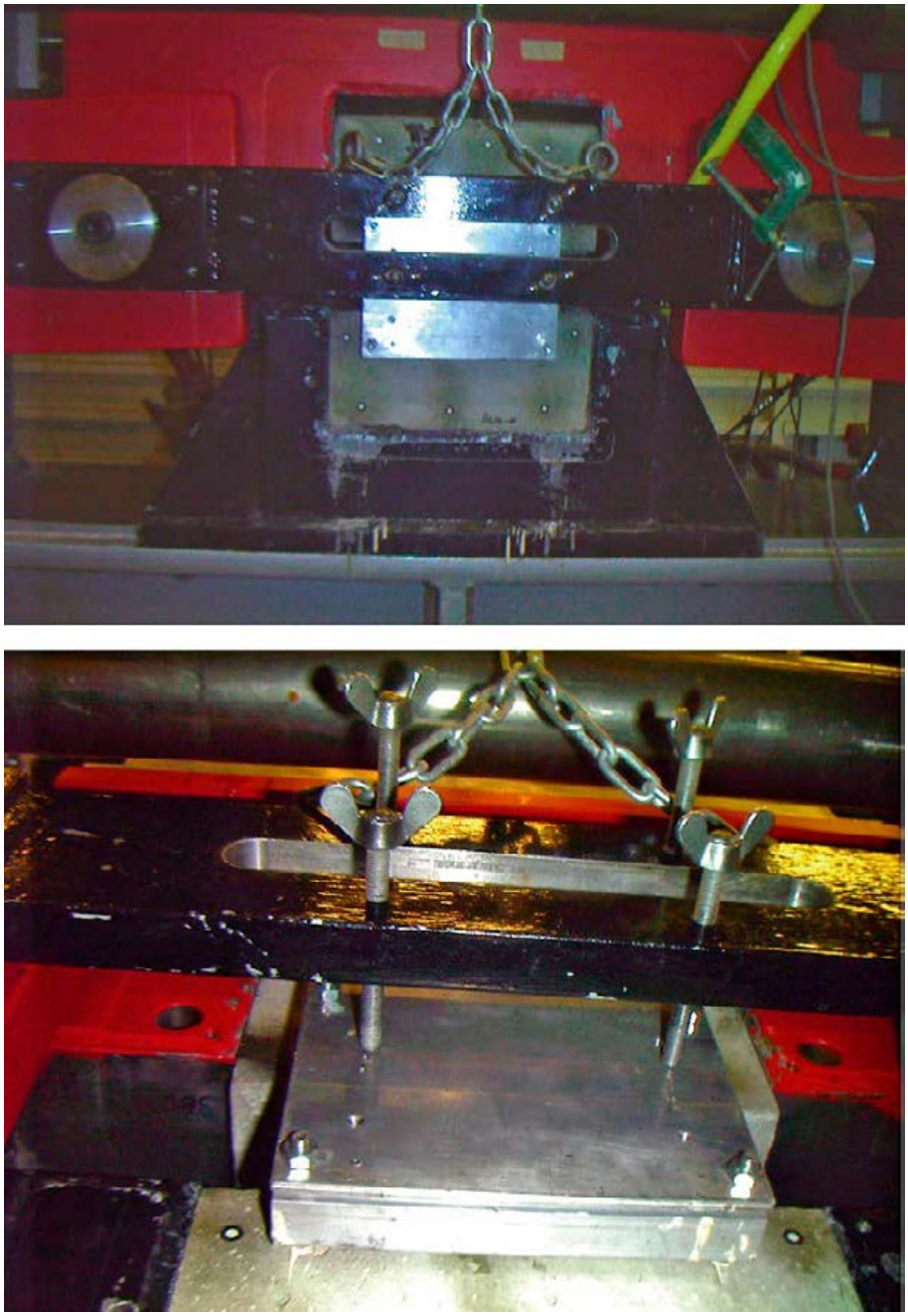

Figure 2-8. *The fixation tool compressed by the wing screws on the stretchers.*

After the glue has hardened, the mounting plates are removed leaving the holders glued on to the side of the concrete. Then, when the LVDTs are mounted in the holders, any opening/closure of the fracture could be recorded and evaluated (Figure 2-9).

Tests with water

The samples are sheared at the same time as water is flowing through the crack in the direction of shearing. To calculate the permeability after the tests, the out flowing water is collected and measured. This is achieved by a system with an open vessel that is supplied with tap water through an inlet (Figure 2-10). Circulating water is allowed to flush out through an outlet in a high position, leaving an open water surface at a fixed level. From the lower end of the vessel is another hose connected that supplies water to the samples “high end”. Water is forced through the fracture over to the other side, the “low end”, where collected. Another hose gathers the through flow of water and leads it into a bucket hanging in a load-cell. The load-cell is logged and the amount of flowing water determined.

Figure 2-9. *LVDTs mounted into the holders after the guide aluminium plate has been removed.*

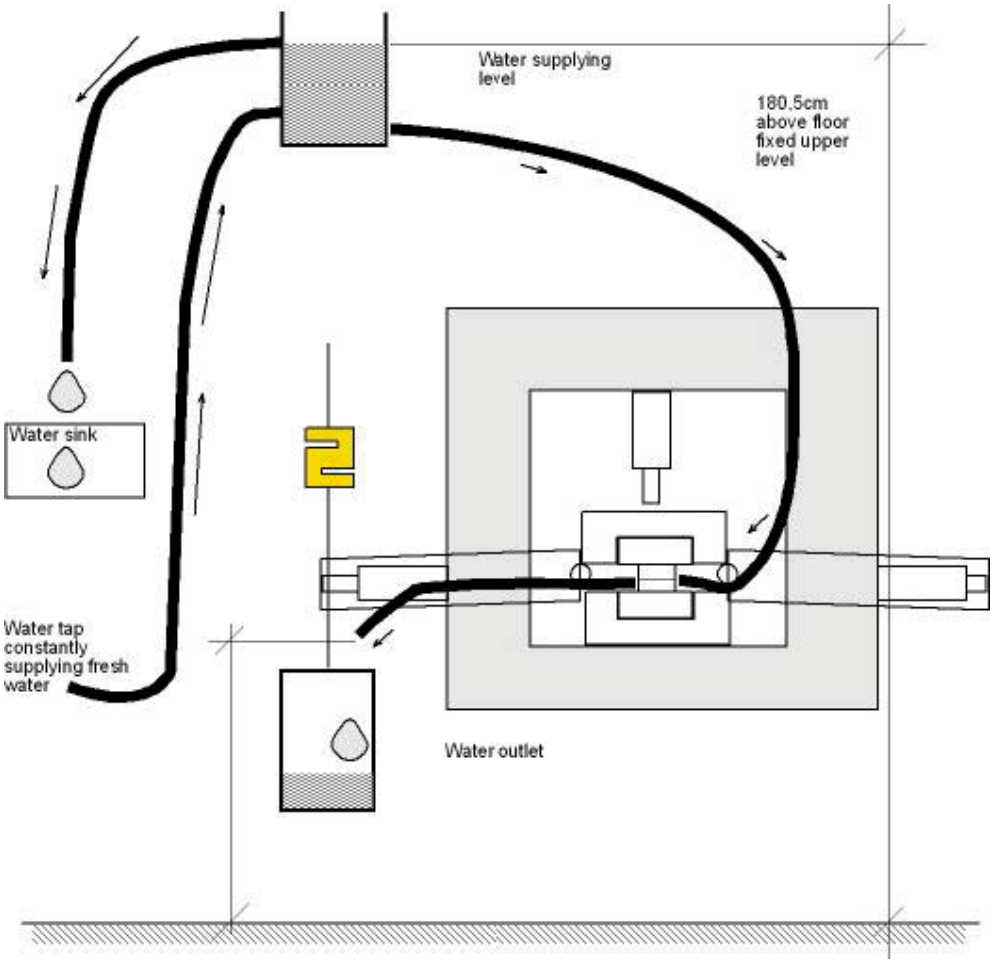

Figure 2-10. *Water supply system.*

In order to seal off two of the sample fracture sides in each sample, a sealing system was constructed (Figure 2-11).

The sealing system consists of rubber tube, with inlet and outlet through a quick joint for the hoses. A white filter is attached on the inside of the rubber seal, on the inlet and outlet sides, so that water is distributed over the entire crack length (Figure 2-12).

Over and under the fracture plane, two steel frames were situated surrounding each sample. On each side of the sample, over and under the fracture plane, a clamp is compressed against the rubber seal so that water doesn't escape out from the seal. Over and under the fracture plane a reinforcement frame is attached. The reinforcement frame is built so that the upper and lower part of the sample may be separated without loosing contact along the crack (Figure 2-13).

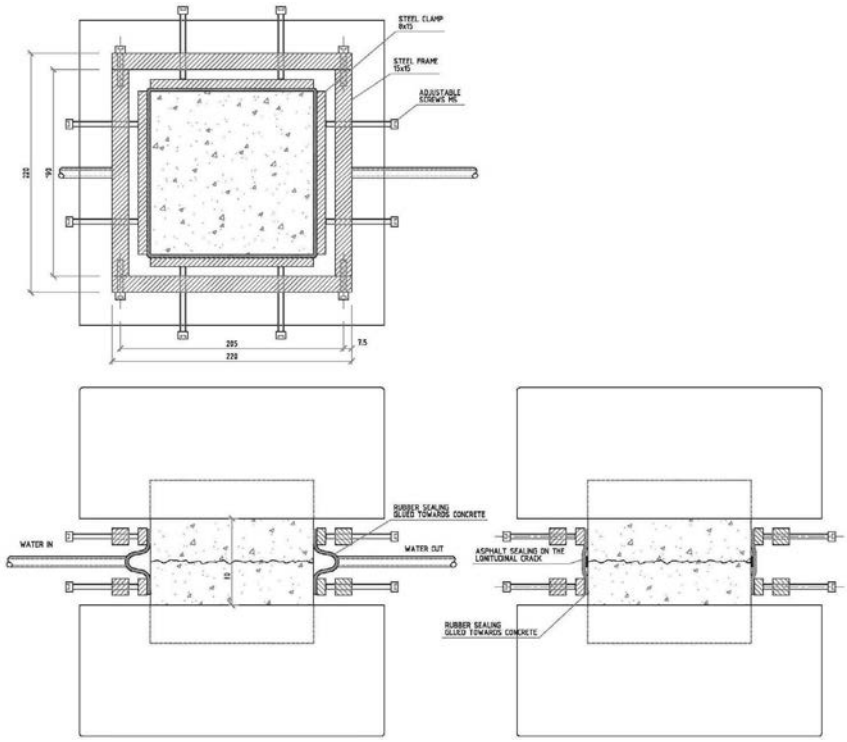

Figure 2-11. *Fracture sealing system.*

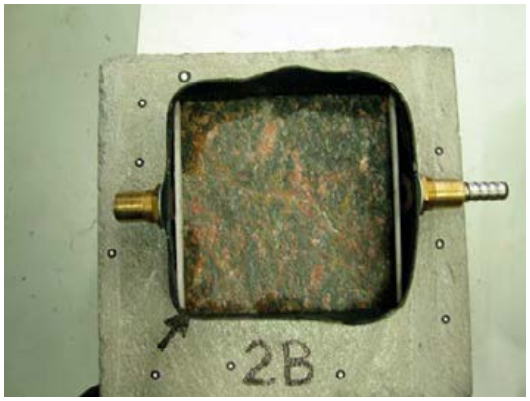

Figure 2-12. *Sample, rubber tube, filters and quick joints for water inlet and outlet.*

Figure 2-13. *Reinforcement frame (picture above) and complete sealing system (picture below).*

In order to allow the sealing system described above to be installed in the samples, it was required to leave a larger portion of the rock out of the mould. Because of this the total sample height became larger than usual and the system had to be slightly modified.

Technical specifications

The reinforced steel frame is manufactured by a company in Luleå called Eric Erlandsson AB and it is equipped with devices according to the list below:

- One digitally controlled actuator for normal force of the type Bradford Cylinders ltd. 500 kN Model MDT BC21197 M.W.P. 207 bar code: 200 × 50 mm with plunger diameter 110 mm.
- Digital servo valve: MOOG 0633 303A typ:P02K01M5M2.
- Normal load: Sensotech type 41/576-01 0–100.000 lbs (500 kN).
- Normal stroke: LVDT by HBM. Type:LSF/50 mm.
- Normal stroke amplifier: HBM Scout 55 with analogue output.
- Shearing: Two actuators INSTRON, 500 kN Model 0633 303A type P with hydraulic servo valves, plunger diameter 110mm.
- Shearing load: Sensotech type 41/576-01 0–100.000 lbs.
- Shearing stroke: LVDT Shaevitz type:RAG Stock no 1132332 S/N:2000 HR12635 stroke 250 mm.
- Shearing controlled by a servo amplified signal processor manufactured by Nobel AB with capacity 10–500 kN and 0–5 mm/minute and named Shear Rig Regulator 1 (SRR-1).
- Crack measurement: Four WSM LSC transducers 25 mm stroke.
- Water permeability measurement: Load cell Load transducer U4000 250 kgf.
- Data logger: HBM's Spider-8.
- Measuring program: HBM's Catman version 5 release 2.0.
- Normal load controlled by a program: MOOG V310.001.
- External calibration load cell: Bofors LS-1 50MP.
- External calibration load amplifier: Nobel BKI-5.

2.1.2 Test plan

Laboratory normal stress/flow and shear stress/flow test on three fracture samples from the APSE tunnel were performed at Testlab (LTU). First a set of normal load/flow tests was carried out to determine the variation of the flow rate with increasing/decreasing normal load. The shear/flow tests were performed with constant normal load boundary conditions.

Normal stress-flow test

For each fracture sample four coupled normal load/flow tests were carried out in order to obtain the variation of the flow and hydraulic aperture of the fracture with increasing/decreasing normal load, and to achieve in-situ initial conditions before shearing.

The normal load varied from 0 to 6 MPa and was applied in increments of 2 MPa (Figure 2-14). Water flowed continuously through the fracture and the flow rate was measured at each of these load stages. The fourth and last cycle stopped at 2 MPa. This would be the initial normal load for the following shear/flow test.

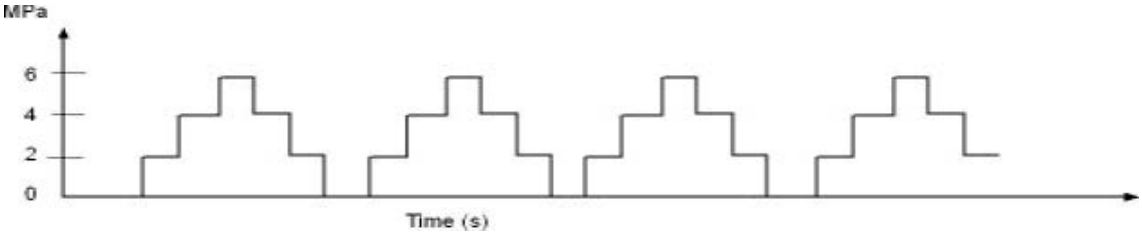

Figure 2-14. *Loading scheme for the four cycles of normal loading/unloading.*

The residual or minimum normal load that the equipment can handle is 16 kN so the minimum normal stress, taking into account the different sample's areas, was 0.97 MPa for sample 1 and 0.73 MPa for sample 2 and 3.

A constant head of 67.5, 65.5 and 62.5 cm was applied as hydraulic boundary condition to Sample 1, Sample 2 and Sample 3 respectively. The hose providing the water to the sample had a large diameter in order to prevent any head loss before the water inlet (Figure 2-15).

Shear displacement-flow test

After the normal stress/flow tests, a shear/flow test was run on the same fracture sample with initial normal load 2 MPa under constant normal load boundary conditions.

The samples were sheared 6 mm with a shear rate of 0.1 mm/minute. Every 0.25 mm of shear displacement, shearing was stopped until the water flow was stabilized so that the flow could be calculated after the tests.

As for the case of the normal load-flow tests, a constant head of 67.5, 65.5 and 62.5 cm was applied as hydraulic boundary condition to Sample 1, Sample 2 and Sample 3 respectively.

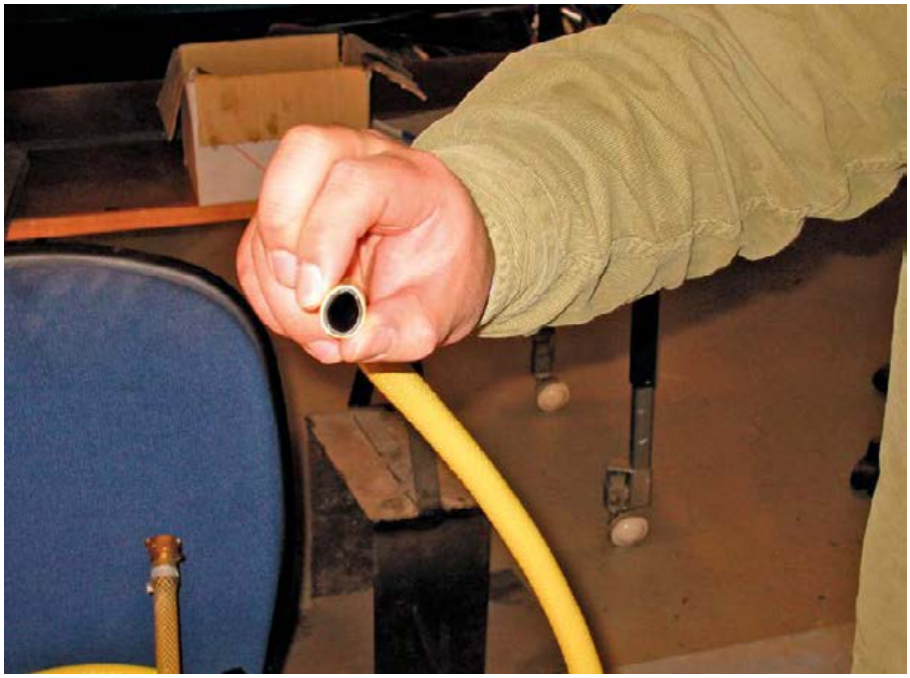

Figure 2-15. *Detail of the hose diameter.*

2.2 Three-dimensional laser scanning

Three-dimensional laser scanning (Figure 2-16) of both walls of each fracture was performed by Jimmy Gidö Schön (Svensk Verktygsteknik AB) before and after the stress-flow tests were carried out. The laser scanner had an accuracy of 30µm. This allowed to accurately characterize the surfaces of the fracture walls and to obtain the fracture mechanical aperture. The fracture mechanical aperture was estimated by importing the two scanned fracture surfaces of each sample to their measured location and calculating the aperture in between. It is important to note that the mechanical aperture was therefore estimated under the normal stress induced by the self-weight of the upper part of the fracture sample. The measurements of the mechanical aperture after the test were conducted by importing the laser-scanned data of the upper part of the sample to its original position, exactly on top of the lower part of the fracture (i.e. the mechanical aperture after each test was measured in the pre-sheared fracture position) while the flow test results reflect the behavior of sheared fractures. The samples were cleaned before performing the laser scanning after the tests.

Making use of these data, basic statistical parameters could be derived for the three fracture samples. Besides, the experimental variograms of the mechanical aperture of each fracture sample have been obtained. This has allowed for a preliminary geostatistical characterization of the three fractures.

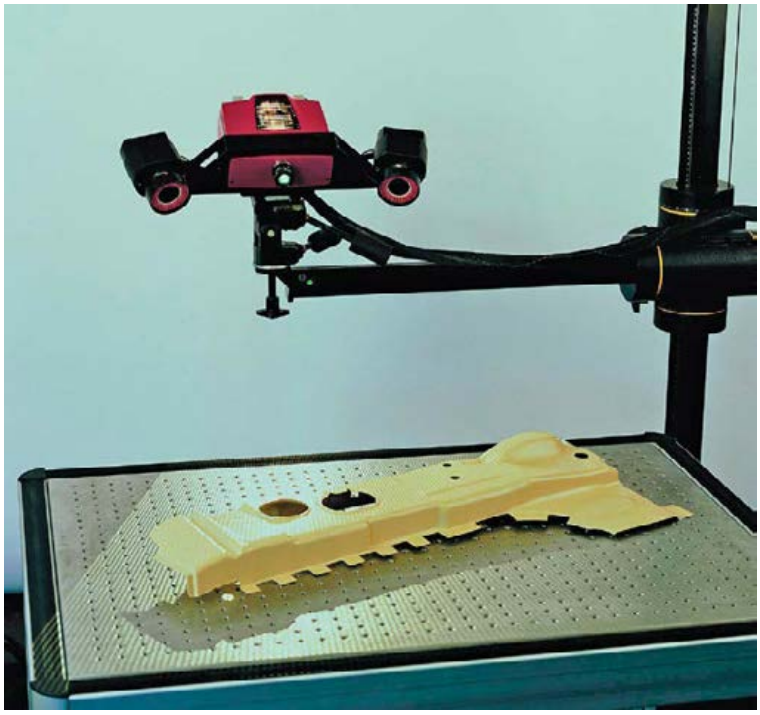

Figure 2-16. *Three-dimensional laser scanner from Svensk Verktygsteknik AB.*

3 Results

This chapter of the report contains the results from this study. First, mechanical aperture contours of the three fracture samples before and after the stress-flow tests are presented. After that, results from an exploratory data analysis of the mechanical aperture data are presented. The final sections of this chapter contain the results derived from the coupled normal load-flow tests and the coupled shear displacement-flow tests.

3.1 Samples description

This section presents contour plots of the mechanical aperture of the three fracture samples before and after the stress-flow tests were conducted (Figure 3-1 to Figure 3-9). The mechanical aperture of the three samples was derived from the three-dimensional laser scanning data of the topography of the fracture walls.

The shear displacement and the water flow were on the positive y-direction referred to this set of contour plots (bottom to top of the page). This direction agrees well with the expected main direction of the water flow and fracture shear that occurred during the "Hydromechanical data acquisition experiment at the APSE site" (Mas Ivars 2005).

From the contour plots we can see that even if the three fracture samples come from the same fracture in the APSE area, they have quite different aperture maps. Sample 1 is marked by the large open channel crossing all the way through the fracture plane (Figure 3-1). However, the channel is assumed to have a relatively small influence on the flow in our test due to the fact that it does not connect the inlet to the outlet of water and it mainly runs in the perpendicular direction to the flow. Besides the channel, it is important to notice than in the lower aperture ranges (Figure 3-2 and Figure 3-3) the low aperture areas (blue) are quite scarce compared to those on Sample 2 and Sample 3. The low aperture areas in Sample 1 seem to have a NW-SE orientation (referred to the plots) that is not clear in Samples 2 and 3. Sample 2 and Sample 3 are more similar to each other in the sense that the larger aperture areas (red) are located mainly in the boundaries of the samples and they both have abundant low aperture areas (blue) if we look at the small aperture range figures (Figure 3-6 and Figure 3-9).

Another aspect worth noticing is the fact that Sample 1 has a much smaller low aperture area than Samples 2 and 3 not only before the test but also after the test (Figure 3-3, Figure 3-6 and Figure 3-9).

Figure 3-4 to Figure 3-6 show how Sample 2 has suffered some damage during testing in its upper border.

Considering all three fracture samples, it is easy to observe how the low aperture total area (blue areas in the figures) grows after the coupled tests have been performed. This effect is much more pronounced in Samples 2 and 3 than in Sample 1.

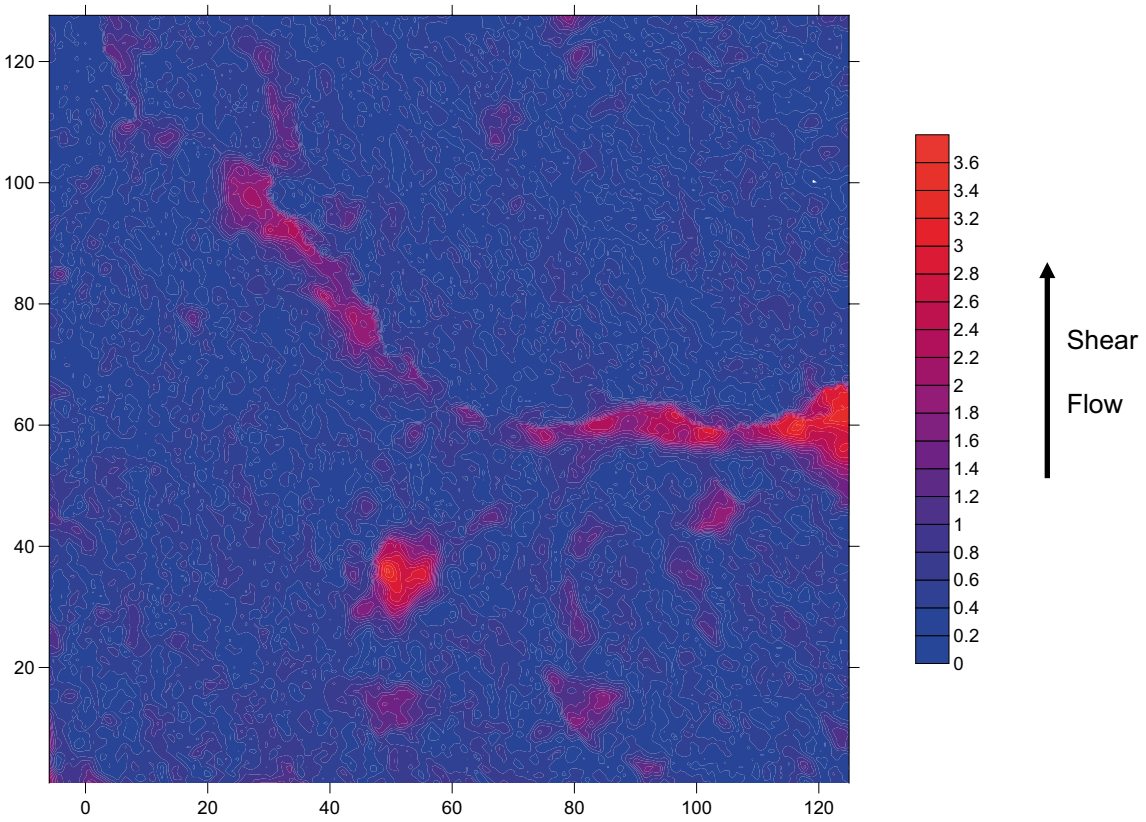

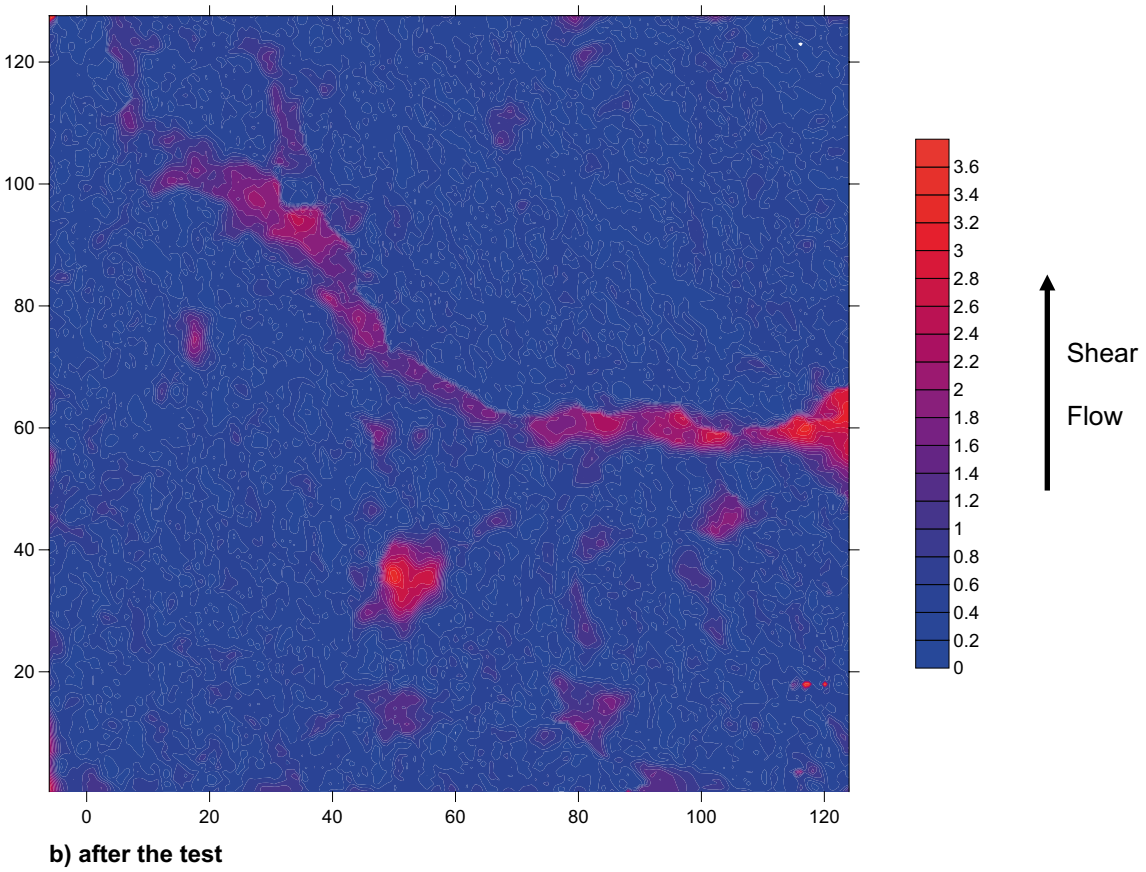

Figure 3-1. *Aperture contours in mm for Sample 1 (whole aperture range).*

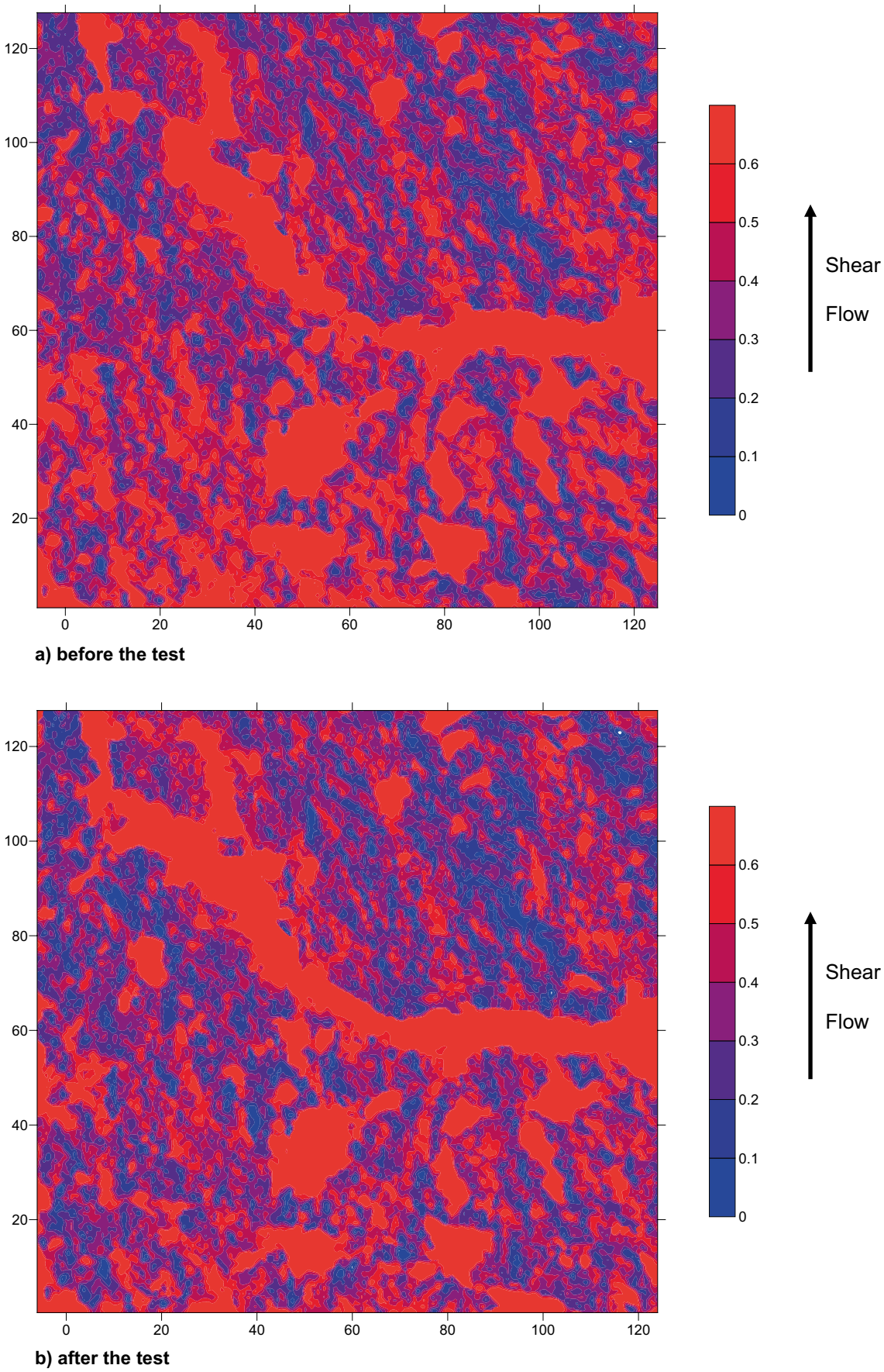

Figure 3-2. *Aperture contours in mm for Sample 1 (medium aperture range).*

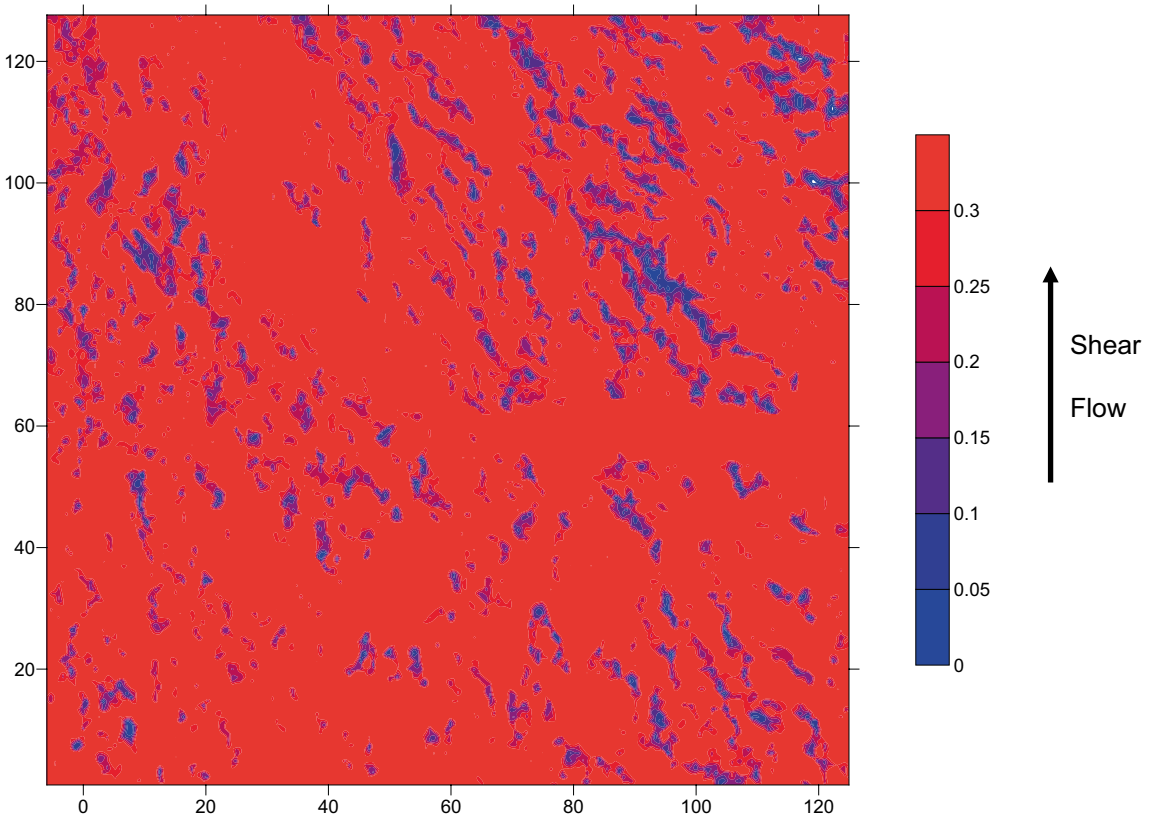

a) before the test

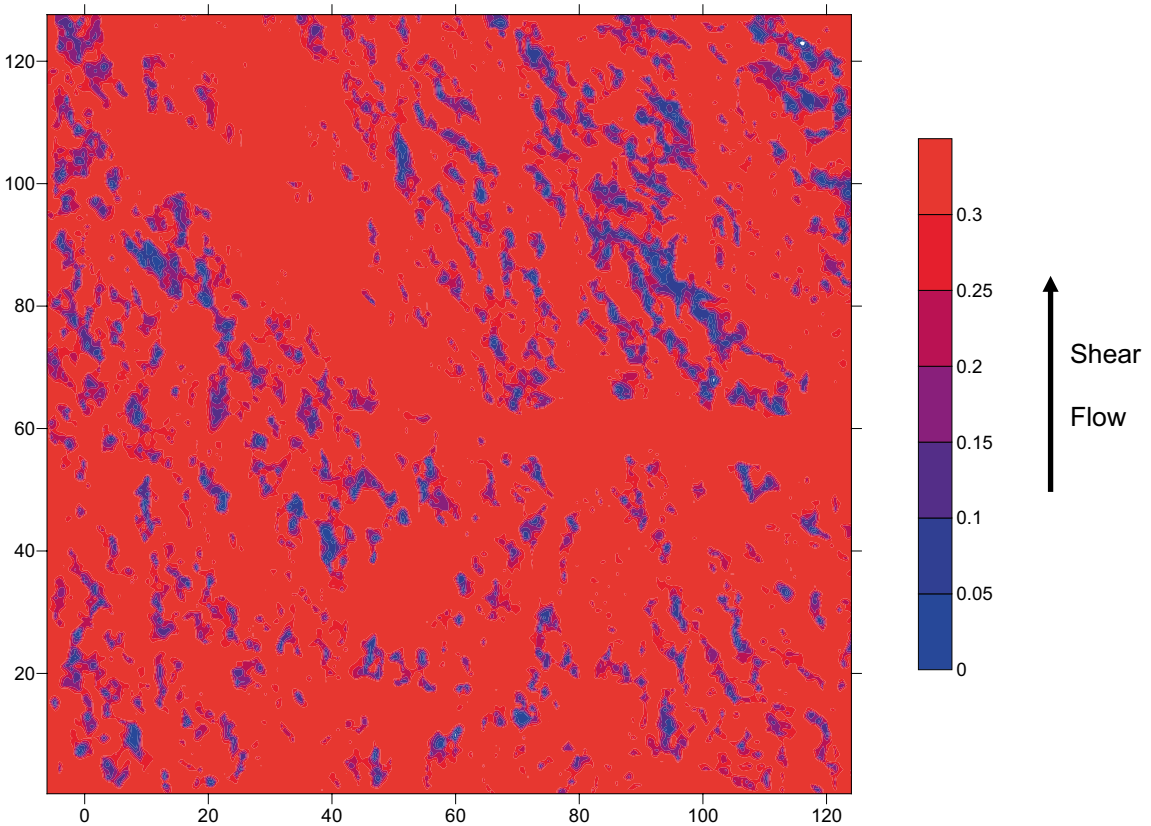

b) after the test

Figure 3-3. *Aperture contours in mm for Sample 1 (small aperture range).*

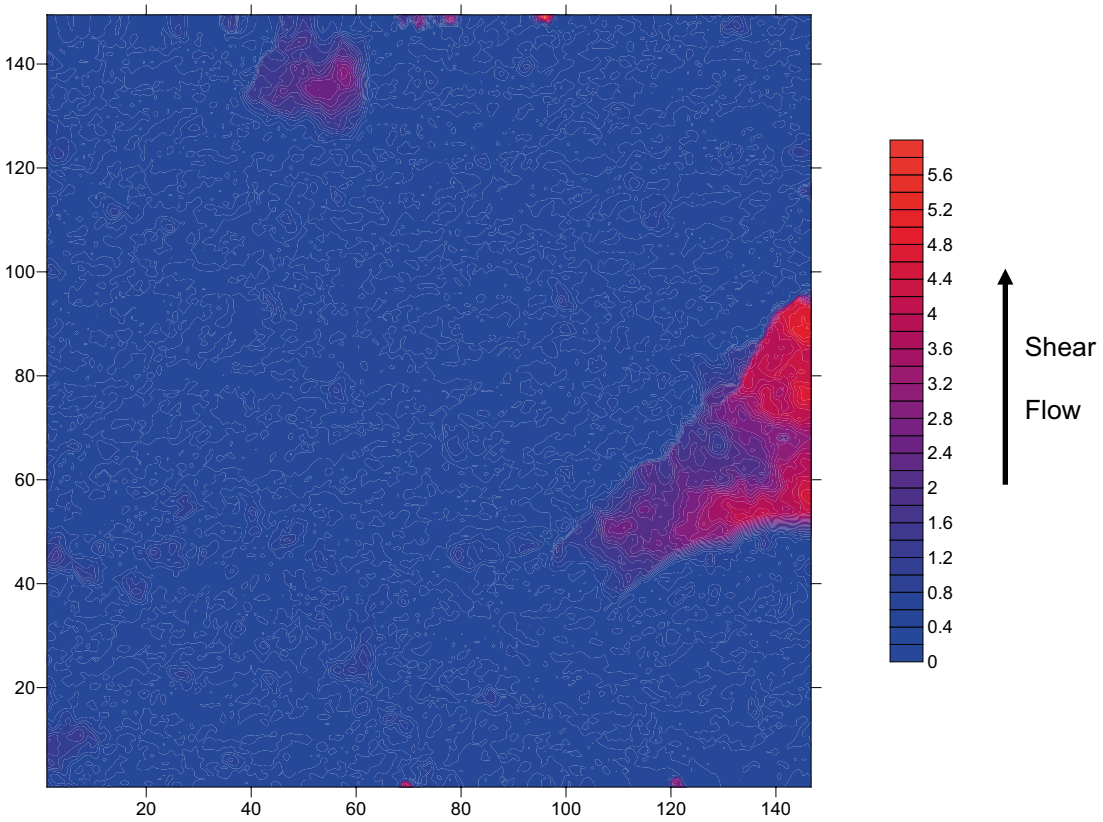

a) before the test

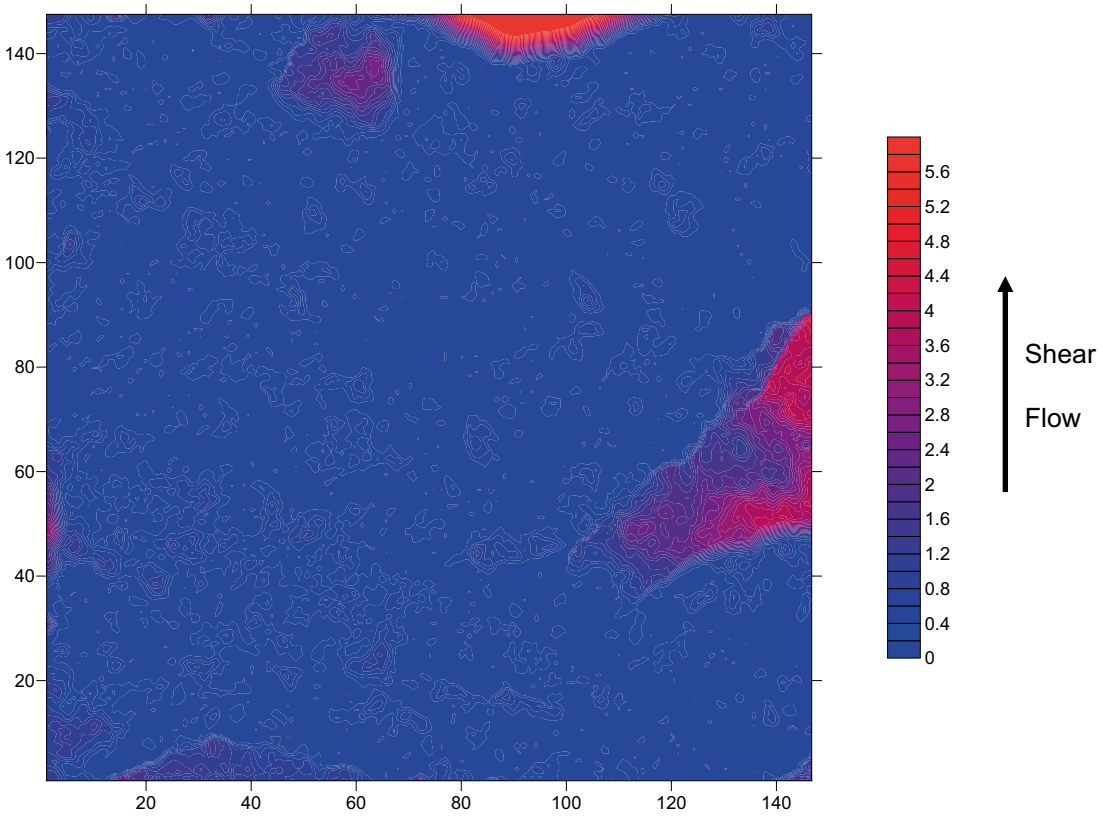

b) after the test

Figure 3-4. *Aperture contours in mm for Sample 2 (whole aperture range).*

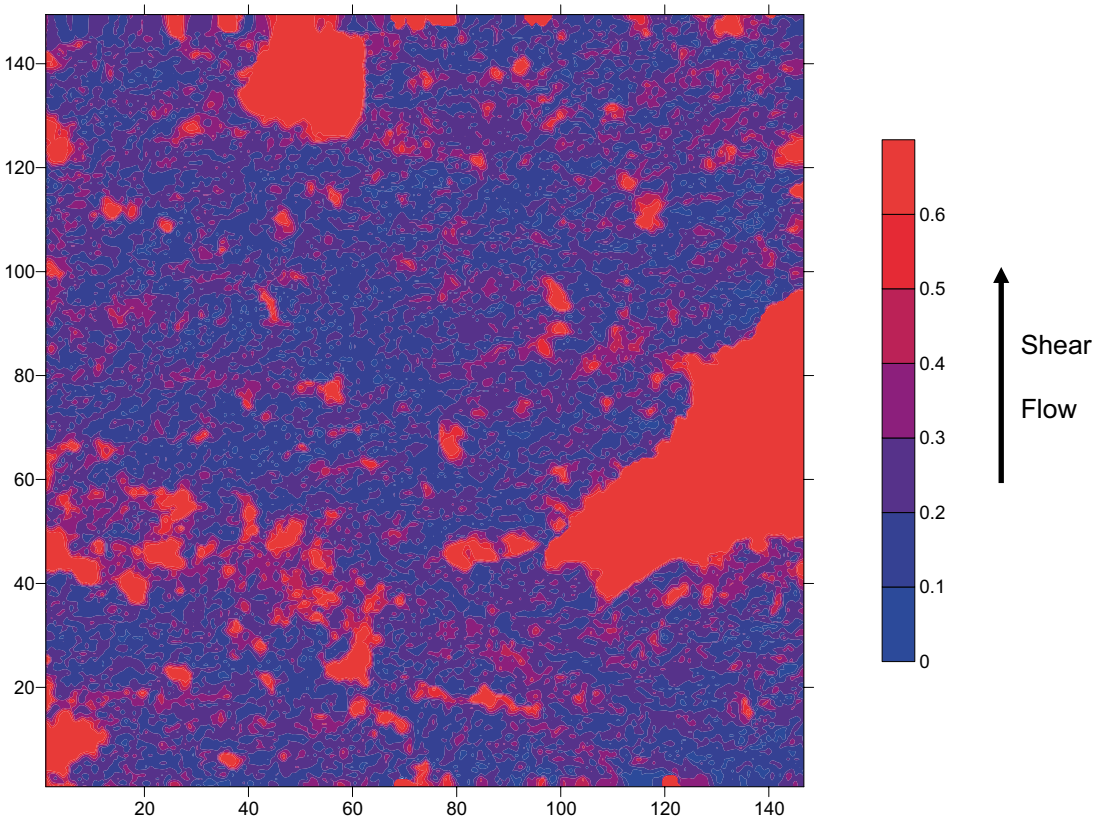

a) before the test

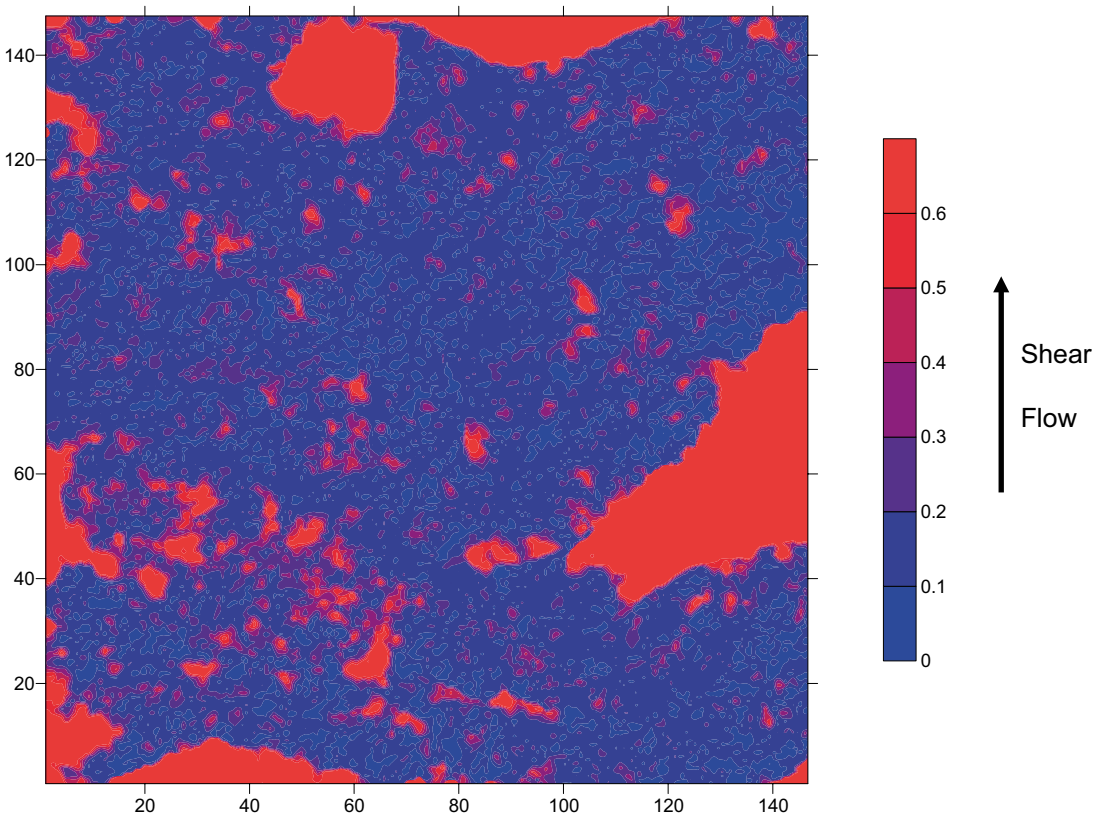

b) after the test

Figure 3-5. *Aperture contours in mm for Sample 2 (medium aperture range).*

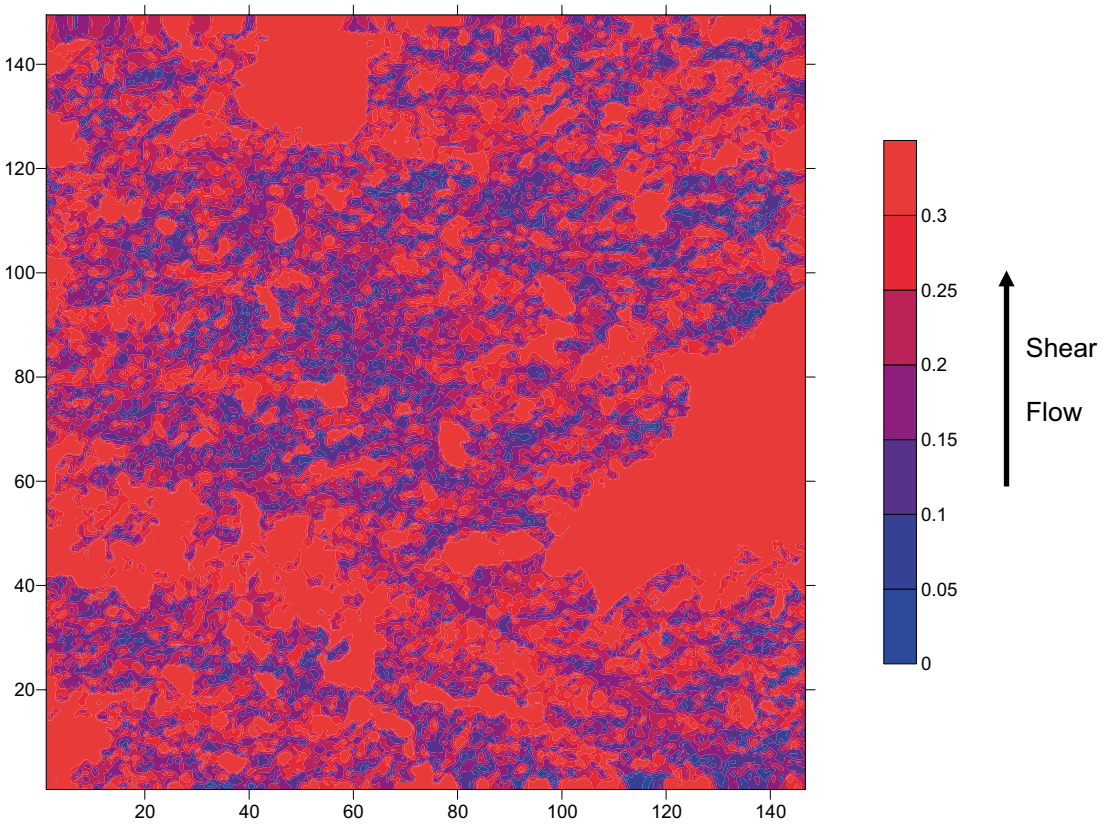

a) before the test

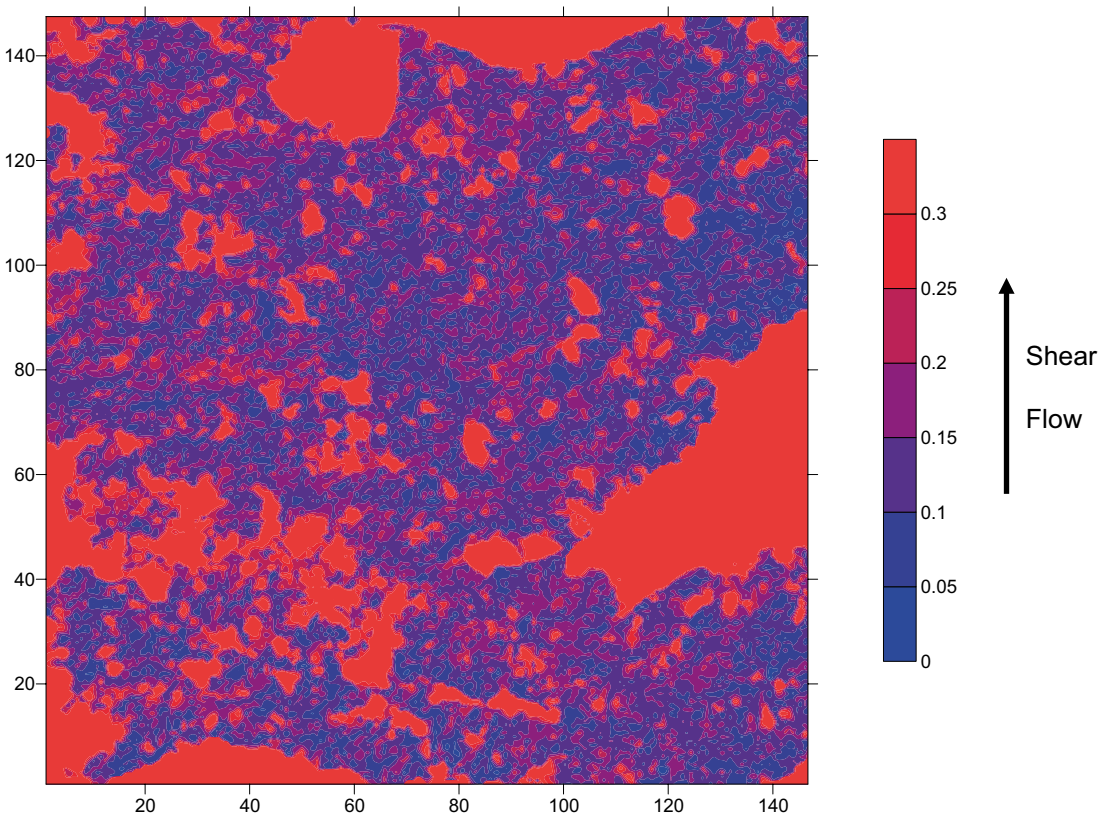

b) after the test

Figure 3-6. *Aperture contours in mm for Sample 2 (small aperture range).*

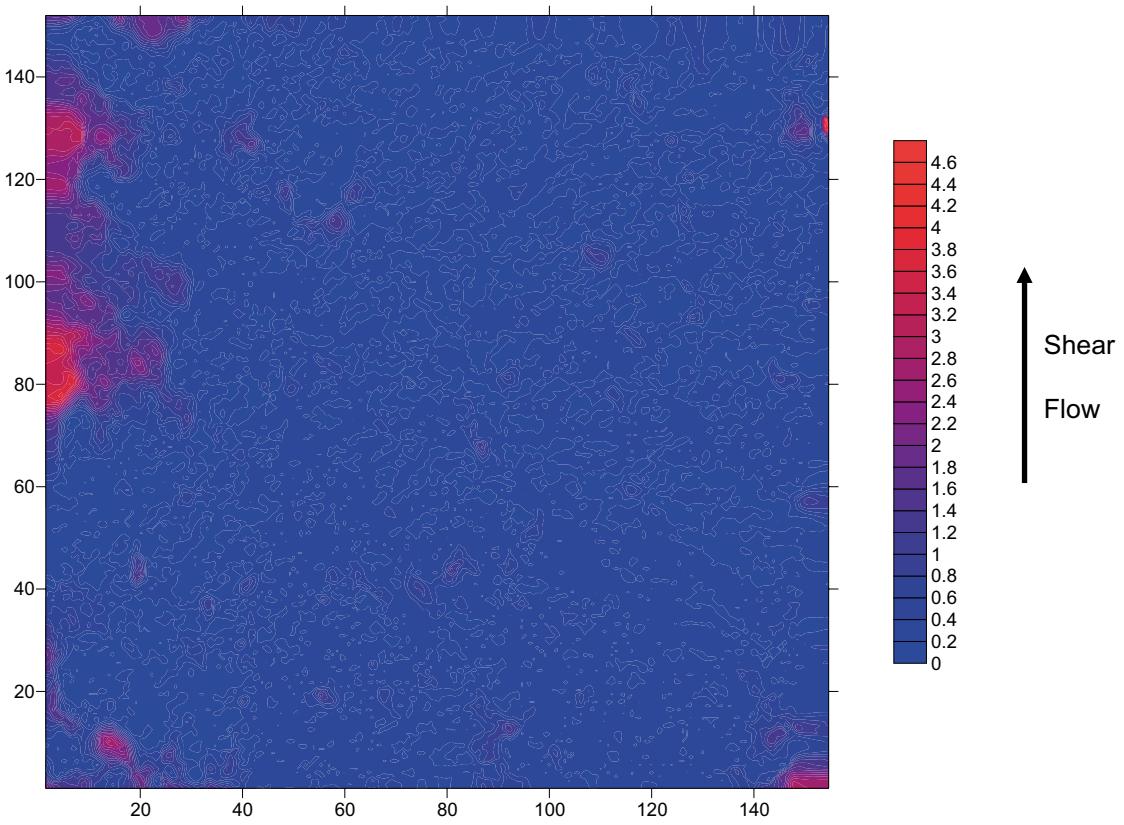

a) before the test

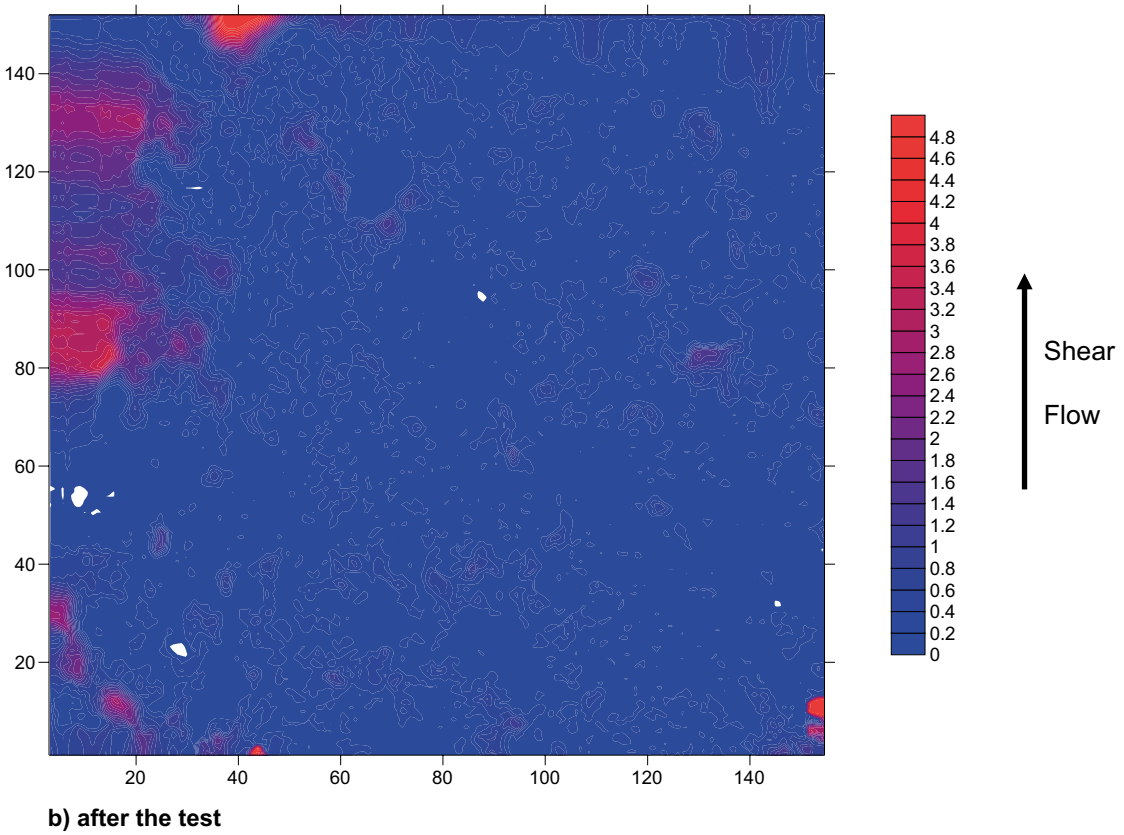

b) after the test

Figure 3-7. *Aperture contours in mm for Sample 3 (whole aperture range).*

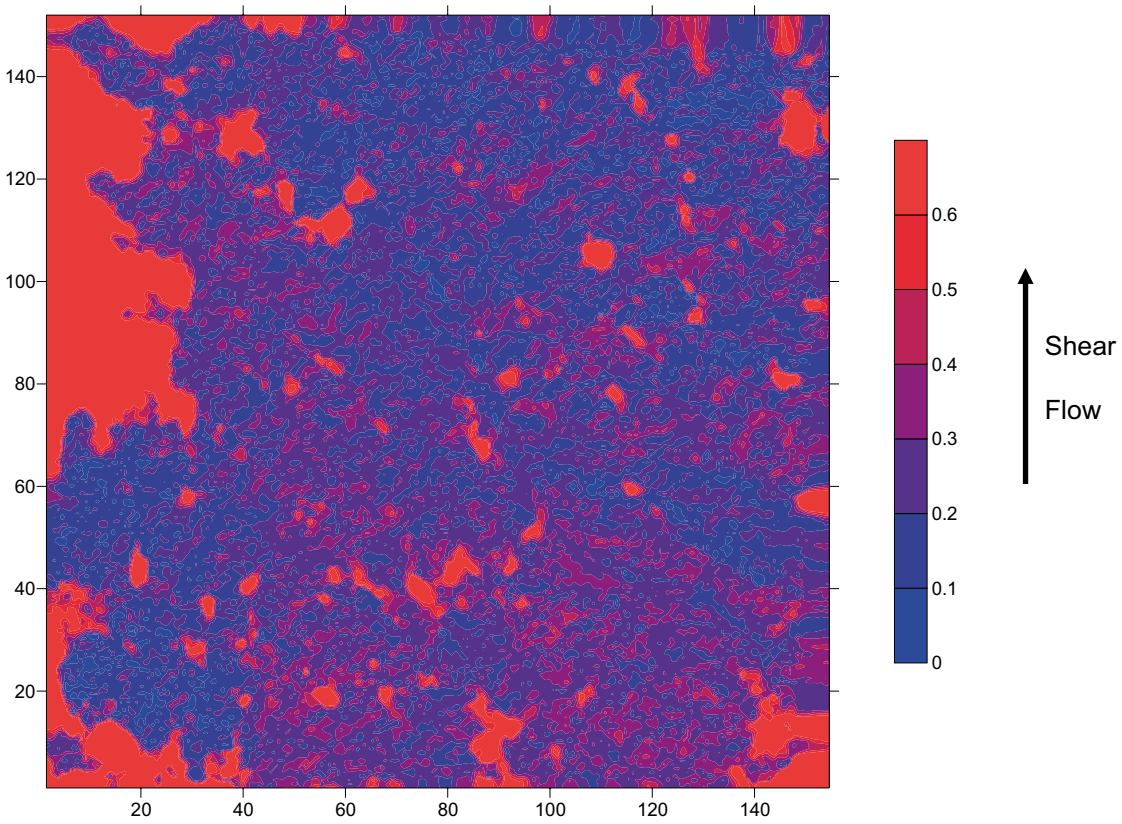

a) before the test

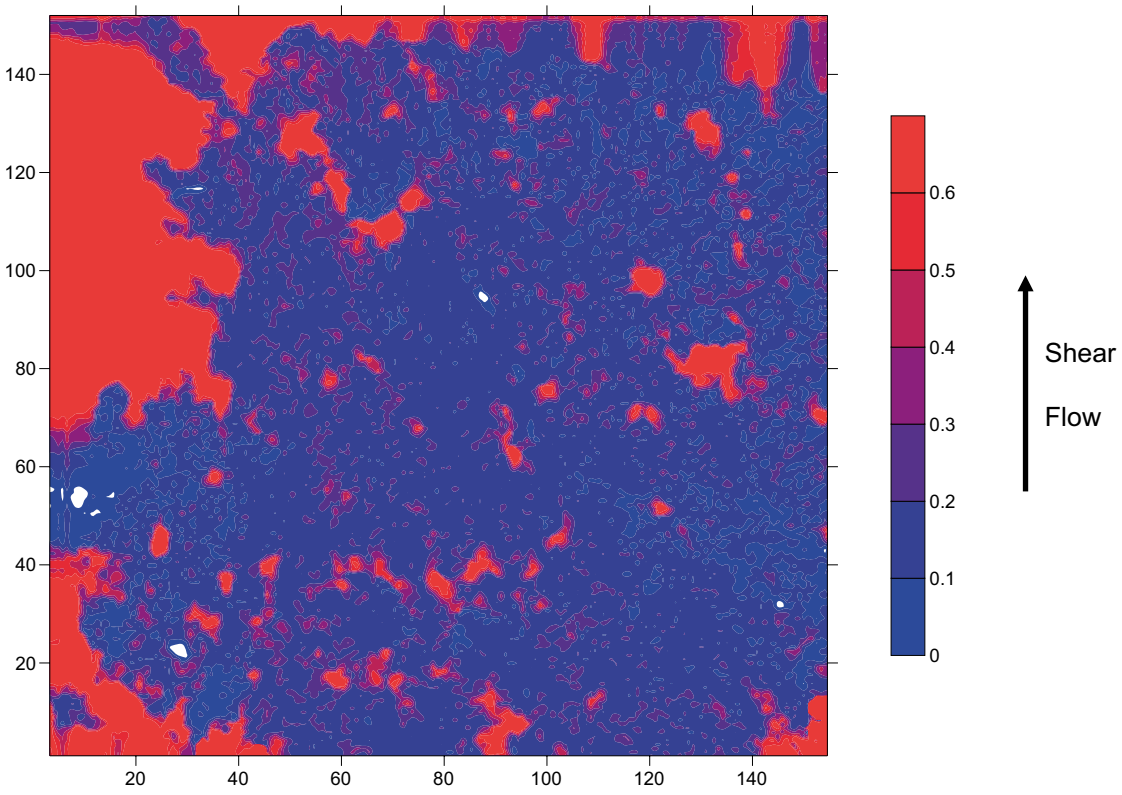

b) after the test

Figure 3-8. *Aperture contours in mm for Sample 3 (medium aperture range).*

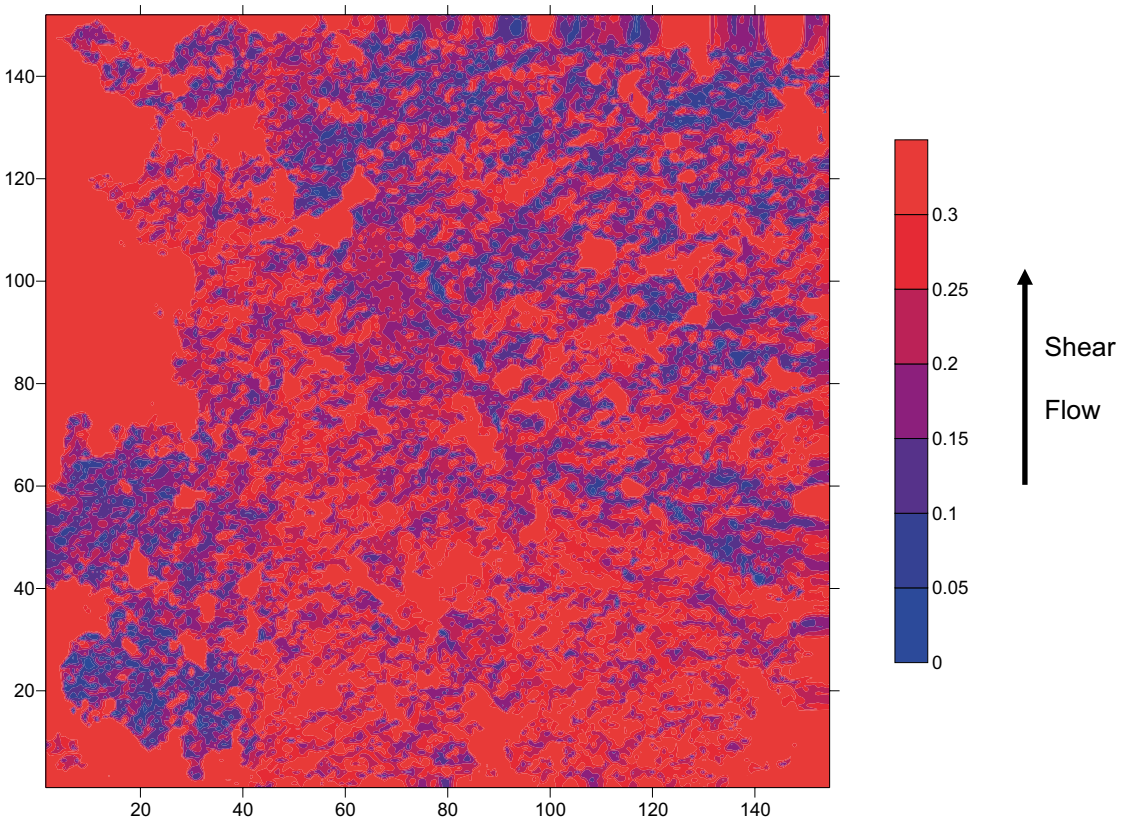

a) before the test

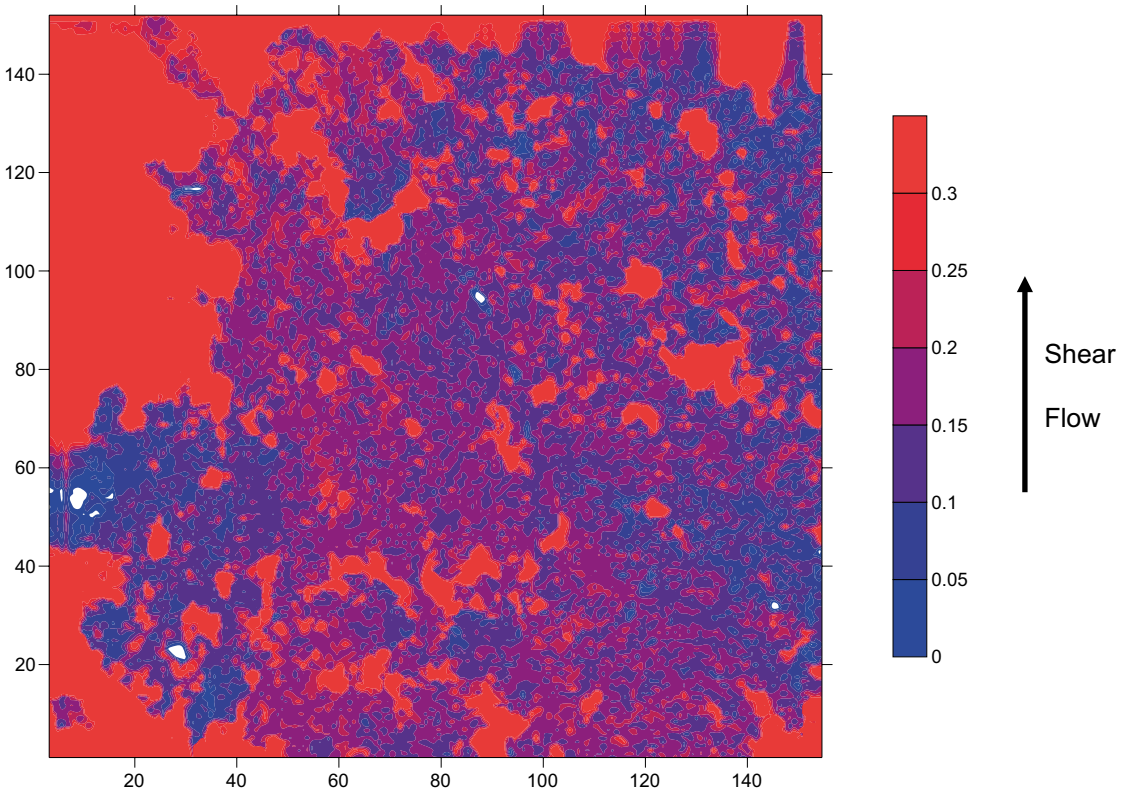

b) after the test

Figure 3-9. *Aperture contours in mm for Sample 3 (small aperture range).*

3.2 Exploratory aperture data analysis

To better understand the nature of the three fracture samples, an exploratory data analysis was performed with the fracture mechanical aperture data. An area of 12 cm × 12 cm in the centre of each sample was selected for this analysis in order to avoid any effect that could be caused by the broken pieces in the boundaries of the samples after the stress-flow tests were performed.

The first part of the data exploration included the derivation of basic statistical parameters from the fracture mechanical aperture data of each sample in the same area (12 cm × 12 cm centred). Table 3-1, Table 3-2 and Table 3-3 present these results.

Table 3-1. Fracture mechanical aperture statistics of the three samples before and after the stress-flow test based on a normal distribution function (12 cm × 12 cm).

	Sample 1		Sample 2		Sample 3	
	Before test	After test	Before test	After test	Before test	After test
Mean	0.51957	0.50599	0.3426	0.28285	0.26661	0.23246
75%tile	0.5826	0.55767	0.31075	0.22346	0.29556	0.21032
Maximum	3.47179	4.9499	3.8445	3.77548	2.32596	2.52304
Standard Deviation	0.38822	0.40559	0.42288	0.43651	0.18347	0.25165
Variance	0.15071	0.1645	0.17883	0.19054	0.03366	0.06333
Coef. Skewness	2.76233	2.5626	4.17121	4.0786	3.84393	3.84193
Coef. Variation	0.7472	0.80157	1.23431	1.54323	0.68816	1.08253

Table 3-2. Fracture mechanical aperture statistics of the three samples before the stress-flow test based on a normal distribution function (12 cm × 12 cm).

	Mean	75%tile	Max	Standard Deviation	Variance	Coef. Skew.	Coef. Variat.
Sample 1	0.51957	0.5826	3.47179	0.38822	0.15071	2.76233	0.7472
Sample 2	0.3426	0.31075	3.8445	0.42288	0.17883	4.17121	1.23431
Sample 3	0.26661	0.29556	2.32596	0.18347	0.03366	3.84393	0.68816

Table 3-3. Fracture mechanical aperture statistics of the three samples after the stress-flow test based on a normal distribution function (12 cm × 12 cm).

	Mean	75%tile	Max	Standard Deviation	Variance	Coef. Skew.	Coef. Variat.
Sample 1	0.50599	0.55767	4.9499	0.40559	0.1645	2.5626	0.80157
Sample 2	0.28285	0.22346	3.77548	0.43651	0.19054	4.0786	1.54323
Sample 3	0.23246	0.21032	2.52304	0.25165	0.06333	3.84193	1.08253

Following the statistical parameter derivation, frequency histograms and cumulative probability diagrams were derived from the data in order to facilitate its comparison (Figure 3-10 to Figure 3-15).

Finally, experimental directional and omnidirectional variograms of the fracture mechanical aperture were derived for the three samples before and after the stress-flow test (Figure 3-16, Figure 3-17 and Figure 3-18). The directional variograms were calculated with an angular tolerance of 22.5°.

The statistical data in Table 3-1, Table 3-2 and Table 3-3 and the histograms and cumulative probability plots (Figure 3-10 to Figure 3-15) support the observations made in our preliminary visual comparison of the three samples presented in the previous section. The mechanical aperture of Sample 1 is the least affected by the stress-flow tests whereas the mechanical aperture of Sample 2 is the most affected by the coupled tests. The experimental variograms in Figure 3-16, Figure 3-17 and Figure 3-18 agree well with this fact also.

Looking at the experimental variograms of the mechanical aperture of Sample 1 we see a low anisotropy both before and after the test (Figure 3-16). The correlation distance increases after the test and this indicates that the mechanical aperture is more correlated after the test than before the test.

Sample 2 has a much more pronounced anisotropy even at low lag distance (Figure 3-17), and it is even higher after the test. The correlation distance of the mechanical aperture of Sample 2 increases after the test.

Sample 3 (Figure 3-18) shows neglectable anisotropy at small lag distances (less than 6 mm). The anisotropy grows with the lag distance and this effect is much more noticeable after the test. In this case there is not much difference between the correlation distance before and after the test.

For all three samples the sill increases significantly after the test has been performed.

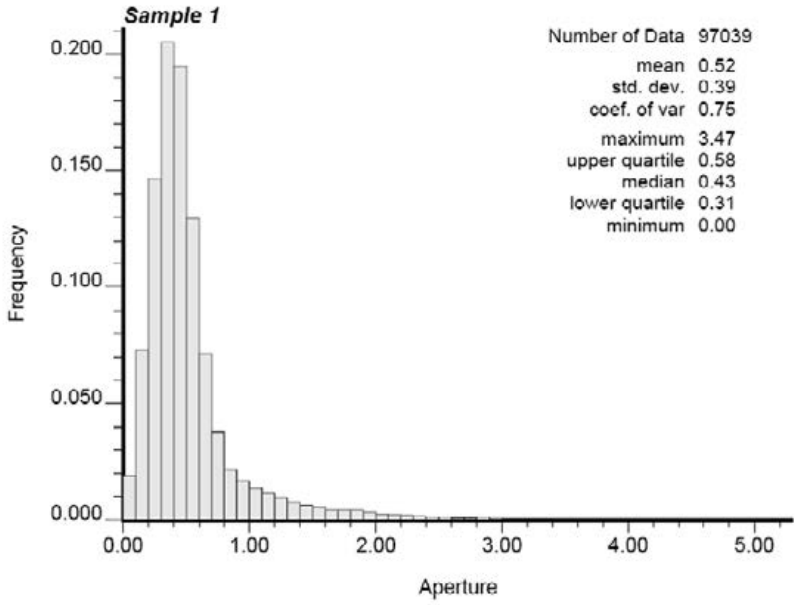

a) before the test

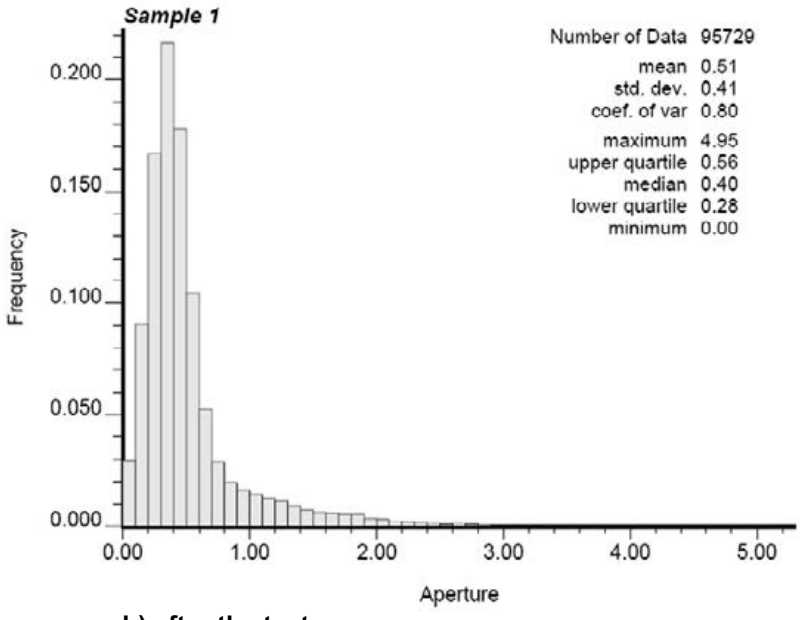

b) after the test

Figure 3-10. *Histogram of the fracture mechanical aperture values of Sample 1 (12 cm × 12 cm, centred) before and after the test based on the 3D-laser scanning data (Aperture is in mm).*

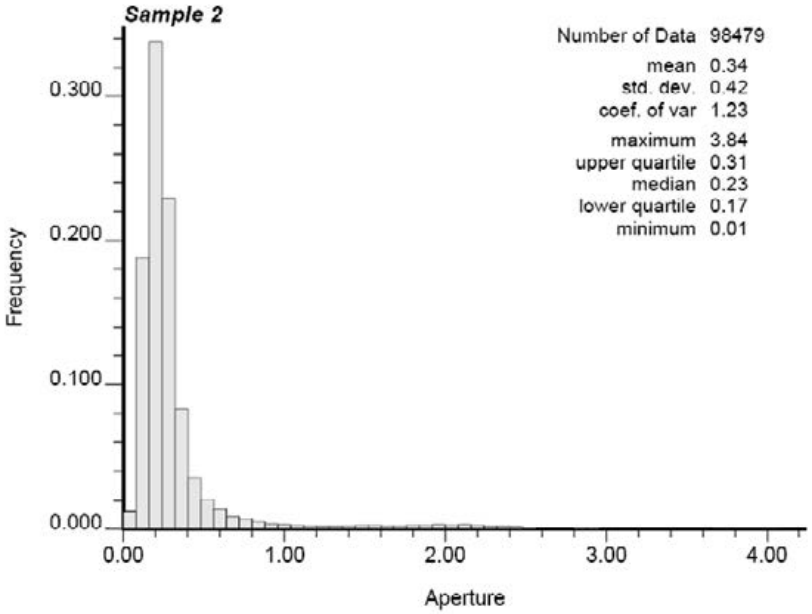

a) before the test

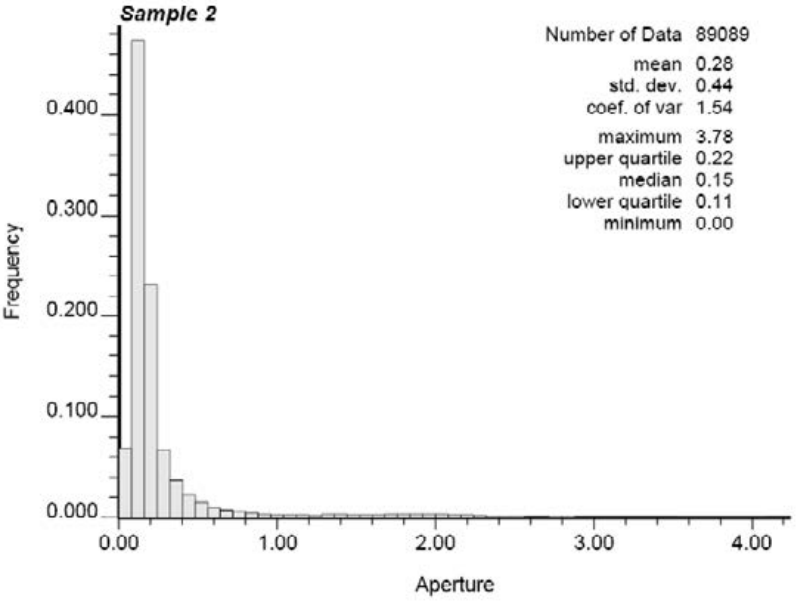

b) after the test

Figure 3-11. *Histogram of the fracture mechanical aperture values of Sample 2 (12 cm × 12 cm, centred) before and after the test based on the 3D-laser scanning data (Aperture is in mm).*

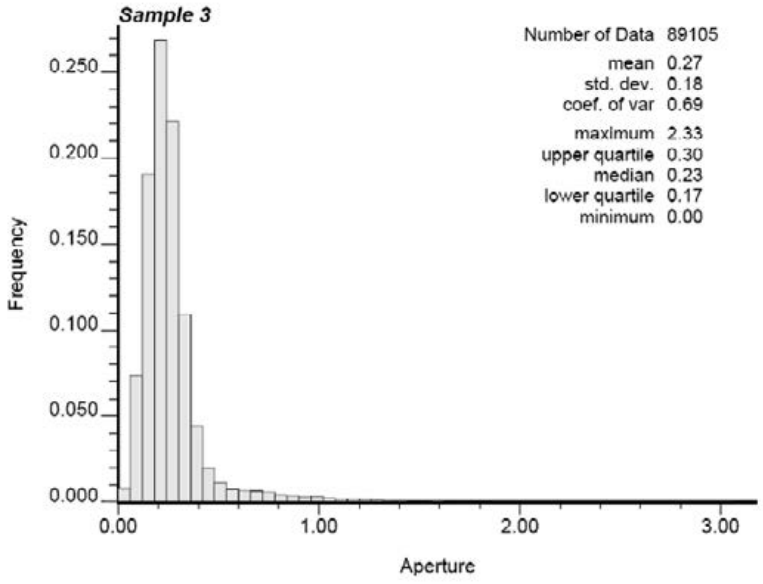

a) before the test

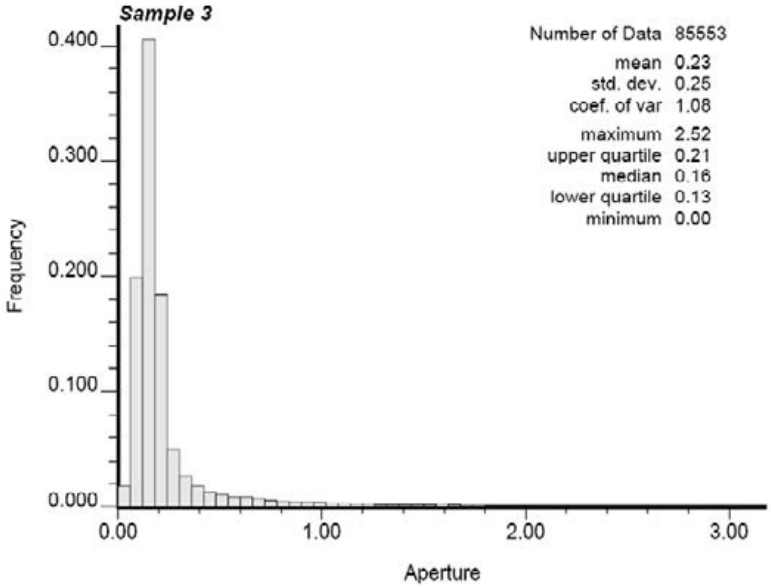

b) after the test

Figure 3-12. *Histogram of the fracture mechanical aperture values of Sample 3 (12 cm × 12 cm, centred) before and after the test based on the 3D-laser scanning data (Aperture is in mm).*

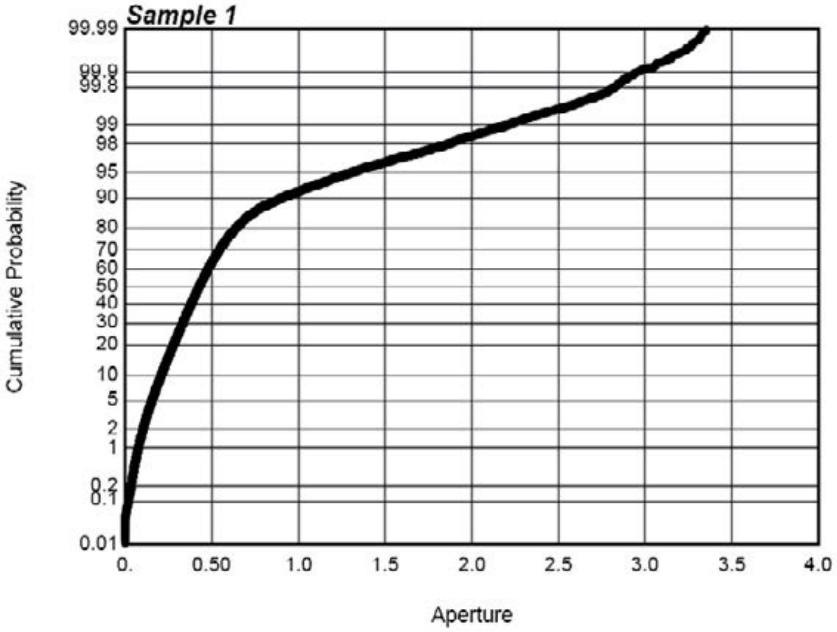

a) before the test

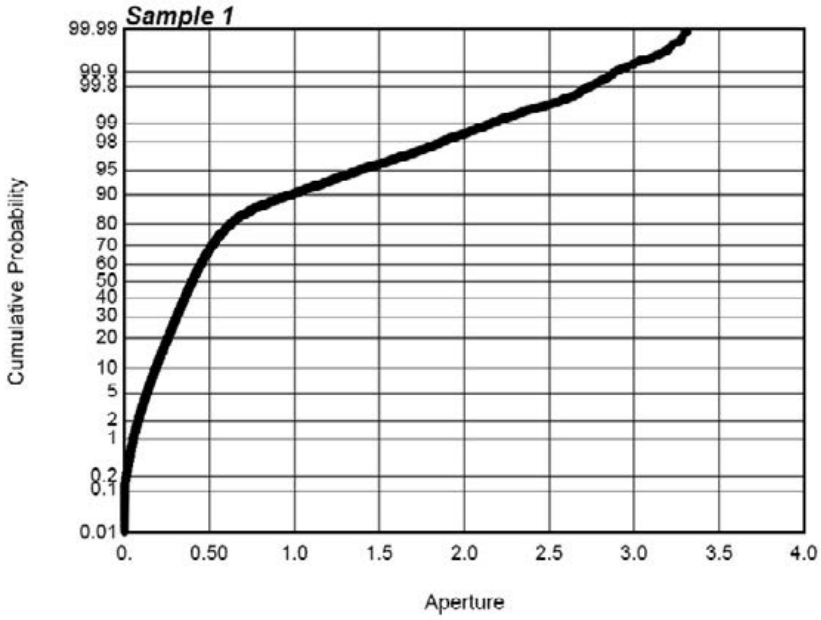

b) after the test

Figure 3-13. *Cumulative probability distribution of the fracture mechanical aperture values of Sample 1 (12 cm × 12 cm, centred) before and after the test based on the 3D-laser scanning data (Aperture is in mm).*

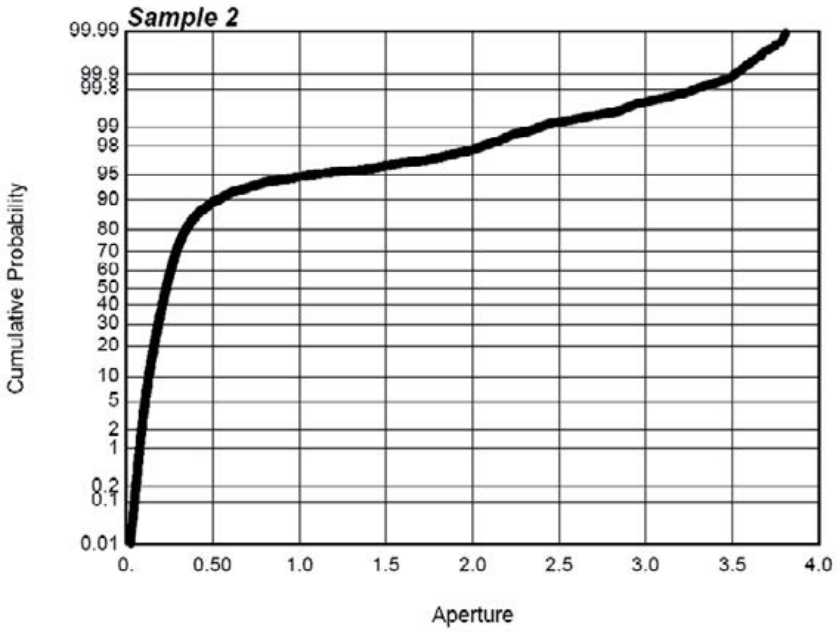

a) before the test

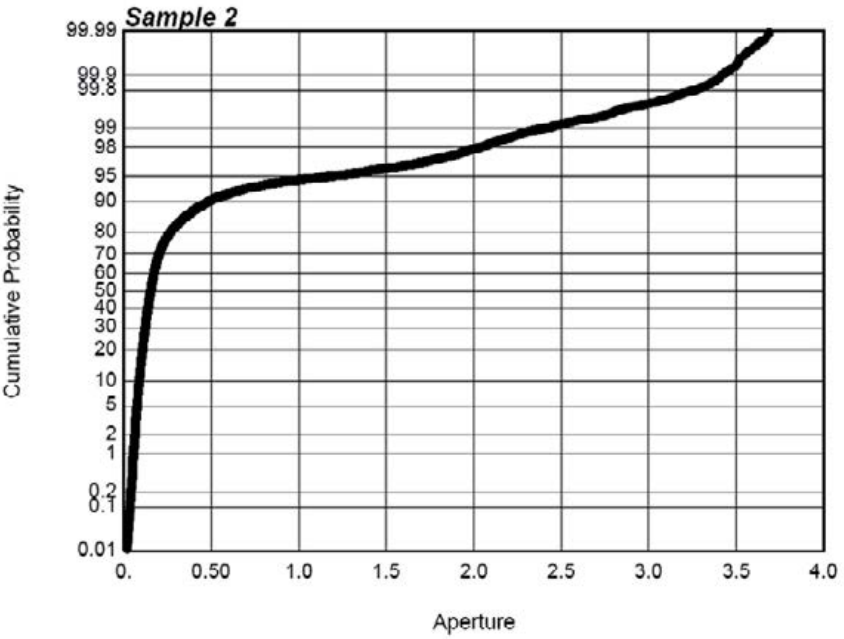

b) after the test

Figure 3-14. *Cumulative probability distribution of the fracture mechanical aperture values of Sample 2 (12 cm × 12 cm, centred) before and after the test based on the 3D-laser scanning data (Aperture is in mm).*

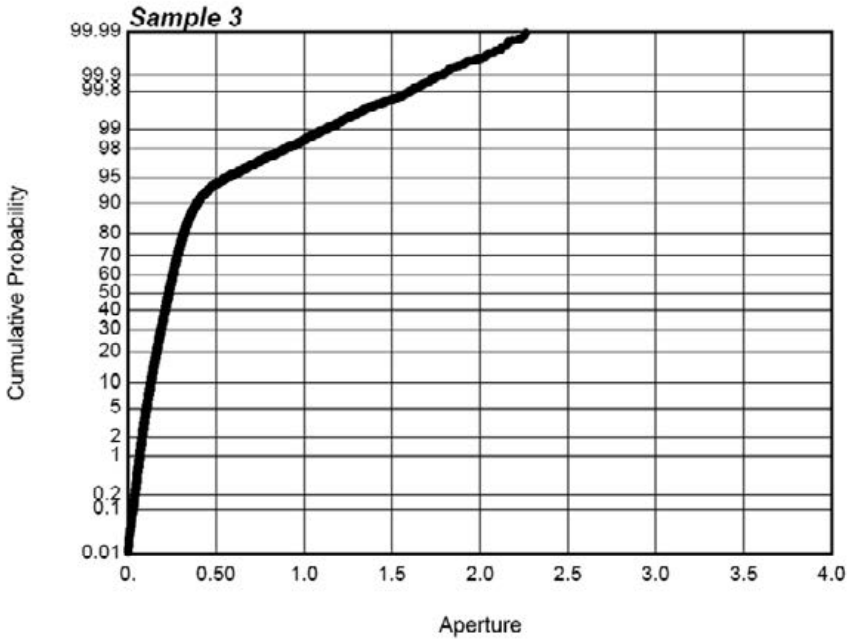

a) before the test

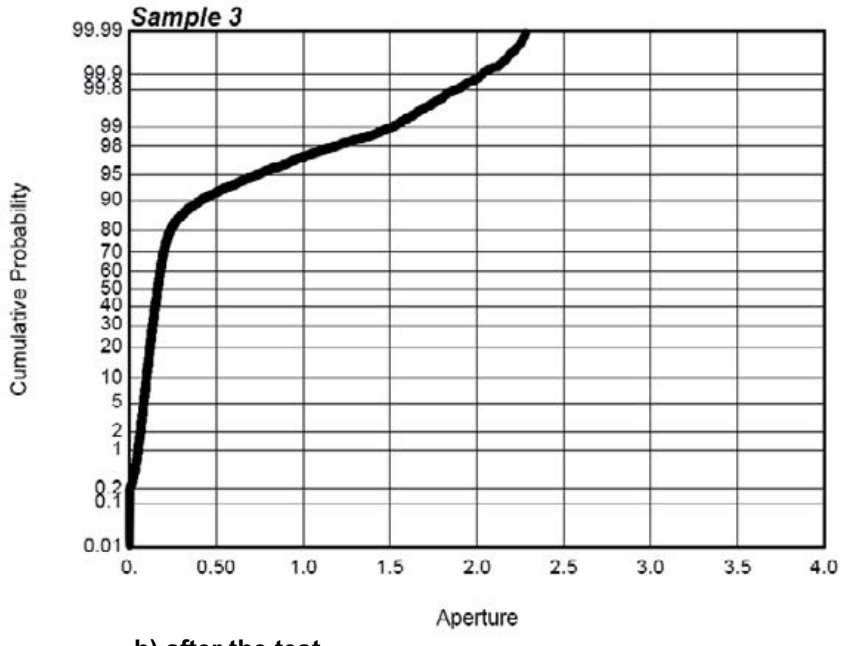

b) after the test

Figure 3-15. *Cumulative probability distribution of the fracture mechanical aperture values of Sample 3 (12 cm × 12 cm, centred) before and after the test based on the 3D-laser scanning data (Aperture is in mm).*

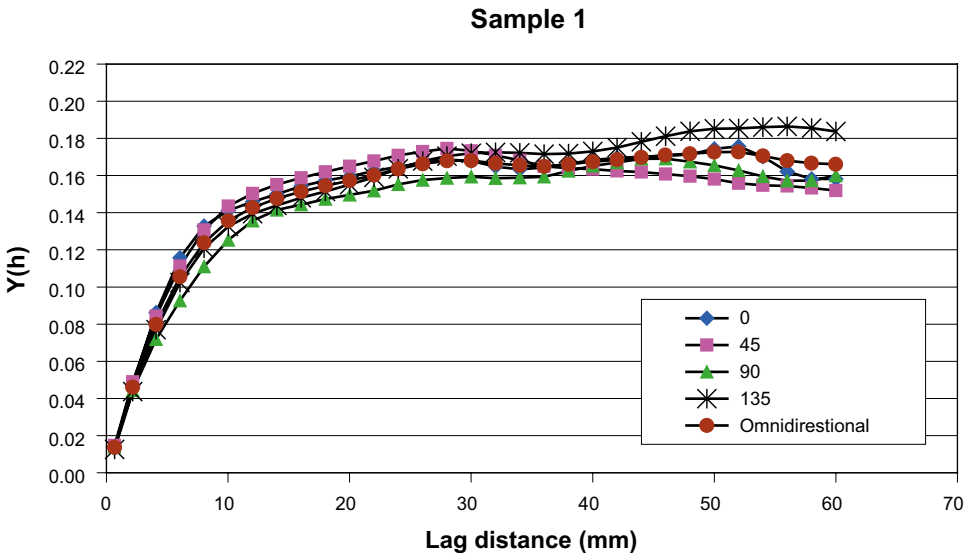

a) before the test

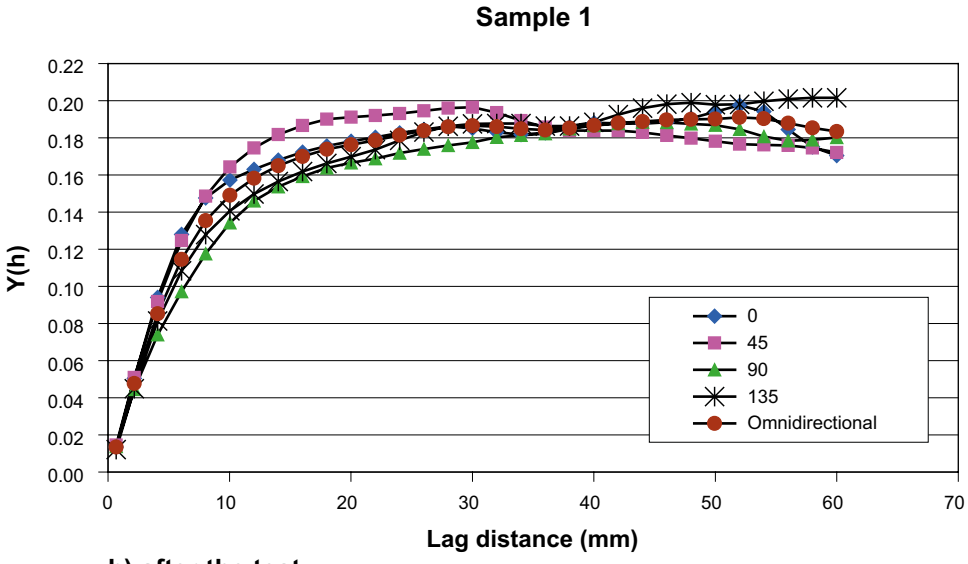

b) after the test

Figure 3-16. *Directional and omnidirectional experimental variograms of the fracture mechanical aperture of Sample 1 (12 cm × 12 cm, centred). 0° indicates the positive y-direction (bottom to top of the page) referred to the mechanical aperture contour plots in Section 3.1.*

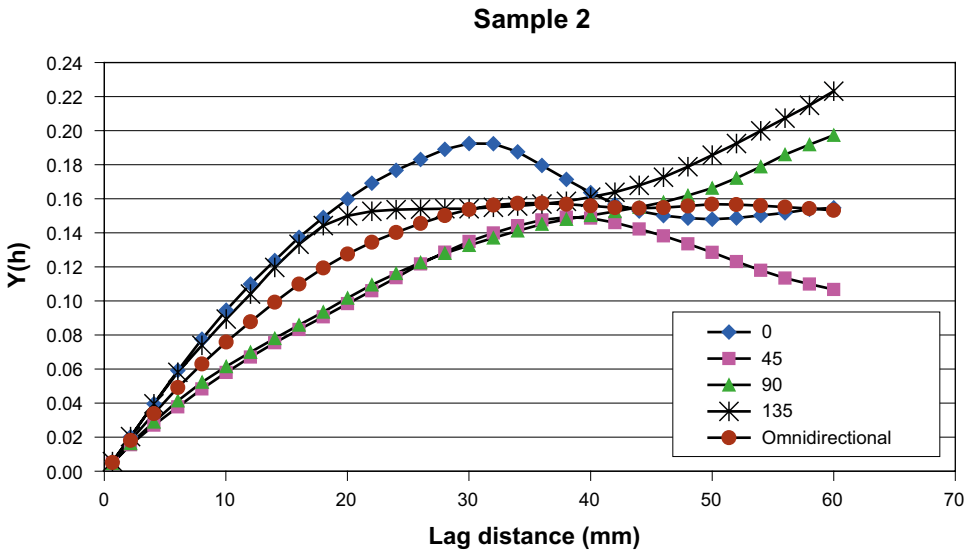

a) before the test

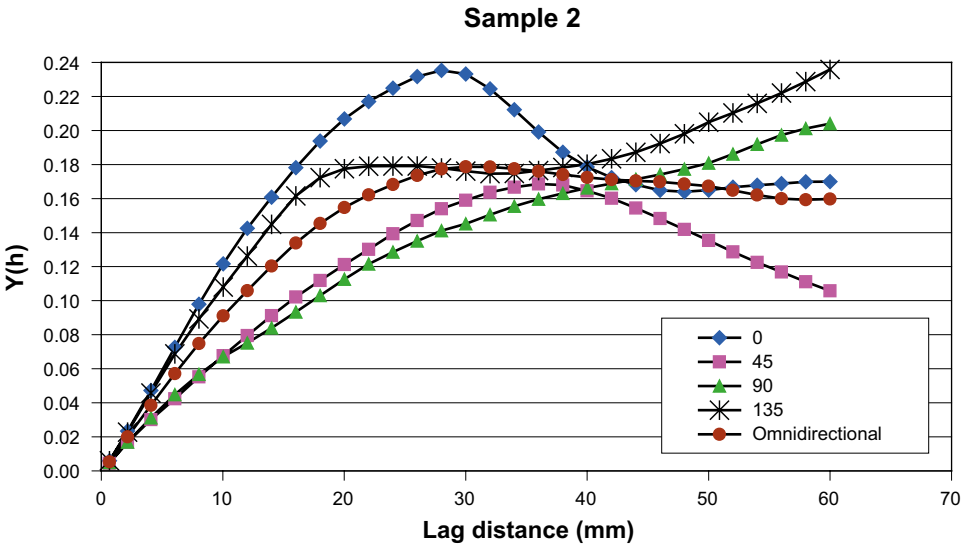

b) after the test

Figure 3-17. *Directional and omnidirectional experimental variograms of the fracture mechanical aperture of Sample 2 (12 cm × 12 cm, centred). 0° indicates the positive y-direction (bottom to top of the page) referred to the mechanical aperture contour plots in Section 3.1.*

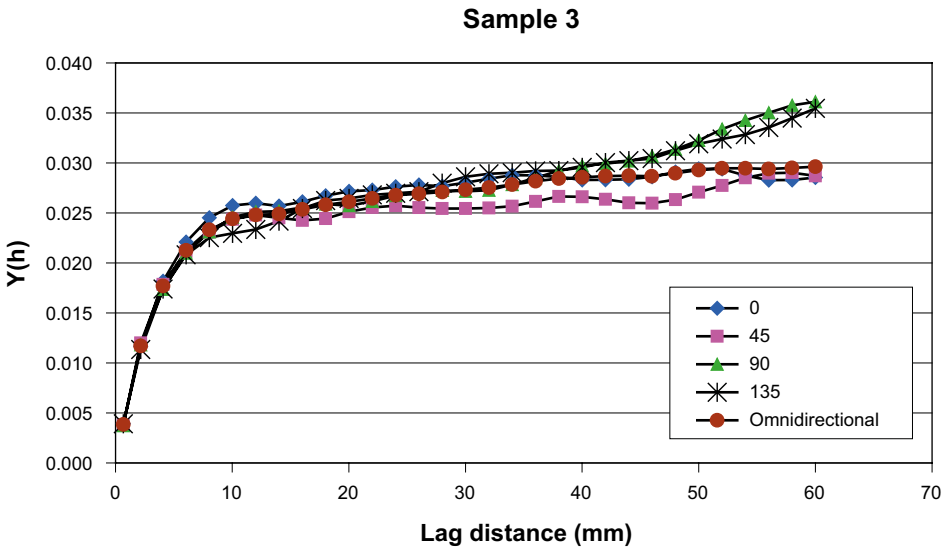

a) before the test

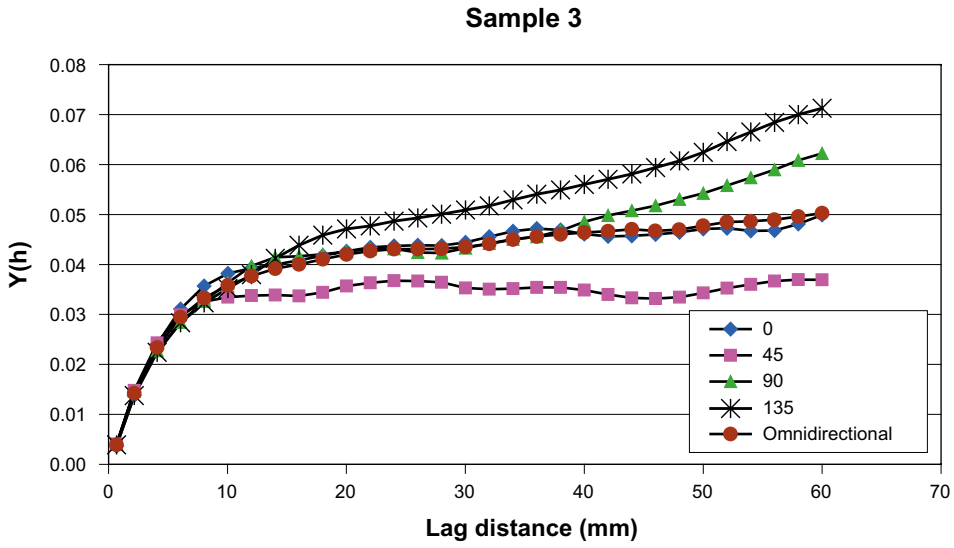

b) after the test

Figure 3-18. *Directional and omnidirectional experimental variograms of the fracture mechanical aperture of Sample 3 (12 cm × 12 cm, centred). 0° indicates the positive y-direction (bottom to top of the page) referred to the mechanical aperture contour plots in Section 3.1.*

3.3 Results from the coupled normal load-flow test

This section contains the results from the coupled normal load-flow tests.

3.3.1 Vertical displacement

As explained in the previous Section 2.1.2 concerning the test plan, four cycles of normal loading/unloading were performed with each of the fracture samples in order to get information about their coupled normal stress-flow behaviour. Additionally, it was assumed that after the fourth loading/unloading cycle, the fracture would be in a state of closure and matedness as similar as possible to in-situ conditions.

The following figures (Figure 3-19 to Figure 3-21) present the measured vertical displacement while performing the four normal loading/unloading cycles of the normal stress-flow tests. As described in Section 2.1.1 regarding the shearing unit, there is a central transducer over the normal force actuator which records the vertical displacement. In the figures (Figure 3-19 to Figure 3-21) these data is labelled "central transducer". The data with the labels LVDT 1, LVDT 2, LVDT 3 and LVDT4, belongs to the four lateral transducers attached to the concrete cast.

It is important to point out that the central transducer data includes both the elastic response of all the concrete cast and the intact rock as well as the fracture response to the normal load change. On the other hand, the normal displacement data coming from the four lateral LVDTs includes a very small portion of the intact rock and a neglectable portion of the concrete cast. For this reason, the normal fracture displacement for the rest of the analysis was derived from the average value of the four lateral LVDTs.

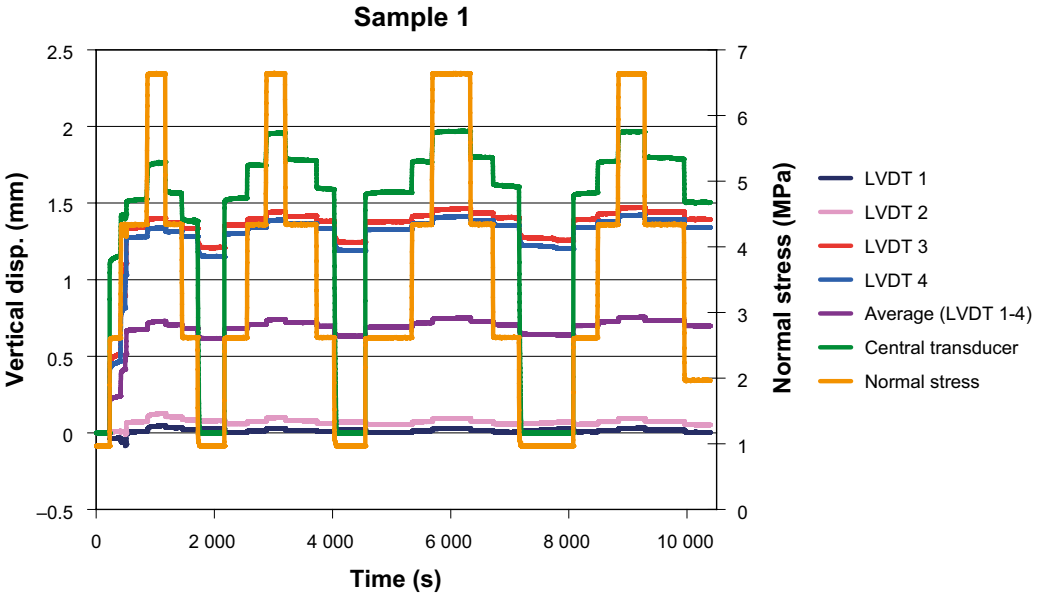

Figure 3-19. *Vertical displacement measured during the four loading/unloading cycles of the coupled normal stress-flow test for Sample 1.*

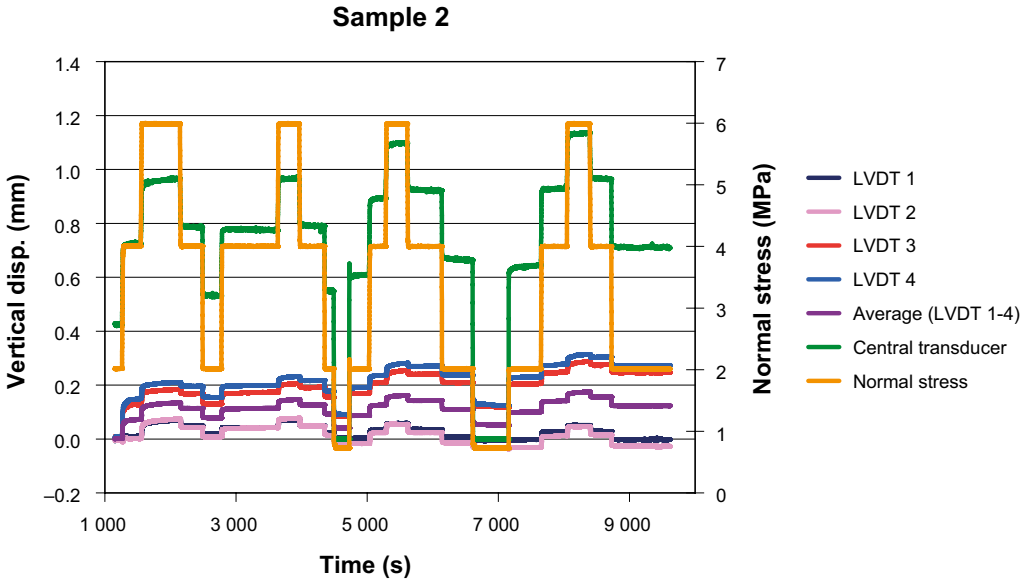

Figure 3-20. *Vertical displacement measured during the four loading/unloading cycles of the coupled normal stress-flow test for Sample 2.*

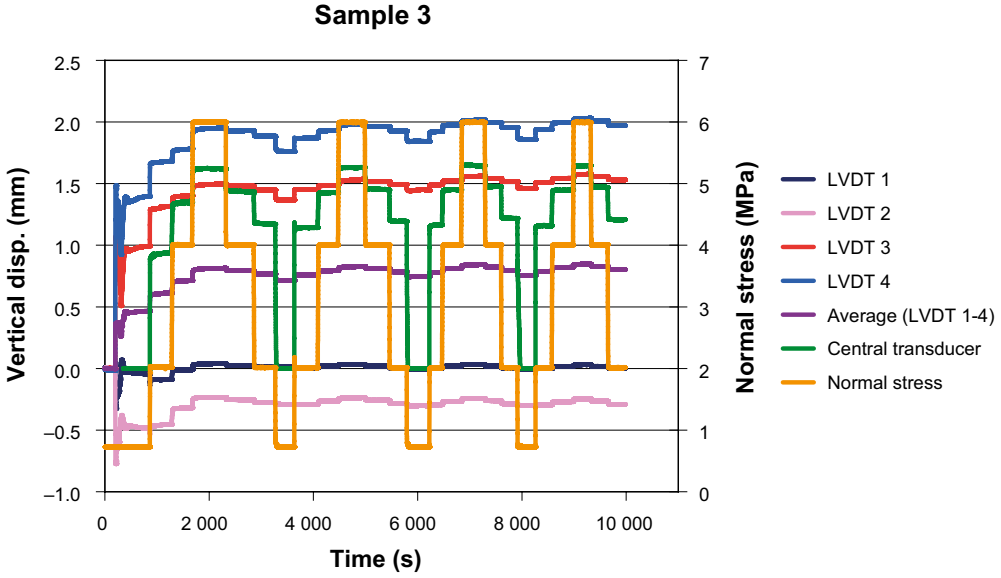

Figure 3-21. *Vertical displacement measured during the four loading/unloading cycles of the coupled normal stress-flow test for Sample 3.*

3.3.2 Normal stress vs. vertical displacement

Figure 3-22 , Figure 3-23 and Figure 3-24 present the normal stress vs. vertical displacement data for the three samples during the four loading/unloading cycles of the coupled normal stress-flow tests. As already mentioned the vertical displacement is the average from the four lateral LVDTs. During the Sample 1 loading/unloading tests (Figure 3-22), the normal load was not correctly calculated and the normal stress reached values larger than the planned intervals of 2 MPa, 4 MPa and 6 MPa. However, this has no negative effect in the validity of the data collected and its analysis. Also, notice that the downloading in the first cycle in Sample 2 stopped at 2 MPa instead of reaching the minimum value of 0.73 MPa (the minimum normal stress for Sample 1 was 0.97 MPa due to its smaller area as explained in the test plan Section 2.1.2).

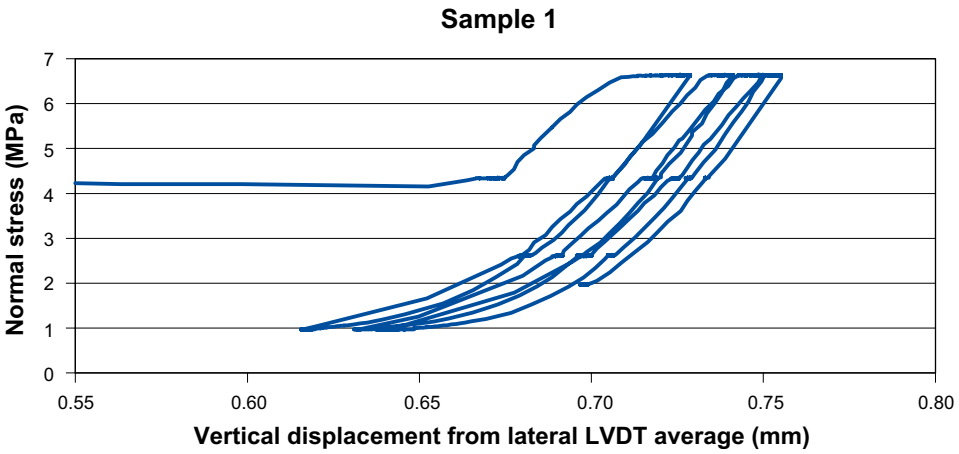

Figure 3-22. *Normal stress vs. vertical displacement during the four loading/unloading cycles of the coupled normal stress-flow tests for Sample 1.*

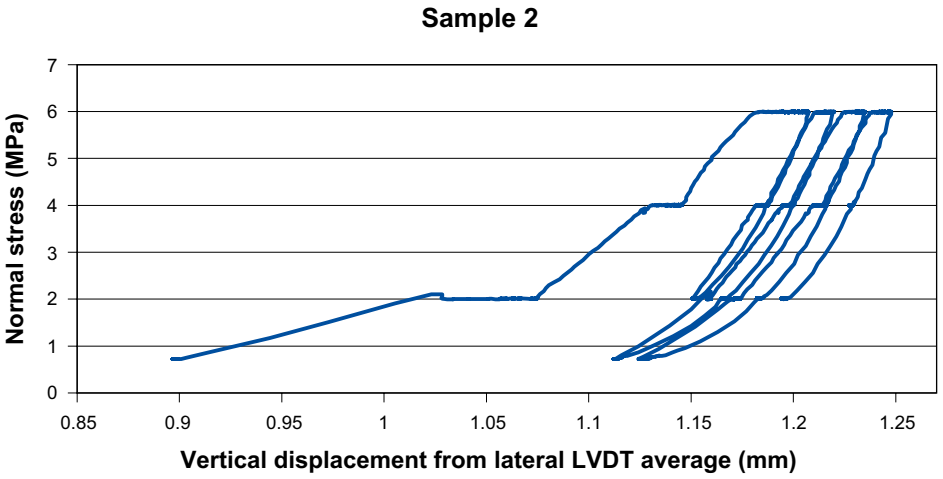

Figure 3-23. *Normal stress vs. vertical displacement during the four loading/unloading cycles of the coupled normal stress-flow tests for Sample 2.*

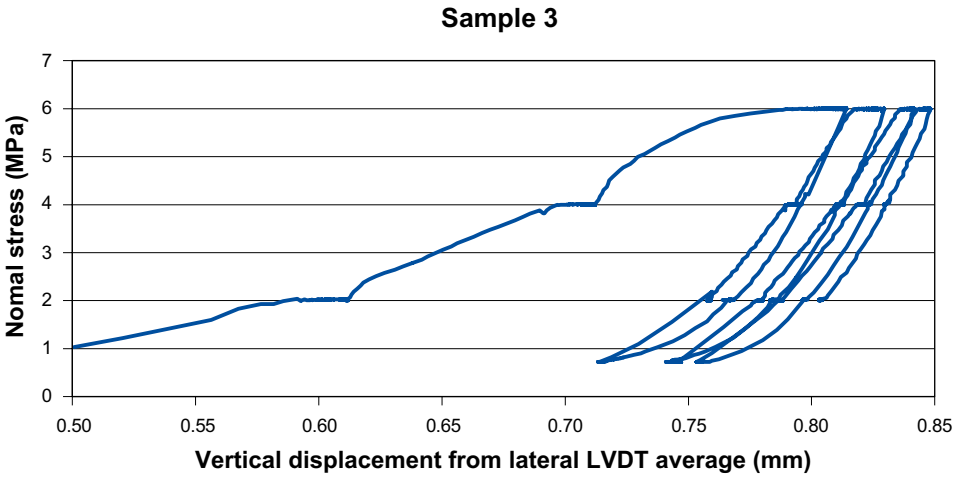

Figure 3-24. *Normal stress vs. vertical displacement during the four loading/unloading cycles of the coupled normal stress-flow tests for Sample 3.*

3.3.3 Fracture normal stiffness

For the derivation of the fracture normal stiffness of the samples tested, the third uploading cycle was considered. Figure 3-25 shows an example of the main components needed for this derivation which followed the methodology from Esaki et al. (2001).

The procedure for the derivation of the normal stiffness of the three fracture samples tested was the following. Based on the data on normal stress vs. vertical displacement (which includes the fracture, the intact rock and the cast responses) from the 3rd cycle uploading, a curve was fitted and prolonged until it reached a normal stress of 16 MPa (after which it is assumed that the fractures are as mechanically closed as they can be). This curve represents the normal stress-vertical displacement behaviour of the fracture, the intact rock and the cast. The part belonging to the displacement in the intact rock part and the cast was then subtracted, after which the curve belonging to the fracture behaviour was obtained. Figure 3-26, Figure 3-27 and Figure 3-28 present this procedure for the three fracture samples. From these data, the fracture normal stiffness of the three samples was derived following the methodology described in Lanaro et al. (2006). Table 3-4 presents the normal stiffness derived for the three fracture samples. Considering the normal stiffness span reported in the literature (e.g. SKB 2008, 2009), the normal stiffness values for the three samples are remarkably similar. This is probably explained by the fact that the samples are from the same fracture and also that they have similar size.

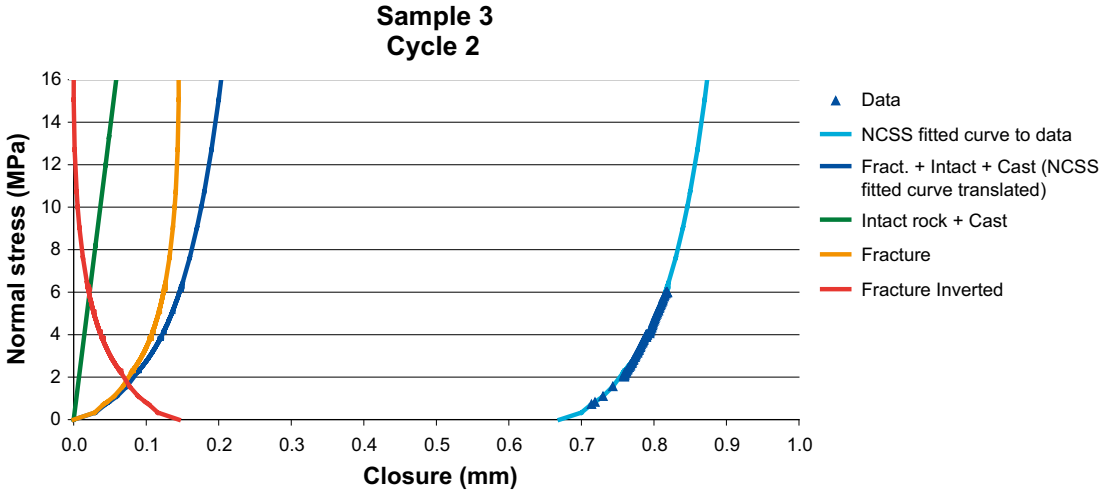

Figure 3-25. *Scheme of the methodology for derivation of the fracture normal stress vs. closure for Sample 3 during the uploading (cycle 2) based on the test data.*

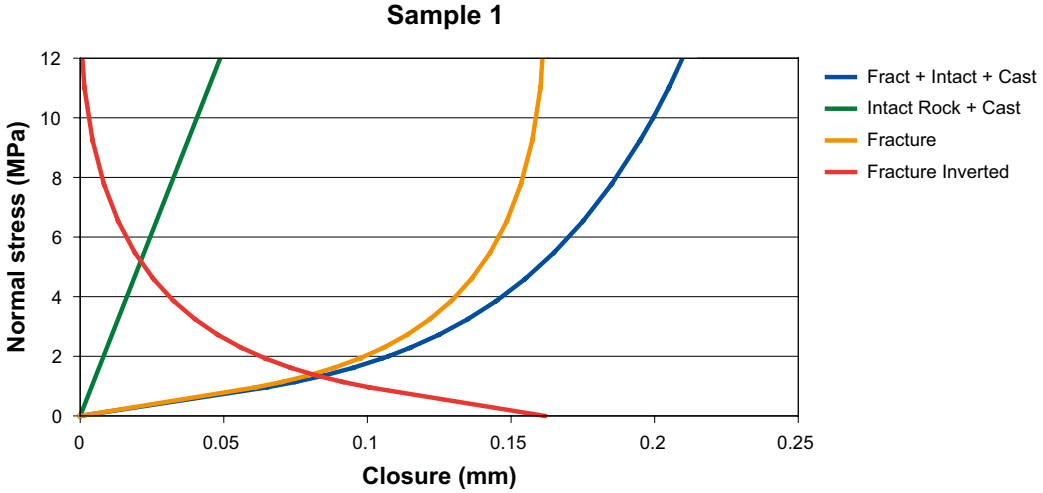

Figure 3-26. *Fracture normal stress vs. closure for Sample 1 during the uploading cycle 3.*

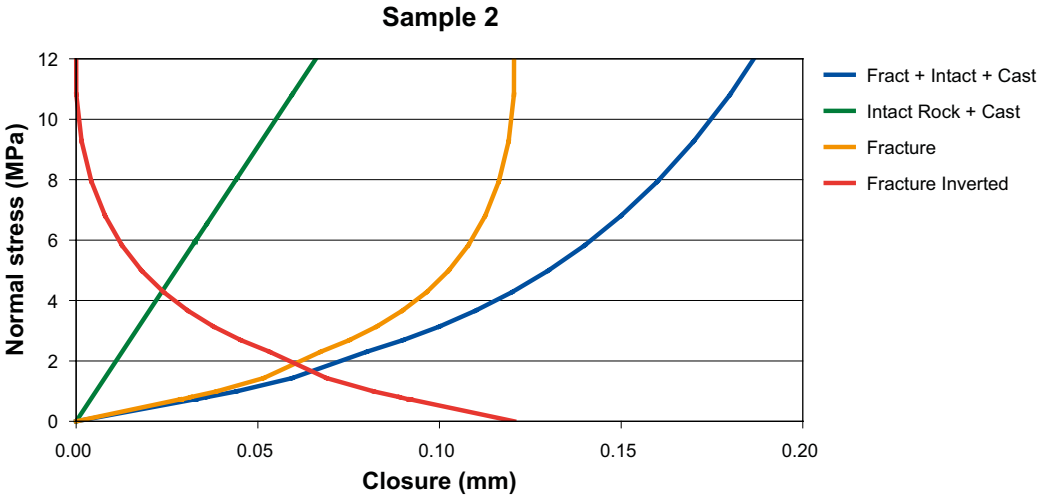

Figure 3-27. *Fracture normal stress vs. closure for Sample 2 during the uploading cycle 3.*

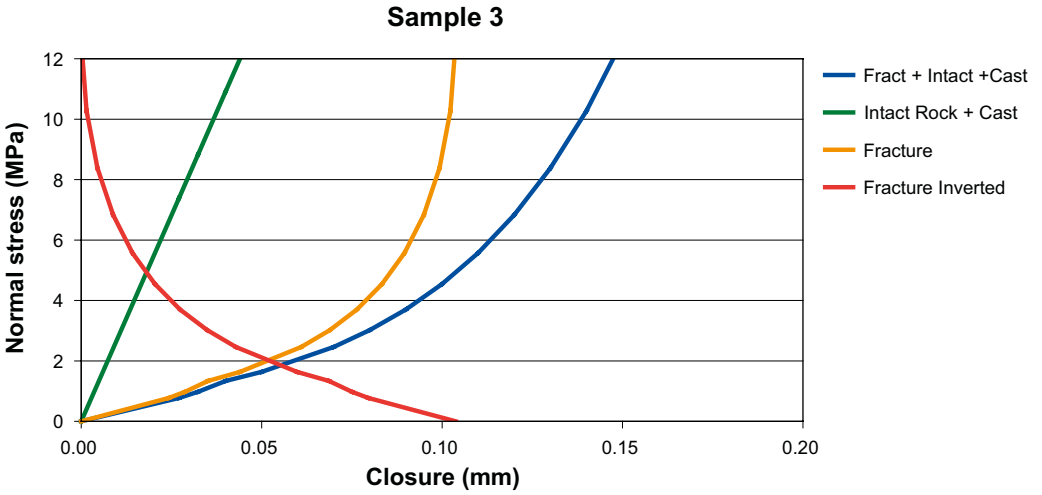

Figure 3-28. *Fracture normal stress vs. closure for Sample 3 during the uploading cycle 3.*

Table 3-4. Normal stiffness of the three fracture samples calculated following the methodology of Lanaro et al. (2006).

	Normal stiffness, Kn (MPa/mm)
Sample 1	74.8
Sample 2	87.2
Sample 3	108

3.3.4 Flow rate vs. normal stress

The following figures (Figure 3-29, Figure 3-30 and Figure 3-31) show the change in water flow during the four cycles of normal loading/unloading for the three fracture samples.

Although the initial flow for Sample 1 was very large (Figure 3-29) after the first loading it diminished in more than an order of magnitude. The last value measured was 0.053 ml/s.

Sample 2 (Figure 3-30), on the other hand, had a last flow value after the whole loading/unloading test of 2.086 ml/s.

Flow through Sample 3 (Figure 3-31) was not large from the beginning and the last value measured was 0.496 ml/s.

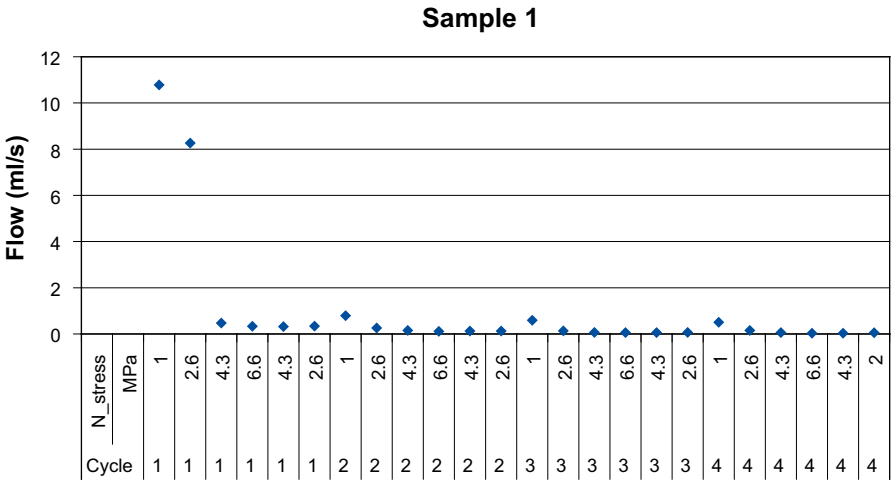

Figure 3-29. *Water flow vs. normal stress during the four loading/unloading cycles for fracture Sample 1.*

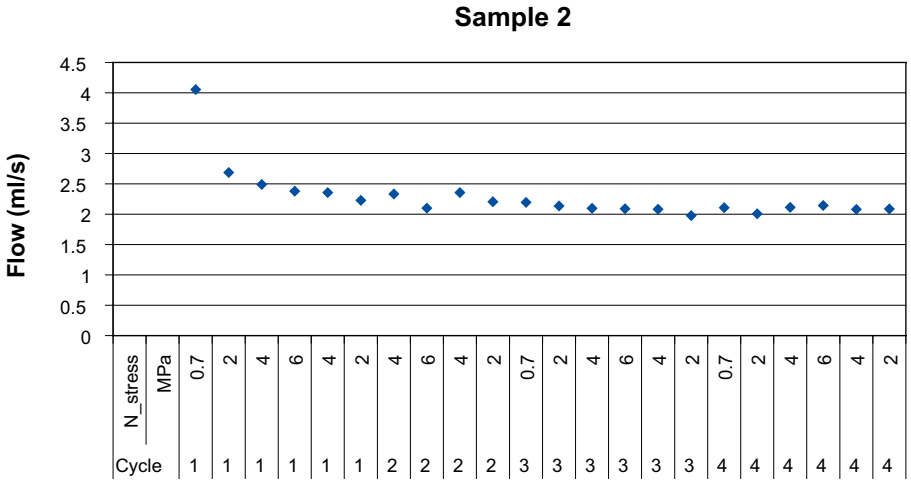

Figure 3-30. *Water flow vs. normal stress during the four loading/unloading cycles for fracture Sample 2.*

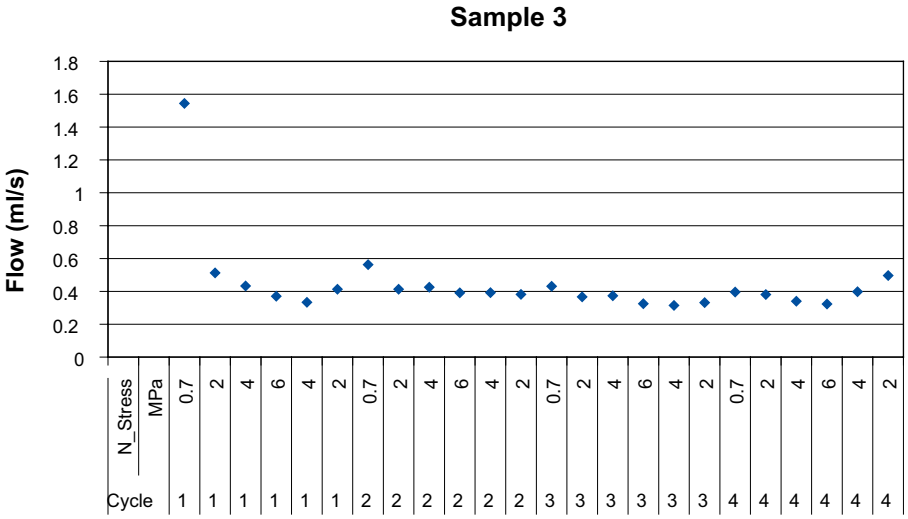

Figure 3-31. *Water flow vs. normal stress during the four loading/unloading cycles for fracture Sample 3.*

3.3.5 Reynolds number

The transition from laminar to turbulent flow is governed by the values of the Reynolds number R_e and by the relative roughness R_r (de Marsily 1986).

The Reynolds number (dimensionless) is defined, for a plane fracture, by

$$R_e = \frac{VD_h\rho}{\mu} \tag{3-1}$$

where V is the mean velocity of the fluid, μ is the coefficient of dynamic viscosity, ρ is the density of the fluid and D_h is the "hydraulic diameter" defined by

$$D_h = 4S/p \tag{3-2}$$

where S is the cross-section area of the flow in the fracture and p is the outside perimeter of this cross-section area of the flow. For a very long fracture D_h is equal to twice its aperture.

The relative roughness (dimensionless) is defined by

$$R_r = \varepsilon/D_h \tag{3-3}$$

where ε is the mean height of the irregularities in the fracture.

Depending on the values of R_e and R_r, Louis (1974) defines empirically five flow regimes and their domains of validity, which are presented in Figure 3-32.

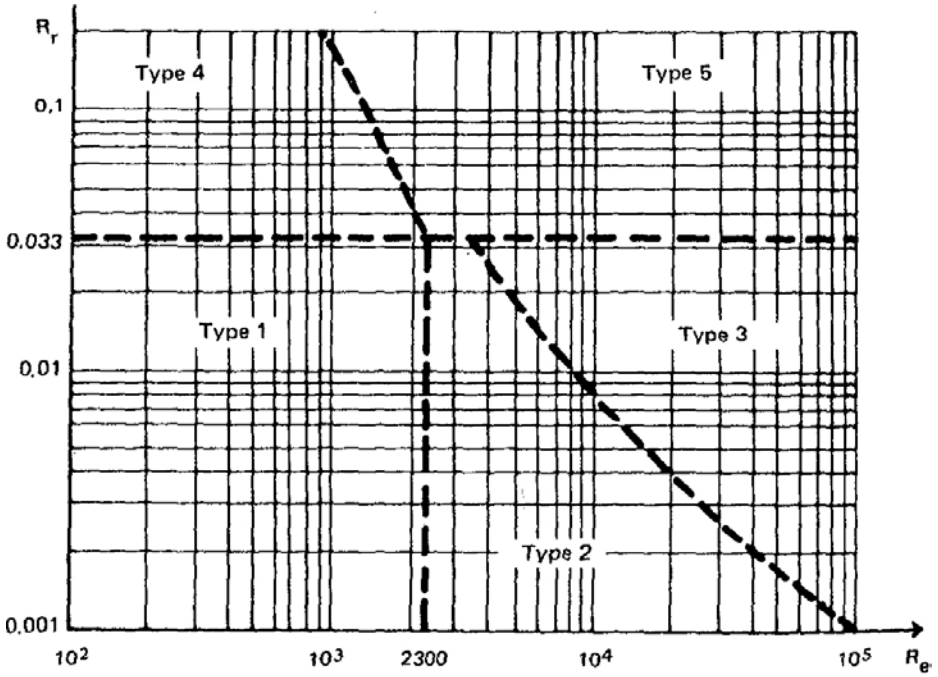

Figure 3-32. *Definition of the flow regime in a fracture (Louis 1974).*

The laws of the steady-state flow in each regime depend on the fracture aperture e, the kinematic viscosity μ/ρ, the relative roughness R_r, and the hydraulic head gradient in the fracture plane J_f:

Type 1; smooth laminar: $$V = -\left(\frac{\rho g e^2}{12\mu}\right) J_f \quad (3\text{-}4)$$

Type 2; smooth turbulent: $$V = -\left[\frac{g}{0.079}\left(\frac{2\rho e^5}{\mu}\right)^{1/4} J_r\right]^{4/7} \quad (3\text{-}5)$$

Type 3; rough turbulent: $$V = -\left(4\sqrt{eg}\,\ln\frac{3.7}{R_r}\right)\sqrt{J_r} \quad (3\text{-}6)$$

Type 4; rough laminar: $$V = -\left[\frac{\rho g e^2}{12\mu\left(1+8.8R_r^{1.5}\right)}\right] J_r \quad (3\text{-}7)$$

Type 5; very rough turbulent: $$V = -\left(4\sqrt{eg}\,\ln\frac{1.9}{R_r}\right)\sqrt{J_r} \quad (3\text{-}8)$$

To calculate the values of the Reynolds number and the approximate relative roughness of the three samples, it was assumed that the flow cross-section area is the same as the fracture area.

The approximate relative roughness for Sample 1, Sample 2 and Sample 3 are 0.023, 0.008 and 0.005 respectively.

The following figures (Figure 3-33, Figure 3-34 and Figure 3-35) show the derived Reynolds numbers during the four cycles of normal loading/unloading for the three fracture samples

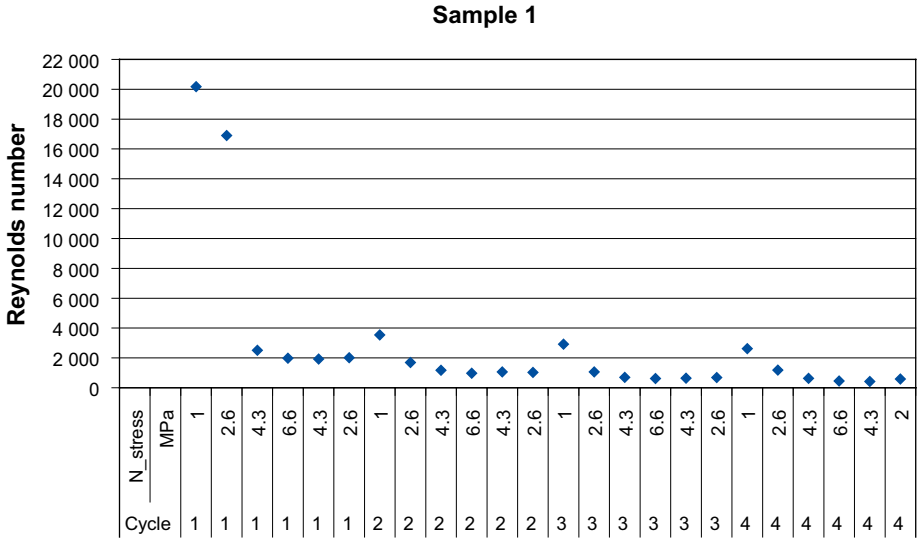

Figure 3-33. *Reynolds number vs. normal stress during the four cycles of normal loading/unloading for Sample 1.*

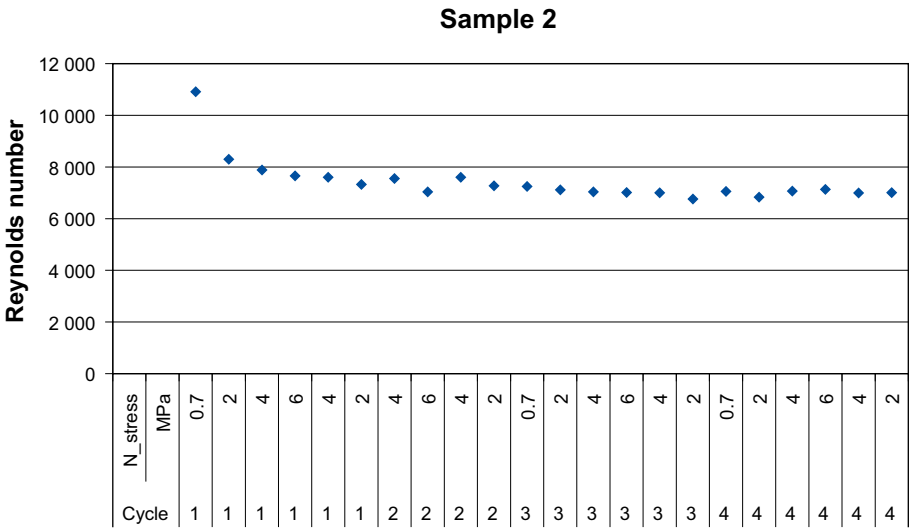

Figure 3-34. *Reynolds number vs. normal stress during the four cycles of normal loading/unloading for Sample 2.*

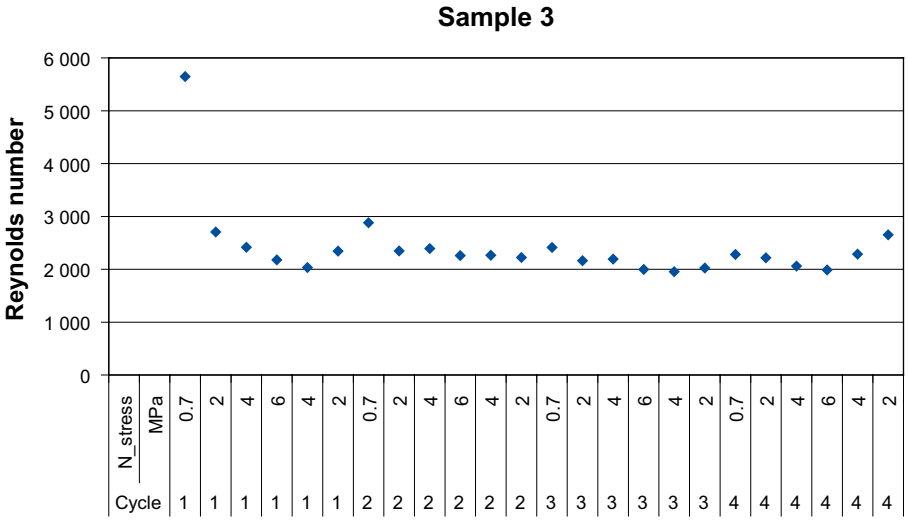

Figure 3-35. *Reynolds number vs. normal stress during the four cycles of normal loading/unloading for Sample 3.*

Sample 1 has an approximate relative roughness of 0.023, and after the first loading/unloading cycle the derived Reynolds numbers are always well under 2 300, except for very low normal stress situations (1 MPa). This makes Sample 1 have a smooth laminar to rough laminar flow regime under a usual range of normal stress.

Sample 2 has an approximate relative roughness of 0.008, and the derived Reynolds numbers are always well over 2 300. This makes Sample 2 have a smooth turbulent (close to rough turbulent) flow regime under a usual range of normal stress.

Sample 3 has an approximate relative roughness of 0.005, and the derived Reynolds numbers are always around the threshold 2 300 (The value of the threshold between the laminar regime and the turbulent regime is not certain yet). This makes Sample 3 have a smooth laminar to smooth turbulent flow regime under a usual range of normal stress.

3.3.6 Cubic law

In this section, in spite of the possibility for turbulent flow according to the Reynolds number analysis reported before, we assume the flow through the fracture follows the "cubic law" as proposed by Witherspoon (1980). Then, we derive the hydraulic aperture based on our flow data. After that, we apply the same approach as Detournay (1980) to the second, third and fourth cycles of loading/ unloading of Sample 1 (We neglect the first uploading /downloading cycle because it only serves as a way of reaching a degree of matedness close to the one in-situ) and obtain Figure 3-36.

Inspection of Figure 3-36 we can see that the linear fit to the data is quite good and the x-coefficients in the linear fitting equations are all close to 1. This indicates that it is a reasonable assumption to apply the cubic law to characterize the coupled normal load-flow behaviour of Sample 1. The departure from 1 of the x-coefficients in the linear fitting equations indicates the departure from the planar parallel assumption inherent to the "cubic law", i.e. Sample 1 follows a smooth laminar to rough laminar flow regime as indicated before by the Reynolds number and the relative roughness number and therefore the x-coefficient is not exactly 1 due to the effect of the roughness of the fracture. It is important to note also that by following this approach, once the assumption of the cubic law is validated it is not necessary any further assumption in order to obtain an initial hydraulic aperture value.

If we now put together the data from the second, third and fourth cycles and follow the same procedure as before we obtain the following figures for Sample 1, Sample 2 and Sample 3 respectively (Figure 3-37, Figure 3-38 and Figure 3-39).

Again, looking at Figure 3-37 it is easy to see that the cubic law applies well to the coupled normal load-flow behaviour of Sample 1. However, Sample 2 and Sample 3 give a very poor linear fit and this indicates deviation from the cubic law. As indicated before by the Reynolds number and the roughness coefficient, Sample 2 may deviate from the cubic law due to inertial (turbulent) effects and roughness, while Sample 3 may deviate from the cubic law due to turbulent effects (Fracture Sample 3 is quite smooth so no significant roughness effects are expected). Although, as already mentioned, there are mathematical models that try to describe these types of flow regimes, this type of analysis is out of the scope of this project.

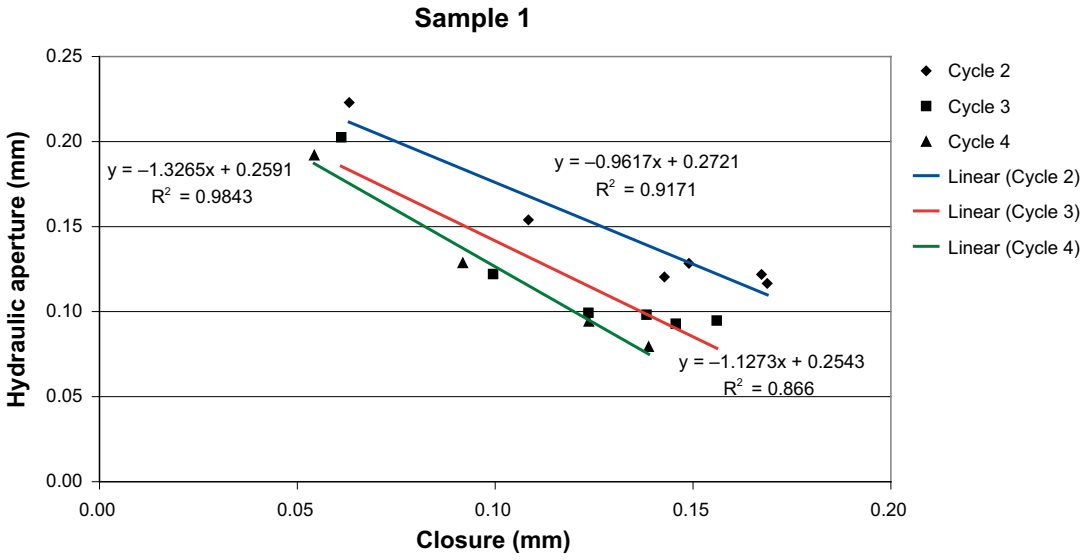

Figure 3-36. *Fracture hydraulic aperture vs. fracture mechanical closure for the 2nd, 3rd and 4th loading/ unloading cycles for Sample 1.*

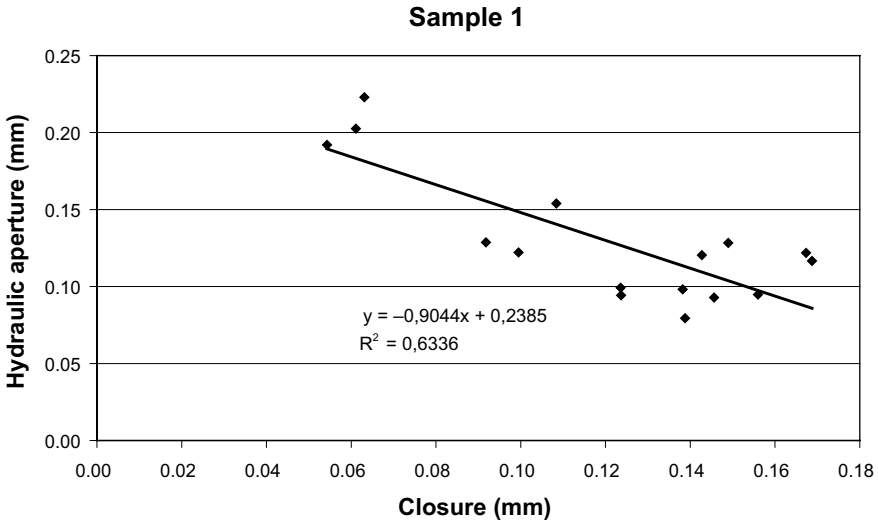

Figure 3-37. *Hydraulic aperture vs. fracture closure from the combined data from the 2nd, 3rd and 4th loading/unloading cycles for Sample 1.*

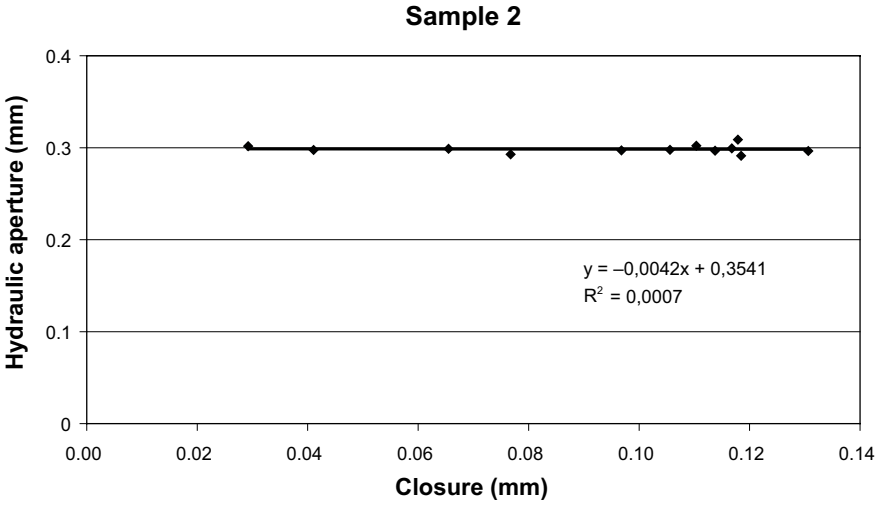

Figure 3-38. *Hydraulic aperture vs. fracture closure from the combined data from the 2nd, 3rd and 4th loading/unloading cycles for Sample 2.*

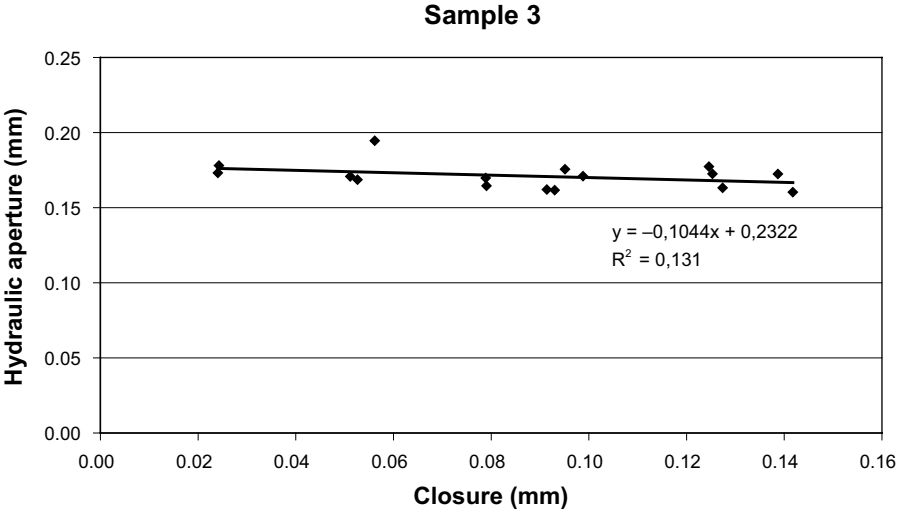

Figure 3-39. *Hydraulic aperture vs. fracture closure from the combined data from the 2nd, 3rd and 4th loading/unloading cycles for Sample 3.*

3.4 Results from the coupled shear displacement-flow test

In this section the results from the coupled shear displacement-flow tests are presented.

3.4.1 Shear stress vs. shear displacement

The shear stress vs. shear displacement response from the three coupled tests are presented in the following figures (Figure 3-40, Figure 3-41 and Figure 3-42)

While performing the test on Sample 3 some problems were experienced regarding the logging of the normal and shear force data, as well as the dilation from the central transducer, after 3.25 mm of shear displacement. Therefore, the data shown in Figure 3-42 reaches only 3.25 mm shear displacement.

The peak fracture shear strength and the calculated fracture shear stiffness and dilation angle for the three samples are listed in Table 3-5.

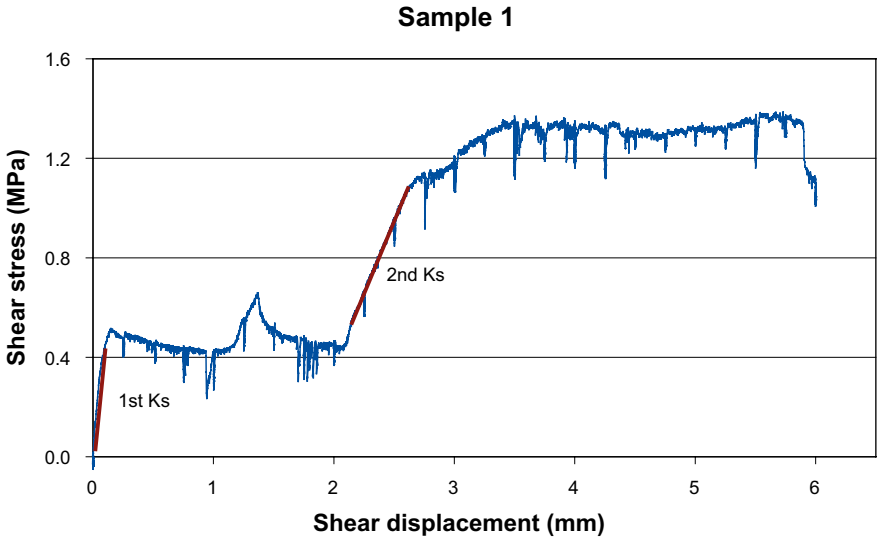

Figure 3-40. *Shear stress vs. shear displacement curve for the coupled shear-flow test on fracture Sample 1.*

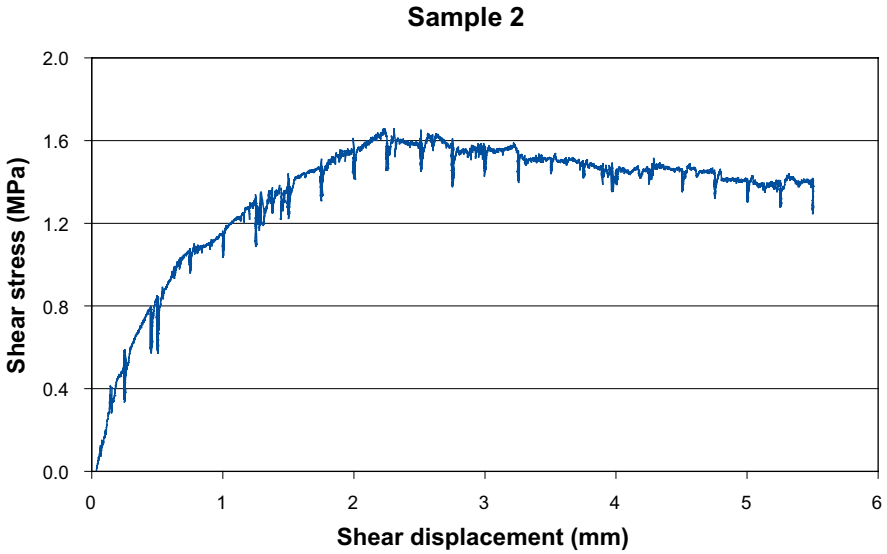

Figure 3-41. *Shear stress vs. shear displacement curve for the coupled shear-flow test on fracture Sample 2.*

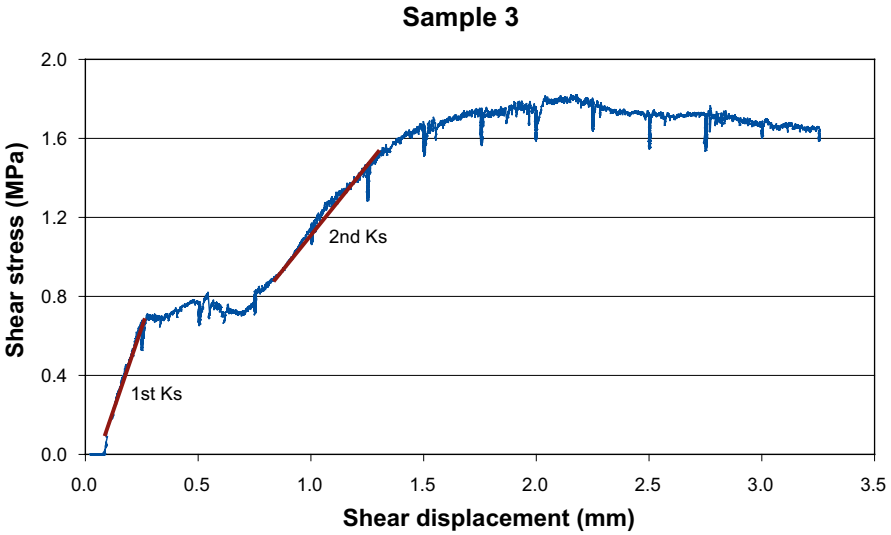

Figure 3-42. *Shear stress vs. shear displacement curve for the coupled shear-flow test on fracture Sample 3.*

Table 3-5. Peak fracture shear strength and fracture shear stiffness for the three fracture samples (2 MPa constant normal stress).

	Peak shear strength (MPa)	1st Shear stiffness, Ks (MPa/mm)	2nd Shear stiffness, Ks (MPa/mm)	Dilation angle (degree)
Sample 1	1.38	3.43	1.14	12.25
Sample 2	1.64	–	1.42	9.72
Sample 3	1.8	3.07	1.05	11.3

As can be seen in Figure 3-40, Figure 3-41 and Figure 3-42, the shear displacement-shear stress response of Sample 1 and Sample 3 has two elastic regions and several regions of slip on weak areas of the fracture before reaching the peak shear strength. When a weak area of a fracture slips, there is a transfer of shear stress from the weak to the strong area and loading along the strong area starts. This behaviour has already been reported in the literature (Mutlu and Bobet 2006).

It is important to notice that while failure in Samples 2 and 3 occurs after approximately 2.25 mm of shear displacement, in Sample 1 failure occurs at a much larger shear displacement.

3.4.2 Shear dilation and tilt analysis

The following Figure 3-43, Figure 3-44 and Figure 3-45 present the dilation (mechanical separation of the fracture walls) of the fracture samples with increasing shear displacement. Figure 3-46, Figure 3-47 and Figure 3-48 present an analysis of the tilting of each sample during the coupled shear displacement-flow tests.

As explained before, test on Sample 3 experience some logging data problems after 3.25 mm of shear displacement. In Figure 3-45 we still show the whole shear displacement as the lateral LVDTs worked correctly as well as the water flow measurements.

As explained in Section 2.1.1 about the laboratory test equipment, the measurement of the vertical displacement from the central transducer included the response from the intact rock as well as the whole concrete cast. For this reason, to minimize the error, it was decided to use the average from the four lateral LVDTs which measured the vertical displacement very close to the fracture plane.

Looking at Figure 3-43, Figure 3-44 and Figure 3-45 one can see that the dilation becomes noticeable at approximately 2.25 mm of shear displacement for Sample 1, while for Sample 2 and Sample 3 it becomes noticeable at a much shorter shear displacement (less than 1 mm). However, the maximum dilation after 6mm of shear displacement is around 0.8–1 mm for the three fracture samples.

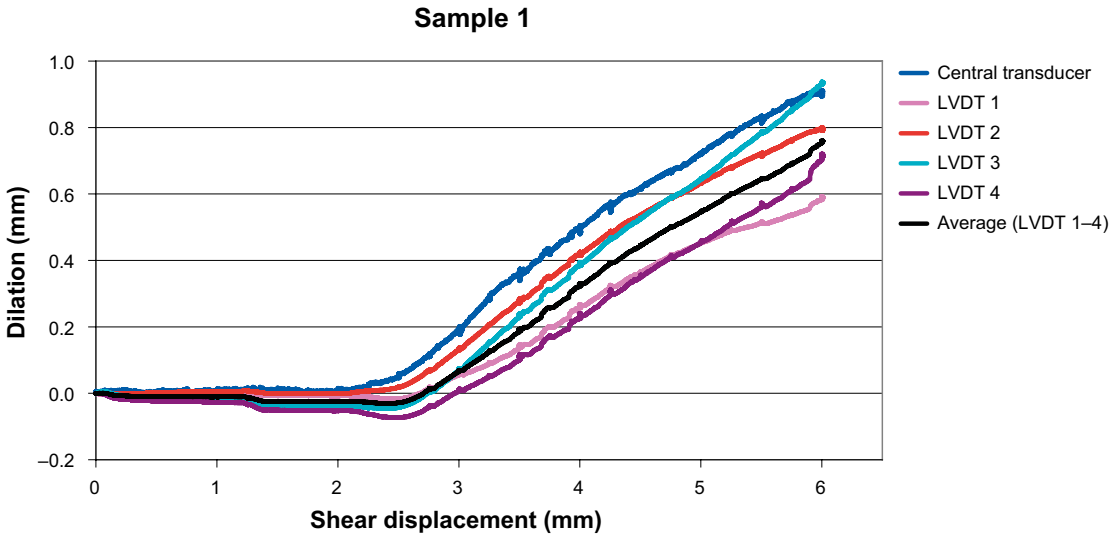

Figure 3-43. *Fracture dilation vs. shear displacement during the coupled shear displacement-flow test for Sample 1.*

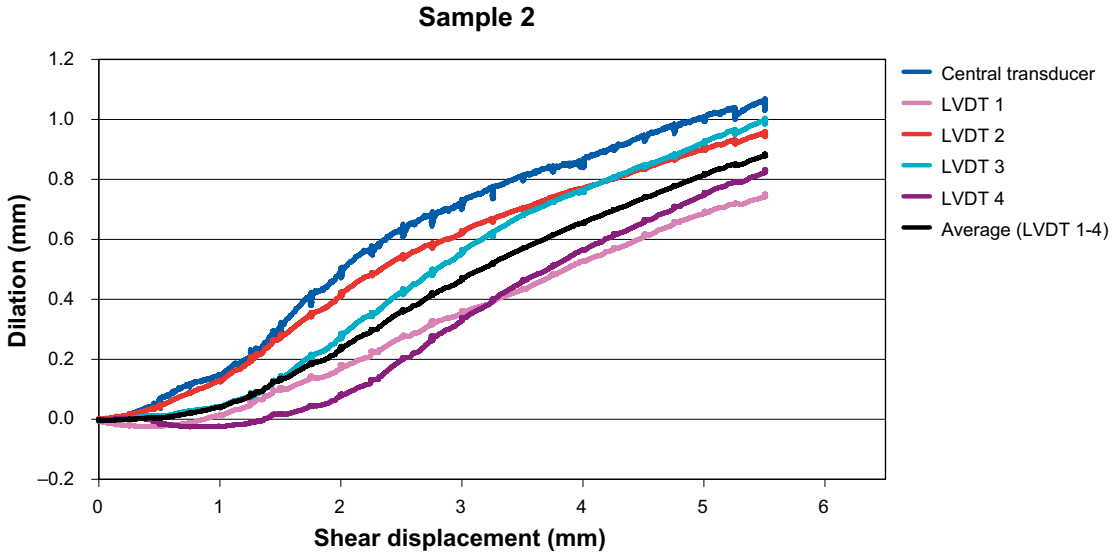

Figure 3-44. *Fracture dilation vs. shear displacement during the coupled shear displacement-flow test for Sample 2.*

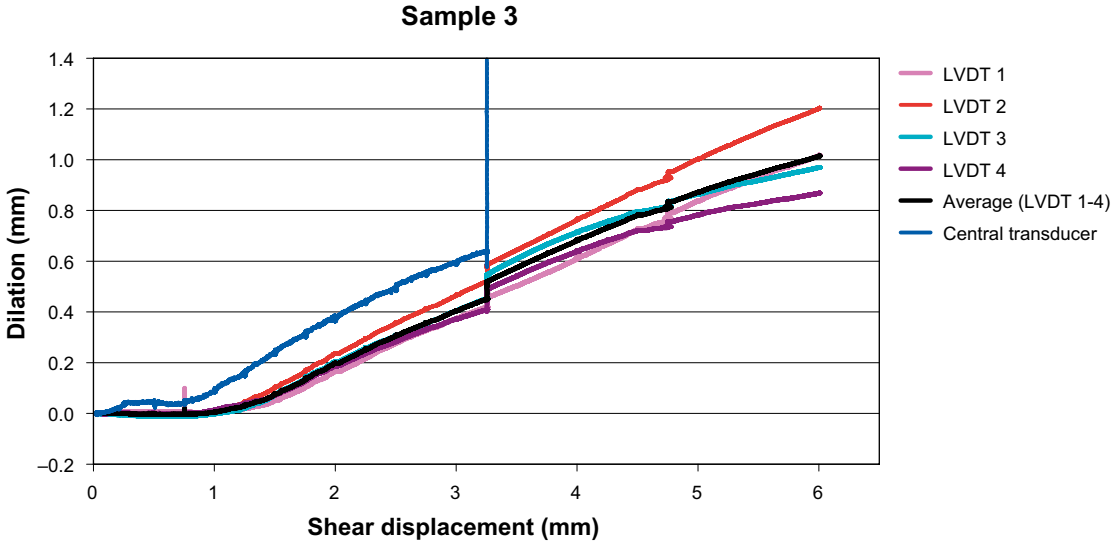

Figure 3-45. *Fracture dilation vs. shear displacement during the coupled shear displacement-flow test for Sample 3.*

To analyze the tilting of the samples during the coupled shear-flow tests, the dilation data from the four lateral LVDTs (Figure 2-6) was plotted showing the average response from different couples of LVDTs. As a result, we can see that there is a general trend in the three samples to experience a final dilation (at 6 mm shear displacement) approximately 0.2 mm larger in the water inlet area (LVDTs 2–3) than in the water outlet area (LVDTs 1–4). This is a phenomena very often observed in shear tests performed with equipment that has no possibility to adjust the normal load at different locations along the fracture plane (only one central normal load actuator). The lateral tilting (right side-left side) is negligible compared to the one mentioned before (front-back).

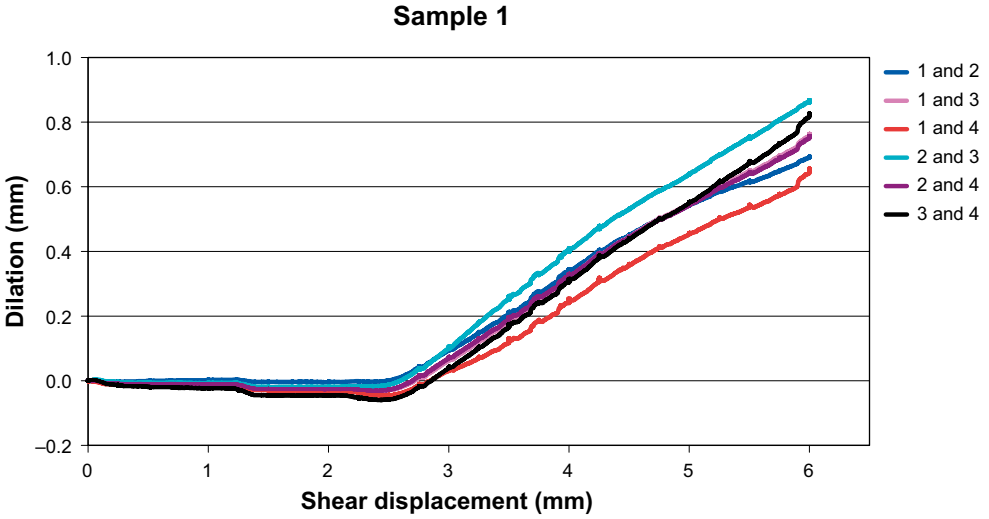

Figure 3-46. *Analysis of the tilting of Sample 1 during the coupled shear displacement-flow test.*

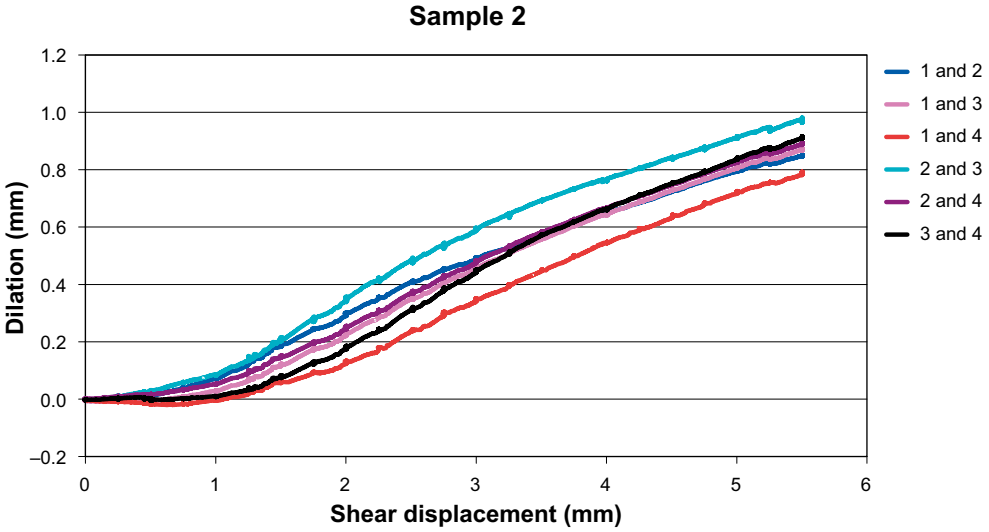

Figure 3-47. *Analysis of the tilting of Sample 2 during the coupled shear displacement-flow test.*

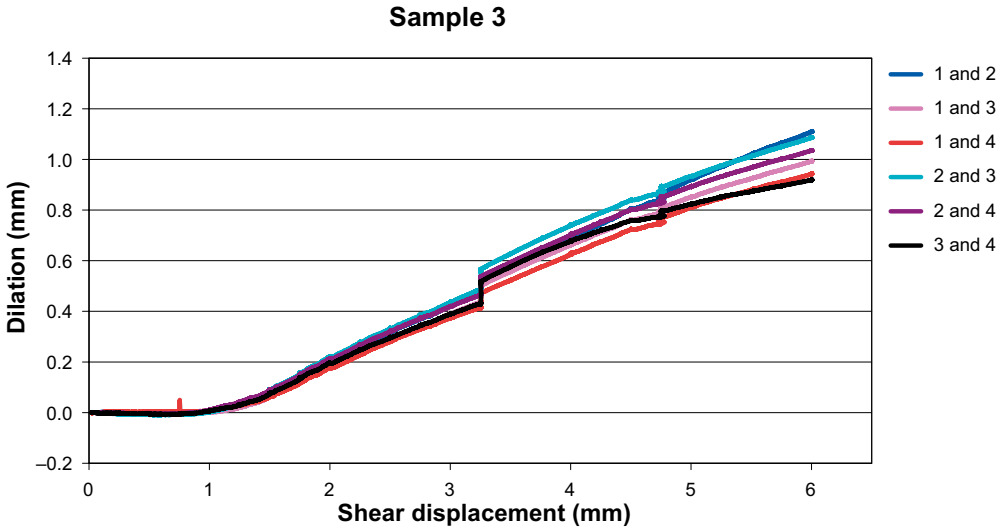

Figure 3-48. *Analysis of the tilting of Sample 3 during the coupled shear displacement-flow test.*

3.4.3 Flow rate vs. shear displacement

The following figures show the change in flow rate with shear displacement during the coupled shear-flow tests for Sample 1, 2 and 3 respectively (Figure 3-49, Figure 3-50 and Figure 3-51).

Looking at Figure 3-49 we can see that the flow in Sample 1 is very much following closely the fracture mechanical behaviour (the flow increases at the same value of shear displacement as the dilation increases and continues to do so as long as the dilation continues increasing).

Sample 2 (Figure 3-50) shows a small increase in flow with increasing dilation up to a point (around 3 mm shear) after which the flow decreases even though the dilation continuously increases. This can be caused by the fact that after certain shear displacement the change in aperture morphology is such that the main flow channels in the fracture are closed with the consequent decrease in flow. The same can be observed in Sample 3 after a shear displacement of around 4.5 mm (Figure 3-50).

Whereas Sample 1 is relatively insensitive to shear displacement for more than 2mm, Sample 2 is affected after less than 0.6 mm and Sample 3 slightly after 1 mm of shear.

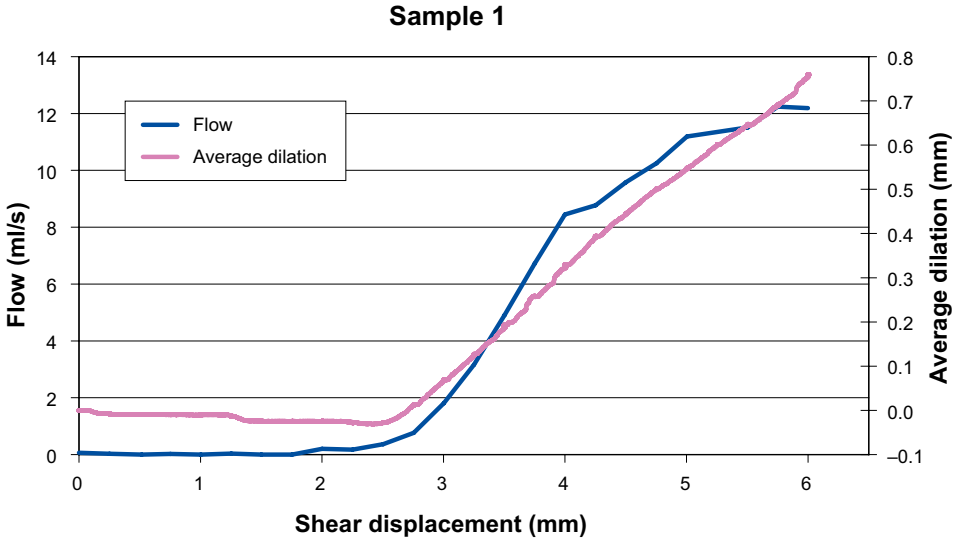

Figure 3-49. *Change of flow rate with shear displacement during the coupled shear-flow test for Sample 1.*

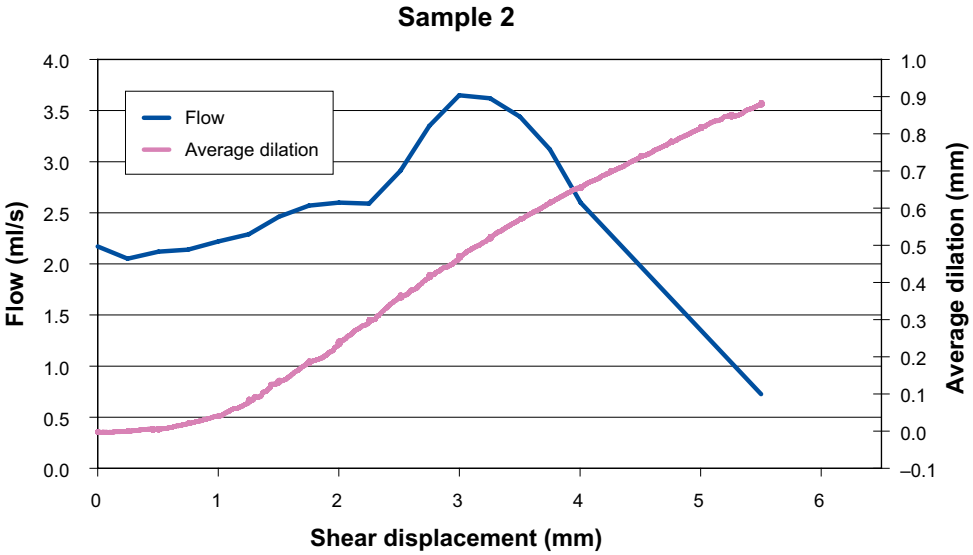

Figure 3-50. *Change of flow rate with shear displacement during the coupled shear-flow test for Sample 2.*

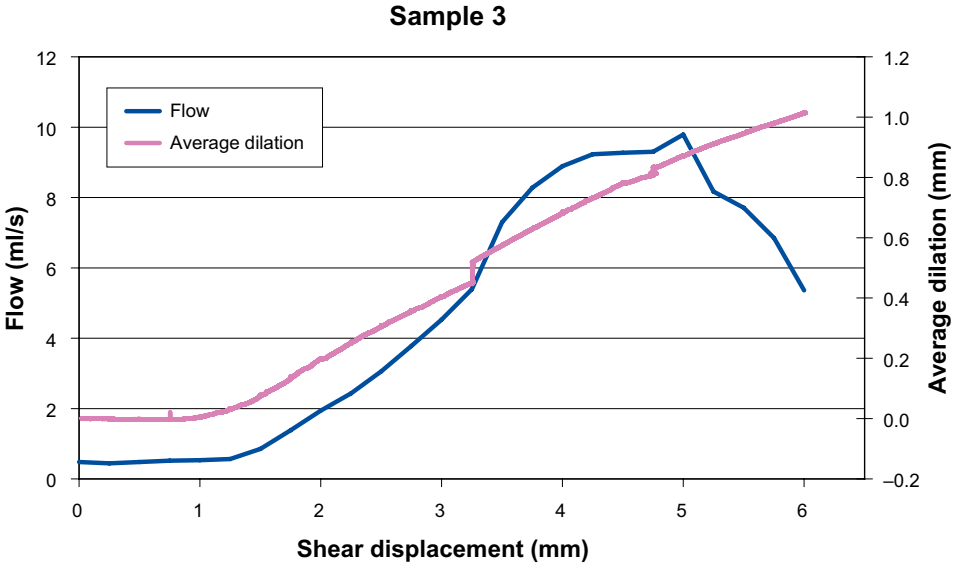

Figure 3-51. *Change of flow rate with shear displacement during the coupled shear-flow test for Sample 3.*

3.4.4 Reynolds number

The variation of the calculated Reynolds number during the coupled shear-flow tests for the three fracture samples is shown in Figure 3-52, Figure 3-53 and Figure 3-54.

As expected, the change in Reynolds number with shear displacement (Figure 3-52, Figure 3-53 and Figure 3-54) has the same trend than the flow (Figure 3-49, Figure 3-50 and Figure 3-51) for the three samples.

Whereas the Reynolds number for Sample 1 is under the critical value which dictates the change from laminar flow regime to turbulent flow regime (2 000–2 300) for more than 2 mm shear displacement, Sample 2 and Sample 3 are already in the turbulent flow regime from the start of the shear test. This implies that the "cubic law" assumption will hold for Sample 1 under a shear distance of slightly over 2 mm but it is not adequate for Sample 2 and Sample 3 because it neglects the influence of the inertial effects that are occurring in those fractures.

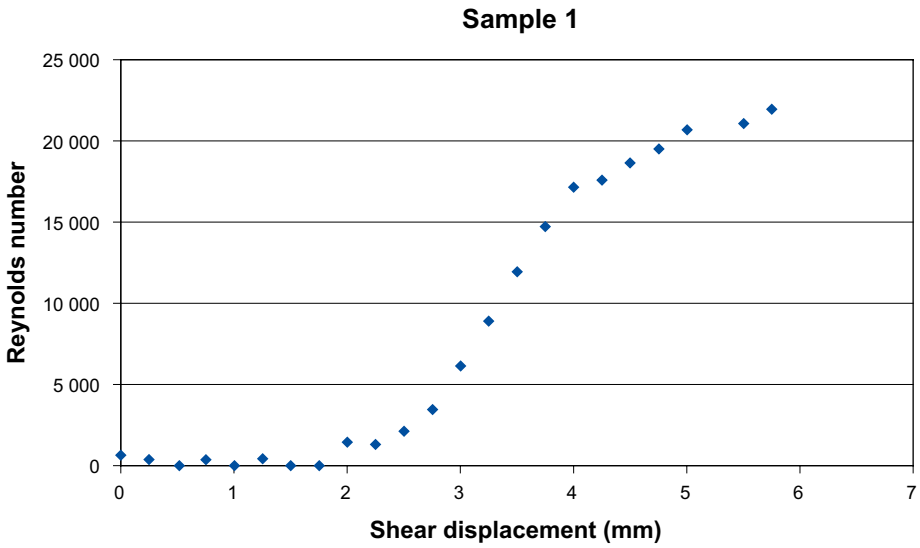

Figure 3-52. *Change in Reynolds number during the coupled shear-flow test for Sample 1.*

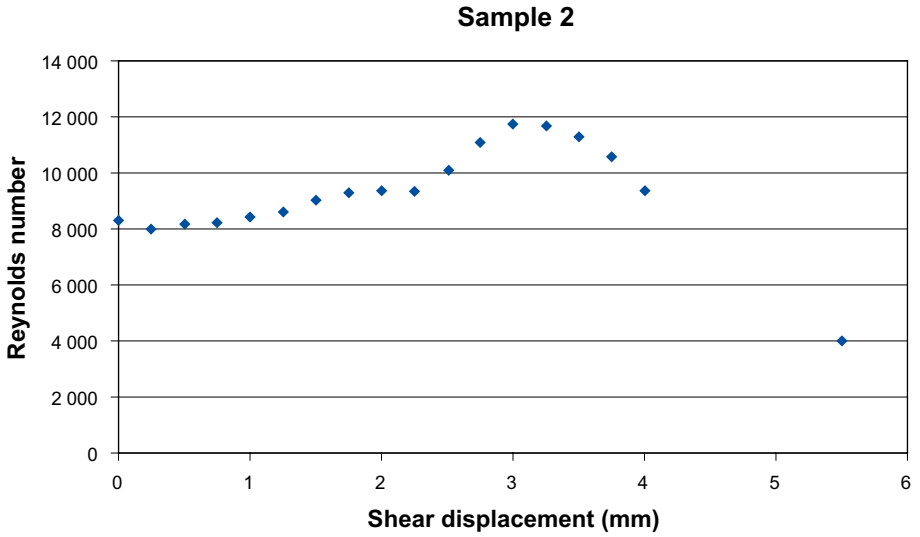

Figure 3-53. *Change in Reynolds number during the coupled shear-flow test for Sample 2.*

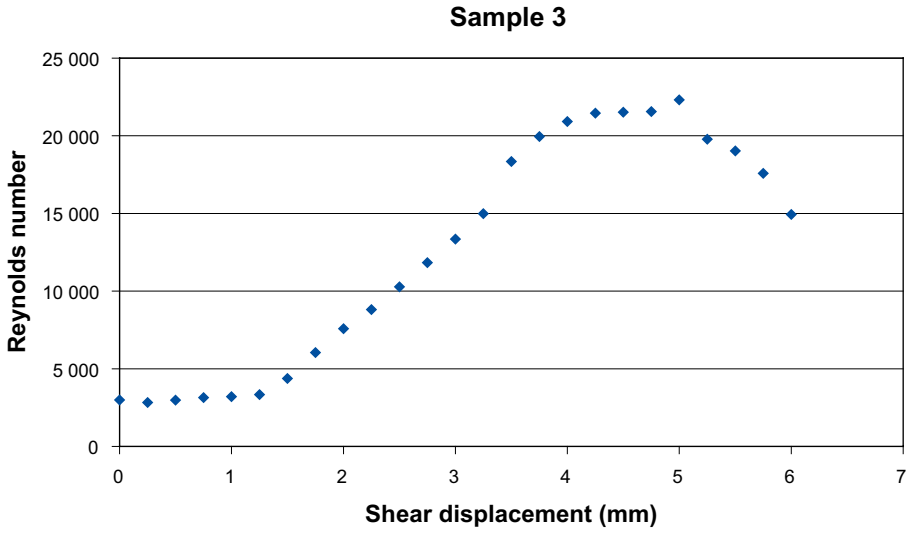

Figure 3-54. *Change in Reynolds number during the coupled shear-flow test for Sample 3.*

3.4.5 Hydraulic aperture and dilation vs. shear displacement

The following figures (Figure 3-55, Figure 3-56 and Figure 3-57) show the change in the hydraulic aperture (calculated assuming the cubic law for the three fracture samples) and dilation (mechanical separation of the fracture walls due to shear) during the coupled shear-flow tests.

As the hydraulic aperture is derived in this study assuming the "cubic law", Figure 3-55, Figure 3-56 and Figure 3-57 can serve as further indirect indicators of the adequacy of the cubic law assumption for the different samples.

As we can see in Sample 1 the dilation and the hydraulic aperture follow the same trend until almost 5 mm shear displacement (Figure 3-55). After that, the flow rate becomes so high that flow may have become turbulent, and the trends of hydraulic aperture and dilation deviate from each other and will continue to do so as shear displacement increases.

On the contrary, the hydraulic aperture of Sample 2 (Figure 3-56) shows almost no dependency at all with the change in dilation.

Sample 3 (Figure 3-57) is somewhere in between the behaviour of Sample 1 and 2.

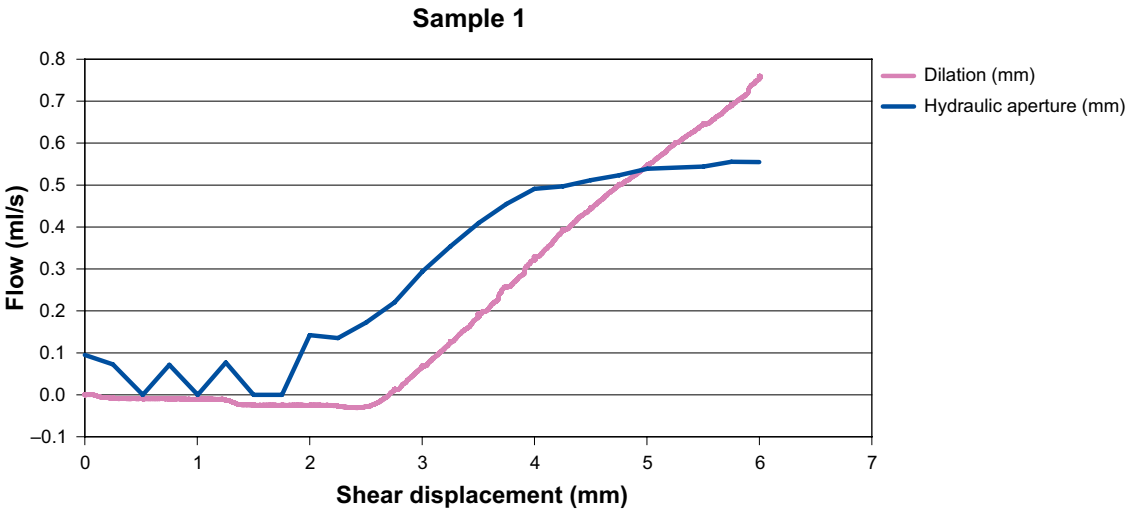

Figure 3-55. *Change in hydraulic aperture (derived from the cubic law) and dilation during the coupled shear-flow test for Sample 1.*

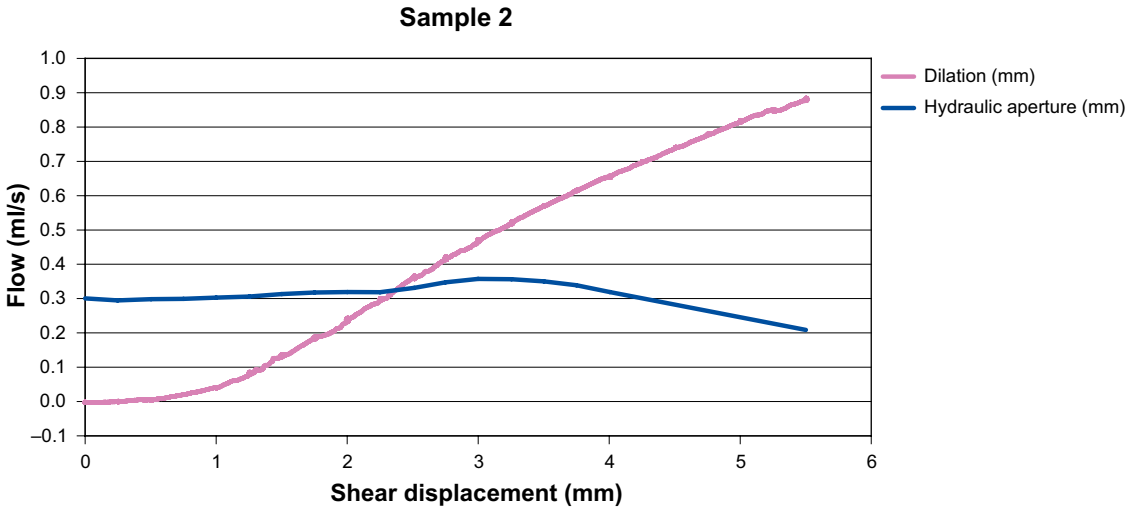

Figure 3-56. *Change in hydraulic aperture (derived from the cubic law) and dilation during the coupled shear-flow test for Sample 2.*

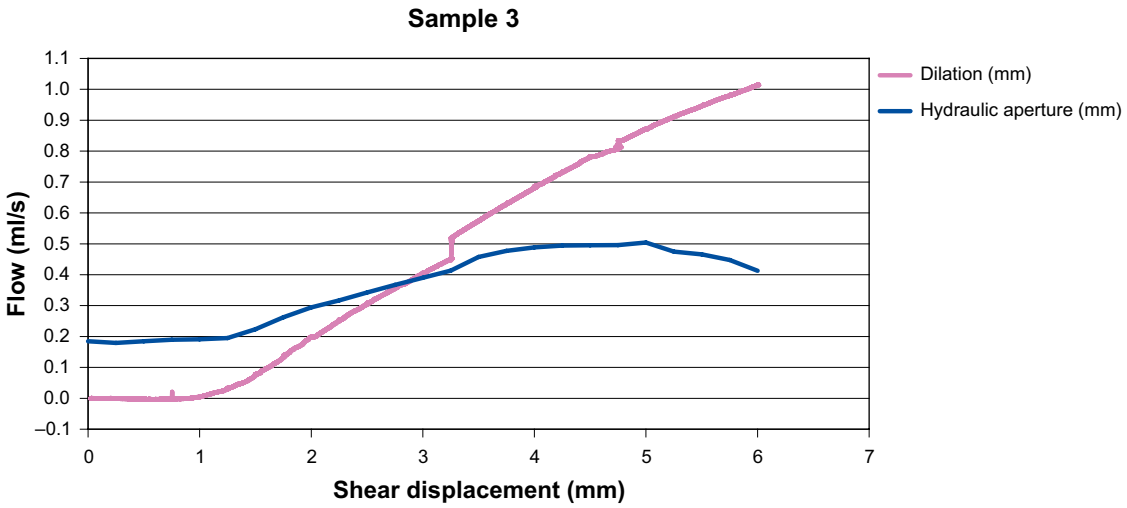

Figure 3-57. *Change in hydraulic aperture (derived from the cubic law) and dilation during the coupled shear-flow test for Sample 3.*

4 Summary and conclusions

Fully coupled stress-flow tests have been performed on three large fracture samples taken from the APSE site at the Äspö HRL in Sweden. Usually, tests of this type are performed with synthetic fracture samples or with artificially induced fracture samples due to the difficulty in obtaining undisturbed real fracture samples. Artificial or induced fractures are usually fresh and very well mated and do not have the same geological history as natural ones do. On the other hand, real natural fracture samples are much more difficult to obtain and to test, since they are less mated and far from the undisturbed planar structure ideal. Therefore, it is important to emphasize that results derived from tests on artificial or induced fractures are often closer to theoretical parallel plate models than results derived from tests on natural fracture samples.

The fracture samples used in the set of coupled fracture tests presented in this report were drilled from a very conductive fracture belonging to the NW-SE, sub-vertical fracture set that is responsible for most of the water flow at the Äspö HRL (Magnor 2004). This fracture (fracture 08 in Figure 1-2) intersected one of the deposition holes (DQ0066G01) of the APSE experiment. Flow and displacements (normal and shear) from this fracture were monitored during the de-stressing of the APSE pillar (Mas Ivars 2005) and it showed a highly stress dependent flow behaviour. For this reason it was decided to take advantage of this unique opportunity and try to characterize the coupled stress-flow behaviour of this fracture in the laboratory.

Although the three fracture samples belong to the same fracture at the APSE site (fracture 08 in Figure 1-2), their mechanical aperture contour maps and derived statistics are quite different (Figure 3-1 to Figure 3-9 and Table 3-1 to Table 3-3). The mechanical aperture of Sample 1 is the least affected by the stress-flow tests whereas the mechanical aperture of Sample 2 is the most affected. From the variogram analysis it can be concluded that anisotropy in mechanical fracture aperture grows for the three samples after the coupled tests have been performed (Figure 3-16, Figure 3-17 and Figure 3-18). It grows the most for Sample 2 and the least for Sample 1. For all three samples the sill increases significantly after the test has been performed. The correlation distance increases for Sample 1 and Sample 2 after the test indicating that the mechanical aperture is more correlated after the test than before the test. The correlation distance in Sample 3 is almost unaltered by the test.

Regarding the derived mechanical parameters for the three fracture samples, the values of normal stiffness, shear stiffness and peak shear strength do not differ significantly. This is probably explained by the fact that the samples are from the same fracture and also that they have similar size. However, meaningful shear dilation begins at approximately 2.25 mm of shear displacement for Sample 1, while it occurs at about 0.5 mm and 1.1 mm of shear displacement for Sample 2 and Sample 3 respectively (Figure 3-43, Figure 3-44 and Figure 3-45). A similar range on the onset of shear dilation has also been observed in the mechanical tests on seven smaller size (approximate area 23.5–27.5 cm^2) fracture samples from subvertical dipping fractures in the APSE area (Jacobsson and Fransbjer 2005). Some of these smaller fracture samples were obtained from the same fracture as Sample 1, 2 and 3. In the mentioned set of tests the onset of shear dilation ranged from 0.4 mm to 1.8 mm of shear displacement at 5 MPa constant normal stress. Another important aspect to point out is that slip on weak areas occurred before reaching peak shear strength in Sample 1 and 3 but not in Sample 2 (Figure 3-40, Figure 3-41 and Figure 3-42).

The values of the calculated fracture normal stiffness and shear stiffness from the three samples (Table 3-4 and Table 3-5) are 5 to 10 times smaller than the ones presented in Mas Ivars (2006) derived from the already mentioned fracture mechanical tests on seven smaller size fracture samples from subvertical dipping fractures in the APSE area (Jacobsson and Fransbjer 2005). On the other hand, the peak shear strength and dilation angle of Sample 1, 2 and 3, agree quite well with the ranges of these values reported for the seven smaller samples. There are a number of reasons that could explain the discrepancies in the derived fracture stiffness (normal and shear) and dilation values. One of the main reasons, in the opinion of the authors, is the scale effect. A difference in the size of the sample tested of this order of magnitude (6 to 10 times larger area than the samples tested by Jacobson and Fransbjer (2005)) can very well be the cause of a 5 to 10 times decrease

in fracture normal and shear stiffness. A decrease of the stiffness on this order of magnitude with a similar increase in the size of the sample has been already reported before, see e.g. Fardin (2003). There are also several other factors that could influence such as: the effect of water in the sample, the different laboratory equipment used, different thickness of concrete cast, etc. One of this aspects or a combination of them could be the cause for this discrepancy.

Several conclusions can be pointed out regarding the water flow. Whereas the flow in Sample 1 seems relatively insensitive to shear displacement for more than 2 mm, Sample 2 is affected after less than 0.6 mm and Sample 3 slightly after 1 mm of shear (Figure 3-49, Figure 3-50 and Figure 3-51). These values of shear displacement agree well with the onset of significant dilation.

The analysis of the flow regime indicates that Sample 1 has a smooth laminar to rough laminar flow regime under the range of normal stress used in these tests. The "cubic law" with an adjusting friction factor, seems to be an adequate predictor for the coupled stress-flow behaviour of Sample 1 up to a shear displacement of 2–3 mm. On the other hand, Sample 2 has a smooth turbulent (close to rough turbulent) flow regime and Sample 3 shows a flow regime somewhere in between smooth laminar and smooth turbulent. The flow in Samples 2 and 3 seems to have a turbulent (nonlinear) component that cannot be neglected and therefore the "cubic law" is not sufficient for its prediction. Other factors not studied in this project may also influence the coupled behaviour (i.e. gouge generation). Higher fracture normal stress than the one applied in this project may modify the observed coupled behaviour.

The tests presented in this report give information that is valuable to be able to describe the characteristics of the sampled fracture. However, it is important to emphasize that, even if the three fracture samples tested in this project were relatively large (13 cm × 13 cm, 15 cm × 15 cm and 15 cm × 15 cm respectively) and they belonged to the same large fracture in the APSE tunnel and were separated less than 1 meter from each other in-situ, their coupled stress-flow behaviour is remarkably different. This confirms the idea that, for this type of highly water bearing fracture, a hydraulically representative fracture area is probably larger than the areas of the fracture samples tested in this project.

References

SKB's (Svensk Kärnbränslehantering AB) publications can be found at www.skb.com/publications.

Andersson J C, 2004. Äspö Pillar Stability Experiment. Summary of preparatory work and predictive modelling. SKB R-03-02, Svensk Kärnbränslehantering AB.

de Marsily G, 1986. Quantitative hydrogeology: groundwater hydrology for engineers. Orlando: Academic Press.

Detournay E, 1980. Hydraulic conductivity of closed rock fracture: an experimental and analytical study. In Proceedings of the 13th Canadian Rock Mechanics Symposium, Toronto, Canada, 28–29 May 1980, 168–173.

Esaki T, Jinno K, Mitani Y, Jiang Y, Uchida M, Yoshino N, 2001. Experimental and analytical research on shear-flow coupling mechanism in rock joints. JNC TY8400 2001-005, Japan Nuclear Cycle Development Institute.

Fardin N, 2003. The effect of scale on the morphology, mechanics and transmissivity of single rock fractures. PhD thesis. Royal Institute of Technology, Stockholm, Sweden.

Itasca, 2003. 3DEC – 3 Dimensional Distinct Element Code, User's manual. Minneapolis, MN: Itasca Consulting Group, Inc..

Jacobsson L, Flansbjer M, 2005. Äspö Hard Rock Laboratory. Äspö Pillar Stability Experiment. Samples from TASQ tunnel at Äspö HRL. Normal loading and shear tests on joints. SKB IPR-05-23, Svensk Kärnbränslehantering AB.

Lanaro F, Öhman J, Fredriksson A, 2006. Rock mechanics modeling of rock mass properties – summary of primary data. Preliminary site description, Laxemar subarea – version 1.2. SKB R-06-15, Svensk Kärnbränslehantering AB.

Louis C, 1974. Introduction à l´hydraulique des roches. Bulletin du Bureau de Recherches Géologiques et Minières, Ser. 2, Sect. III, No. 4. (In French.)

Magnor B, 2004. Äspö Hard Rock Laboratory. Äspö Pillar Stability Experiment. Geological mapping of tunnel TASQ. SKB IPR-04-03, Svensk Kärnbränslehantering AB.

Mas Ivars D, 2005. Äspö Hard Rock Laboratory. Äspö Pillar Stability Experiment. Hydromechanical data acquisition experiment at the APSE site. SKB IPR-05-21, Svensk Kärnbränslehantering AB.

Mas Ivars D, 2006. Äspö Hard Rock Laboratory. Äspö Pillar Stability Experiment. Three-dimensional mechanical discontinuum modelling of the de-stressing slot drilling at the APSE site. SKB P-17-22, Svensk Kärnbränslehantering AB.

Mutlu O, Bobet A, 2006. Slip propagation along frictional discontinuities. International Journal of Rock Mechanics and Mining Sciences 43, 860–876.

SKB, 2008. Site description of Forsmark at completion of the site investigation phase. SDM-Site Forsmark. SKB TR-08-05, Svensk Kärnbränslehantering AB.

SKB, 2009. Site description of Laxemar at completion of the site investigation phase. SDM-Site Laxemar. SKB TR-09-01, Svensk Kärnbränslehantering AB.

Witherspoon P A, Wang J S, Iwai K, Gale J E, 1980. Validity of cubic law for fluid flow in a deformable rock fracture. Water Resources Research 16, 1016–1024.